

The Astrophysical Search For Axion Like Particle Signatures In γ -ray Propagation

Dissertation
zur Erlangung des Doktorgrades
an der Fakultät für Mathematik, Informatik und
Naturwissenschaften
Fachbereich Physik
der Universität Hamburg

vorgelegt von
Rahul Joseph Cecil

Hamburg

2025

Gutachter/innen der Dissertation:

Prof. Dr. Manuel Meyer
Prof. Dr. Marcus Brüggem

Zusammensetzung der Prüfungskommission:

Prof. Dr. Manuel Meyer
Prof. Dr. Marcus Brüggem
Prof. Dr. Marco Ajello
Prof. Dr. Oliver Gerberding
Prof. Dr. Daniela Pfannkuche

Vorsitzende/r der Prüfungskommission:

Prof. Dr. Daniela Pfannkuche

Datum der Disputation:

11.02.2025

Vorsitzender des Fach-Promotionsausschusses PHYSIK:

Prof. Dr. Markus Drescher

Leiter des Fachbereichs PHYSIK:

Prof. Dr. Wolfgang J. Parak

Dekan der Fakultät MIN:

Prof. Dr.-Ing. Norbert Ritter

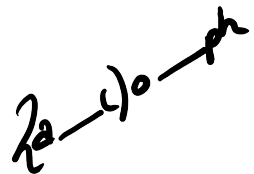
Declaration of Originality

I hereby declare that all work presented here is original and earnest. All external sources utilized in the work have been credited, referenced and/or cited explicitly or implicitly in the text, footnotes or in the bibliography. All methods, results and related information have been presented here with clarity, transparency and honesty. No plagiarism in any form has been committed in this undertaking and I bear responsibility for the authenticity of the document presented herein. Any occurrence where appropriate credit might not have been attributed is purely unintentional oversight and will be corrected upon notification.

If any electronic resources based on generative artificial intelligence (gAI) were used in the course of writing this dissertation, I confirm that my own work was the main and value-adding contribution and that complete documentation of all resources used is available in accordance with good scientific practice. I am responsible for any erroneous or distorted content, incorrect references, violations of data protection and copyright law or plagiarism that may have been generated by the gAI.

28.11.2024

Date

A handwritten signature in black ink, appearing to read 'Z. J. O. Ph', written diagonally across the page.

Signature of Doctoral Candidate

Acknowledgements

I would like to extend my heartfelt gratitude to all persons who directly or indirectly contributed toward, and supported me in this endeavor. First and foremost, I would like to thank my supervisor Dr. Manuel Meyer for entrusting me with the responsibility and associated expectations of being his first Doctoral Student. The time I have spent here has been a learning experience for both of us, and I am truly grateful for his ever present guidance and encouragement. I would also like to extend my gratitude to my colleagues whose constant motivation and presence made my efforts seem much lighter. I acknowledge my dearest family and friends whose eternal and undying support have always been the driving force in my life.

I also acknowledge support from the European Research Council (ERC) under the European Union’s Horizon 2020 research and innovation program Grant agreement No. 948689 (AxionDM) and from the Deutsche Forschungsgemeinschaft (DFG, German Research Foundation) under Germany’s Excellence Strategy – EXC 2121 “Quantum Universe” – 390833306.

I would also like to acknowledge the support of the Namibian authorities and of the University of Namibia in facilitating the construction and operation of H.E.S.S., as well as the support by the German Ministry for Education and Research (BMBF), the Max Planck Society, the German Research Foundation (DFG), the Helmholtz Association, the Alexander von Humboldt Foundation, the French Ministry of Higher Education, Research and Innovation, the Centre National de la Recherche Scientifique (CNRS/IN2P3 and CNRS/INSU), the Commissariat à l’énergie atomique et aux énergies alternatives (CEA), the U.K. Science and Technology Facilities Council (STFC), the Irish Research Council (IRC) and the Science Foundation Ireland (SFI), the Knut and Alice Wallenberg Foundation, the Polish Ministry of Education and Science, agreement no. 2021/WK/06, the South African Department of Science and Technology and National Research Foundation, the University of Namibia, the National Commission on Research, Science & Technology of Namibia (NCRST), the Austrian Federal Ministry of Education, Science and Research and the Austrian Science Fund (FWF), the Australian Research Council (ARC), the Japan Society for the Promotion of Science, the University of Amsterdam and the Science Committee of Armenia grant 21AG-1C085. We appreciate the excellent work of the technical support staff in Berlin, Zeuthen, Heidelberg, Palaiseau, Paris, Saclay, Tübingen and in Namibia in the construction and operation of the equipment. This work benefited from services provided by the H.E.S.S. Virtual Organisation, supported by the national resource providers of the EGI Federation.

Foreword

“All physical theories, their mathematical expressions apart, ought to lend themselves to so simple a description that even a child could understand them.”

- A. Einstein to L. de Broglie

Einstein: His Life and Times (1972)

The deep seeded thirst to model and predict reality is present in our very genetics. Perhaps merely an extended evolution of a survival instinct adopted by an evolutionary ancestor, this singular tendency has birthed our modern age: an age where every human being has access to technological tools of nearly incomprehensible complexity. In this era where the line between science fiction and reality seems increasingly blurred, we stand at a crossroads. Many of our leading theories describing and predicting reality are unable to keep up with our newest discoveries and inventions. On one hand, our instruments are approaching such minute scales that reality itself appears to follow a different set of physical laws. On the other hand, our detailed observations of the Cosmos at the grandest scales indicate that there exists a realm of reality so powerful that it drives the evolution of the Cosmos itself, yet it remains so well hidden that we are unable to find any direct evidence of its existence.

The shared reality we experience every waking moment of our lives is paradoxical at its core. The more we appear to know, the more we realize we can never know. Such an “un-knowability” is at the core of many of our modern theories of Physics. Heisenberg’s uncertainty principle proposes a fundamental inability to fully know the states of the quantum systems we face at the smallest scales of our reality. The theory of relativity posits that the experience of time itself is observer dependent, with our concepts of a shared time being merely a convenience. It also suggests that all causal events occur in a time bound manner, only able to occur within the limit of the propagating velocity c . This implies that in an expanding Universe, accelerating away from us in all directions, there exists a Cosmic “horizon” beyond which all causal events are disconnected from us, rendering them forever beyond our observation. Taking all these limitations into consideration, we find ourselves living in a vast Cosmic “bubble”, only able to experience our own line of time, and with boundaries on the smallest and largest scales of observation. Despite the existence of such grand limitations, the human spirit is hardly deterred. We pursue the near infinite amount of knowledge available to us within our Cosmic bubble with a fervent determination.

Standing on the precipice of a new scientific age, we seek new models of reality where our old models have begun to fail. Building on the foundation laid by the greatest human minds in history, we now face a time where our theories can no longer explain all of our observations of reality. The inability of modern theory to successfully marry quantum mechanics and gravity, the mystery of dark matter and dark energy, the unclear origin of neutrino mass. These describe just some of the failings of modern Physics to comprehensively model reality as we observe it. While disheartening at first, it also means that it is a truly exciting time for humanity. We are fast approaching a new era of Science, unlike anything we have known before. We have been presented with the opportunity to contribute toward this era in our own ways. The opportunity

presented to me during my Doctoral research has truly been an amazing one, giving me a glance at what it means to conduct research on the edge of new Physics.

I have made a conscious effort to present this thesis in a way that would provide context for, and to motivate the research we conducted. I have attempted to offer a comprehensive introduction for any researchers who might be entering the world of axions, ALPs and γ -ray Astronomy. I believe that it is important for every researcher to understand the complete context for their research and why their contribution is important. My goal with this thesis was to present the work in a highly technical manner, but while maintaining an engaging style of writing. When beginning research in fields such as that of axions and ALPs, it is often difficult to weave together all the various pieces of research that set the stage for this particular field. This here is my attempt to provide such a narrative, motivating the allocation of resources toward such studies. I sincerely hope my contributions will lend itself to the efforts of future researchers in the field.

Abstract

The work undertaken during this Doctoral period involved studying interactions of Very High Energy (VHE) γ -rays with Astrophysical magnetic fields and the Extra-galactic Background Light (EBL). The primary goal was to search for signatures of ultralight Axion Like Particles (ALPs) via their interactions with VHE γ -rays. These particles are also a promising Dark Matter candidate.

Our first project attempted to find spectral “wiggles” induced by photon-ALP oscillations in the presence of Astrophysical magnetic fields. Our candidate VHE γ -ray source was the Messier 87 Active Galactic Nucleus, located at $z \sim 0.0042$ at the center of the Virgo cluster. We chose to implement a Gaussian turbulence model for the Virgo cluster magnetic field as a radially varying function dependent on the electron density profile. Electron density measurements and calculations of Faraday Rotation measures from M87 and M84 were applied to constrain the model parameters, giving us a central magnetic field value of $B_0 = 34.2 \mu\text{G}$. We modeled spectral wiggles as outcomes of various pseudo-randomized magnetic field realizations along the line of sight. We performed Likelihood ratio tests and other statistical analyses to verify any preferences for our models, fitting the pseudo-random models against data from H.E.S.S. observational campaigns. We chose observations from 2005, 2010 and 2018 when the source was reported to have been observed in flaring/high states. Our results were statistically inconclusive, showing at best only a preference of $< 2\sigma$ for the ALPs case. Strictly speculatively, this may hint at a possible signal region within our parameter space. Reports of the magnetic field model and constraints, along with the ALP search were presented and published as proceedings at the Heidelberg International Symposium 2022 and at ICRC 2023 respectively.

Beyond our ALP searches, we were also able to make contributions toward the fields of EBL research and γ -ray Astronomy. We made a first-ever detection of intrinsic curvature in the VHE γ -ray spectrum of the AGN hosted by Messier 87 during flares. We detected such a spectral curvature in with a confidence of $\sim 4\sigma$. In a combined analysis with colleagues from the H.E.S.S. Collaboration, we were able to utilize the same data set to place upper limits on the normalization term of three EBL models which are widely used in the field of γ -ray Astrophysics. The discovery of curvature, along with the EBL model constraints were published as a peer reviewed collaboration paper in the *Astronomy & Astrophysics Journal* in 2024.

Another project during the research period searched for ALP induced upturns in the VHE spectra of γ -ray sources. We searched for, and attempted to relate spectral upturns to ALP induced transparency of the Universe to VHE γ -rays. We model the upturns as outcomes of pseudo randomized realizations of the intergalactic and galactic magnetic fields along the line of sight. We fit these models against our data set and performed Likelihood ratio tests. We see at best one limiting case where the ALPs model can be ruled out at $\sim 4\sigma$. We constructed an elaborate and robust dataset consisting of observations of our 13 candidate blazars, all of which have been observed in flaring states during H.E.S.S. observational campaigns. The data set was analyzed and temporally segmented where any source exhibited significant variability in its emission pattern with respect to its observed flux and spectral hardness. The data set

has potential application for various types of Astrophysics research and will be made publicly available after publication of our results. This effort is being undertaken by colleagues.

Zusammenfassung

Die im Rahmen dieser Promotion durchgeführte Forschung befasste sich Wechselwirkungen zwischen Very High Energy (VHE) γ -Strahlen und astrophysikalischen Magnetfeldern sowie dem Extragalactic Background Light (EBL). Das Hauptziel bestand darin, nach Signaturen ultraleichter Axion-Like Particles (ALPs) durch ihre Wechselwirkungen mit VHE γ -Strahlen zu suchen. Diese Teilchen stellen auch einen vielversprechenden Kandidaten für Dunkle Materie dar.

Unser erstes Projekt zielte darauf ab spektrale “Oszillationen” zu finden, die durch Photon-ALP-Oszillationen in Gegenwart astrophysikalischer Magnetfelder induziert werden. Als VHE γ -Strahlenquelle wählten wir den Messier 87 AGN, der sich bei $z \sim 0,0042$ im Zentrum des Virgo-Clusters befindet. Wir implementierten ein Modell der Gaußschen Turbulenz für das Magnetfeld des Virgo-Clusters als radial variierende Funktion, Abhängig vom Elektronendichteprofil. Elektronendichtemessungen und Berechnungen der Faraday-Rotationsmaße von M87 und M84 wurden angewendet, um die Modellparameter einzuschränken, was zu einem zentralen Magnetfeldwert von $B_0 = 34,2 \mu\text{G}$ führte. Wir modellierten spektrale Oszillationen als Ergebnisse verschiedener pseudo-randomisierter Magnetfeldrealisierungen entlang der Sichtlinie. Wir führten Likelihood-Ratio-Tests und andere statistische Analysen durch, um etwaige Präferenzen für unsere Modelle zu verifizieren, indem wir die pseudo-zufälligen Modelle an Daten aus H.E.S.S.-Beobertungskampagnen anpassten. Wir wählten Beobachtungen aus den Jahren 2005, 2010 und 2018, als die Quelle Berichten zufolge in Flare-/Hochzuständen beobachtet wurde. Unsere Ergebnisse waren statistisch nicht schlüssig und zeigten bestenfalls eine Präferenz von $< 2\sigma$ für die ALP Hypothese. Rein spekulativ könnte dies auf einen möglichen Signalbereich innerhalb unseres Parameterraums hindeuten. Berichte über das Magnetfeldmodell und die Einschränkungen sowie die ALP-Suche wurden als Proceedings beim Heidelberger Internationalen Symposium 2022 und bei der ICRC 2023 vorgestellt und veröffentlicht.

Über unsere ALP-Suchen hinaus konnten wir auch Beiträge zu den Bereichen EBL-Forschung und γ -Astronomie leisten. Wir machten eine erstmalige Detektion intrinsischer Krümmung im VHE γ -Strahlenspektrum des von Messier 87 beherbergten aktiver galaktischer Kern während Flares. Wir detektierten eine solche spektrale Krümmung mit einer Konfidenz von $\sim 4\sigma$. In einer kombinierten Analyse mit Kollegen der H.E.S.S.-Kollaboration konnten wir denselben Datensatz nutzen, um obere Grenzen für den Normalisierungsterm von drei EBL-Modellen zu setzen, die in der γ -Astrophysik weit verbreitet sind. Die Entdeckung der Krümmung sowie die EBL-Modelleinschränkungen wurden 2024 als peer-reviewed Kollaborationsartikel in der Zeitschrift *Astronomy & Astrophysics* veröffentlicht.

Ein weiteres durchgeführtes Projekt suchte nach ALP-induzierten Anstiegen in den VHE-Spektren von γ -Strahlungsquellen. Wir suchten nach spektralen Anstiegen und versuchten, diese mit ALP-induzierter Transparenz des Universums für VHE γ -Strahlen in Verbindung zu bringen. Wir modellierten die Anstiege als Ergebnisse pseudo-randomisierter Realisierungen der intergalaktischen und galaktischen Magnetfelder entlang der Sichtlinie. Wir passten diese Modelle an unseren Datensatz an und führten Likelihood-Ratio-Tests durch. Wir beobachteten

bestenfalls einen Grenzfall, bei dem das ALP-Modell mit $\sim 4\sigma$ ausgeschlossen werden konnte. Wir erstellten einen umfangreichen und robusten Datensatz, bestehend aus Beobachtungen unserer 13 Kandidaten-Blazare, die alle während H.E.S.S.-Beobertungskampagnen in Flare-Zuständen beobachtet wurden. Der Datensatz wurde analysiert und zeitlich segmentiert, wenn eine Quelle signifikante Variabilität in ihrem Emissionsmuster in Bezug auf den beobachteten Fluss und die spektrale Härte aufwies. Der Datensatz hat potenzielle Anwendungen für verschiedene Arten der astrophysikalischen Forschung und wird nach der Veröffentlichung unserer Ergebnisse öffentlich zugänglich gemacht. Diese Studien werden von Kollegen unternommen.

Contents

1	Introduction	1
2	Theoretical Foundation	5
2.1	The Standard Model	5
2.2	Axions and ALPs	13
2.3	AGN and Blazars	18
2.4	The EBL	20
3	Experimental Foundation	22
3.1	VHE γ -ray Astronomy	22
3.2	Axion/ALP Searches	24
3.3	EBL Measurements	25
4	Instrumentation	27
4.1	The H.E.S.S. Array	27
4.2	Data Handling	29
5	Constraining EBL Using M87	31
5.1	Overview	31
5.2	Data Selection	32
5.3	Curvature	33
5.4	EBL Constraints	35
6	ALP Searches in Virgo Using M87	39
6.1	Overview	39
6.2	Virgo	40
6.3	ALP Search	43
7	Upturn Searches for ALPs	48
7.1	Overview	48
7.2	Data Selection	49
7.3	Upturn Searches	53
7.4	Searching for ALPs	58
8	Conclusions & Outlook	64
A	ALP Upturn Searches	68
	References	91

Chapter 1

Introduction

The Standard Model (SM) of particle physics is a highly comprehensive theoretical framework, which was gradually pieced together by the contributions of many brilliant minds over the span of decades. Over the course of time, it has been amended and extended as new discoveries and theories came to light. It is a theoretical framework which has held up to inordinate amounts of testing, and has demonstrated more predictive ability than possibly any other theory in human history. Yet despite its great success, it remains unable to explain a growing list of experimental observations. This includes, but is not limited to its inability to model dark matter & dark energy, its disparity with Einstein's theory of general relativity and its inability to explain neutrino mass. There are broadly two approaches to solving this growing problem: amend the Standard Model yet again with new extensions and corrections, or disregard the Standard Model entirely and pursue a completely novel approach with a different theoretical framework. These approaches take many forms, with the first side attempting to introduce new fields, symmetries and particles to reconcile the Standard model with observational anomalies, while the latter seeks to partially or fully remake/replace the standard model with frameworks such as super-symmetry, string theory, grand unified theories etc.

In the scope of our research work, we follow an extension approach and pursue the search for an interesting class of hypothetical particles: axions and Axion Like Particles (ALPs). This class of particles was predicted in the 1970s with the intention of resolving one particular shortcoming of the SM, referred to as the Strong CP Problem. This arises in the sub-field of Quantum Field Theory dealing with quarks, gluons and the strong nuclear interaction: Quantum Chromodynamics (QCD). When experimental observation failed to discover a theoretically predicted violation of CP symmetry in the strong sector, Physicists Roberto Peccei and Helen Quinn proposed the introduction of a new global symmetry which would allow the CP violating term in the QCD Lagrangian to be nullified by setting its coefficient to zero, or more realistically the upper bounds set by experiment (Peccei & Quinn, 1977a, 1977b). Following their introduction of this new global symmetry, two Nobel laureates Frank Wilczek and Steven Weinberg introduced independently, but almost simultaneously, their solutions to the CP problem (Wilczek, 1978; Weinberg, 1978). This was presented in the form of a new particle: the axion. This specific particle is also referred to as the QCD axion for its theoretical capacity to resolve the discrepancy between theory and experiment in QCD. Other Physicists extended the theoretical axion model, primarily using the framework of String Theory, thereby introducing the set of particles referred to as Axion Like Particles. These particles along with the QCD axion are considered promising dark matter candidates, given their predicted abundance and minimal interaction with SM particles. Our research is focused on verifying the existence of ALPs in the context of an astrophysical particle search, and not directly as a dark matter search. This being said, any indication of the presence of ALPs holds direct relevance to the dark matter sector with these particles potentially being able to account for either the entirety or a fraction of the dark

matter budget of the Universe. We rely on the secondary effects caused by the Primakoff effect (Primakoff, 1951) which predicts a mixing of the photon and ALP eigenstates in the presence of external magnetic fields. This prediction is theoretically similar in its dynamics to neutrino mixing and oscillations, thereby resulting in photon-ALP oscillations in the presence of external magnetic fields. The astrophysical approach to search for ALPs via secondary effects is highly motivated by the experimentally verified presence of vast and relatively strong natural magnetic fields in inter and intra-galactic space, combined with our ability to detect Very High Energy (VHE) γ -ray sources, which function as particle generators in our Cosmic laboratory.

By employing these naturally occurring systems to create a “laboratory” of Cosmic scales, we overcome many of the logistical and technological limitations of ground based experiments searching for these particles. Of course, exploiting natural systems that cannot be reproduced on Earth comes with its own unique set of challenges. One of the leading challenge in this scenario is our inability to predict natural systems with high accuracy due to their chaotic nature. The theoretical models we implement to study these systems have to account for the apparent randomness we encounter in nature, and this can often be a limiting factor given our current level of computational technology and theoretical prowess. Astrophysical searches are also subject to vast background and foreground noise, leading to low signal to noise ratios, making detections quite challenging. Compared to the strictly controlled environments of a laboratory, this paradigm could be compared to hunting for small game in a vast jungle, equipped with nothing but a toy pistol, a pair of binoculars and a folding map of the vast wilderness we find ourselves in the middle of. Regardless of the seemingly impossible challenge inherent to this type of work, the search for this class of particles is a growing global endeavor with growing amounts of success. New experiments and studies are appearing worldwide, probing ever deeper into the parameter space of expected mass-coupling values for the particles. The general narrative of axions, ALPs and the current state of research is explored in the following thesis.

While the different approaches taken toward ALP searches truly showcase the extent of human ingenuity and innovation, we limit our work to one general approach. As mentioned earlier, our focus is on the secondary effects arising from the mixing of photon and ALP eigenstates as predicted by the Primakoff effect (Primakoff, 1951). The photon-ALP oscillations resulting from said mixing has some rather interesting consequences, particularly on VHE γ -ray propagation over Cosmic scales. Within the realm of γ -ray astronomy and astrophysics, there are many known phenomena that affect the propagation of these energetic photons. This includes interactions with interstellar and intergalactic dust and plasma, interactions with magnetic fields and interactions with background photons. We expect from theoretical models of ALPs that the introduction of these exotic particles can have additional consequences to these already well-known effects. We focus primarily on photon extinction effects and anomalous γ -ray transparency effects in the context of our research. In the course of our analyses, we work with the H.E.S.S. Collaboration as official members, employing archival data and proprietary software provided from the Imaging Atmospheric Cherenkov Telescope (IACT) array and its associated organization. Located in the Khomas Highlands of Namibia, this telescope array is one among the first generation of such telescopes and has provided us with countless hours of vastly interesting data from the γ -ray Universe.

Our first project focuses on the loss of signal photons due to photon-ALP conversions in the presence of astrophysical magnetic fields. Due to predicted photon-ALP oscillations, we have a probabilistic chance of photons along our energy spectrum arriving at our detectors in the ALP eigenstate, rendering them “extinct” to our perspective. The combined effect of such photon extinction manifests as “wiggles” in the spectra of certain γ -ray sources, specifically in the VHE range when considering ultralight ALPs in the neV mass range. We select Messier

87 (M87) as our candidate high-energy particle generator, with the intention of exploiting the well documented tendency of the AGN hosted at its core to occasionally flare, entering high states of activity and emitting increased amounts of high-energy particles including VHE γ -rays. The Virgo cluster which hosts M87 at its center provides us a large scale magnetic field on the order of a few Mpc which is ideal to probe the expected pc - kpc scale oscillations for our chosen section of the mass-coupling parameter space of ALPs, focused on ultralight neV scale ALPs. Additionally we accommodate for the Milkyway magnetic field using the existing JF12 model (Jansson & Farrar, 2012). We employ a Gaussian turbulence model for the Virgo cluster magnetic field, deviating from previous studies of a similar nature which use a randomized cell-by-cell approach. We begin by attempting to constrain the central magnetic field value and its fall-off factor which describes a radially varying electron density profile. This is achieved by calculating Faraday Rotation measures with our pseudo-randomized magnetic field model along two lines of sight and comparing their intersectional values to reported values from past studies. The constrained magnetic field model is then used to simulate and search for ALP wiggles by generating pseudo-randomized spectral models. This is done by calculating various possible realizations of the line of sight magnetic fields and the resulting ALP wiggles. We perform Likelihood analyses and draw conclusions based on the results.

During the initial processing of the M87 data set, we discovered a distinct curvature in the intrinsic spectrum of Messier 87. Such a curvature during its high/flaring states has never been reported before. As such, we undertook the effort to report our findings. We combined our analysis with another ongoing H.E.S.S. Collaboration project which utilized a very similar data set with a different goal. This study attempted to place constraints on the normalization value of three relevant Extragalactic Background Light (EBL) models currently used in the field. We published a combined article describing the statistical motivation for the detected curvature, possible explanations for said curvature, and the results of the EBL model normalization upper limits. My individual contribution toward the publication was the primary analysis for both studies using the *gammapy* open source framework (Donath et al., 2023).

The next undertaking during the Doctoral research period involved the search for spectral upturns in VHE γ -ray sources as a predicted secondary effect of photon-ALP oscillations. While our Universe is expected to have a certain “opacity” toward VHE γ -rays due to the presence of the EBL, the introduction of ALPs in our Cosmology allows for some photons to by-pass this barrier. This would manifest as anomalous photon events appearing in our detectors beyond the expected cut-off caused by EBL attenuation. For the purposes of this study, we construct a robust and effective data set comprising observations made of 13 different blazars at various Cosmological redshifts, reported to have been observed in flaring states. We study each source carefully, segmenting our data where the respective source displays any significant variability in its emissive behavior. This results in a carefully organized final data set which has the potential for use in many contexts of research, not just for upturn searches. We utilize the data set to search for any indications of general upturning in the spectra with careful statistical fits. After conducting these searches, we attempt to verify the ALP-induced nature of any possible upturning by constructing models for ALP induced upturns for each source. We do this by accounting for the intergalactic and Milkyway magnetic field using existing models. We perform Likelihood analyses and draw our final conclusions from the results.

Reported herein are all the methods employed toward our research and the results of our efforts. I have also attempted to provide the foundational context motivating our research and setting the stage for future efforts. The research we conducted has been presented at International conferences and meetings, with multiple publications made in the form of proceedings and an article in the *Astronomy & Astrophysics* journal. The results of our upturn searches are pending publication, with publications efforts being carried out by colleagues within the

research group. Only one study was conducted on the robust data set we developed due to time constraints but there are many potential applications for this data set, both within the context of ALP searches and beyond.

Chapter 2

Theoretical Foundation

2.1 The Standard Model

2.1.1 Quantum Field Theory

As the name implies, Quantum Field Theory (QFT) is a theoretical framework which attempts to marry classical field theory with special relativity and quantum mechanics to provide a quantum theory of reality as described by fields. This theoretical framework is the foundation upon which one of the leading theoretical frameworks regarding elementary particles and their interactions is built. The Standard Model of Particle Physics represents the culmination of decades of research and effort, modeling nature with unprecedented accuracy upon the foundation of QFT. In the formulation of QFT, point particles are not considered the fundamental building blocks of physical reality. Instead, the fundamental entities which constitute reality are described as a collection of quantum fields that pervade all of reality, generating our physical reality through their various interactions. The particles we observe appear as excitations or *quanta* in these Universal fields. The elementary matter quanta of the Standard Model interact with each other through the fundamental forces: electromagnetic, weak nuclear, strong nuclear and gravity. It is important to note that gravitational interactions are still not accepted as part of the SM, with theoretical models yet unverified by experiment.

The interactions in the SM are facilitated by force carrying virtual particles termed gauge bosons. These virtual particles are created and annihilated within the span of their respective interactions as temporary excitations in their quantum fields. These particles borrow energy from the Universe within a predicted time-energy uncertainty, only to return their energy to the Universe upon facilitating the interaction in question. Their lifetimes being determined by their masses, the massless gauge bosons have an infinite range of effect while the massive ones have limited ranges. The dynamics of these interactions as facilitated by their gauge bosons are described by Lagrangians (\mathcal{L}) and the principle of least action as applied to their respective Lagrangian. The collective Lagrangian which describes the entire set of interactions in the Standard Model is referred to simply as the Standard Model Lagrangian. This behemoth of a formulation now includes the Lagrangians for the fundamental forces and higher order corrections which have been introduced to compensate the infinities which occur in the mathematical formulation of the theory.

The overall Lagrangian comprising all individual components of the Standard Model can be expressed in its simplest condensed form as:

$$\mathcal{L}_{\text{SM}} = \mathcal{L}_{\text{gauge}} + \mathcal{L}_{\text{fermion}} + \mathcal{L}_{\text{Higgs}} + \mathcal{L}_{\text{Yukawa}} \quad (2.1)$$

To understand this seemingly simple set of components let's take a journey through the story of the Standard Model before revisiting the complete Lagrangian once again with context. The foundation for QFT, and by extension the Standard Model, was laid by Paul Dirac in the 1920s when he attempted to quantize the electromagnetic field (Dirac, 1927). He also established the concept of creation and annihilation operators, which are fundamental to QFT. Additional contributions from Wolfgang Pauli, Eugene Wigner, Pascual Jordan, Werner Heisenberg and Enrico Fermi led to more improvements on this foundational work in the 1930s. Following even more contributions and corrections by Physicists like Robert Oppenheimer, eventually a fully covariant formulation of Quantum Electrodynamics (QED) was established by Shin'ichirō Tomonaga, Julian Schwinger, Richard Feynman and Freeman Dyson. Tomonaga, Schwinger and Feynman shared the Nobel Prize for their work in 1965. Within its framework, QED describes light-matter interaction, specifically the interaction between electrically charged particles and light. It found incredible success in predicting these interactions, notably being able to predict the anomalous magnetic moment of the electron and the measured Lamb shift in the Hydrogen atom (Feynman, 2018, 2006). QED has been able to make some of the most accurate predictions about the sub-atomic world, even within the broader scope of QFT. Perhaps this can be attributed to the relative simplicity of these interactions as compared to weak and strong interactions.

With the establishment of QFT and the success of QED setting the stage, we see the emergence of a new Quantum Field Theory and with it a new sector of quantum field theories: Quantum Chromodynamics, or QCD for short. The story of QCD begins in the 1960s when Murray Gell-Mann (Gell-Mann, 2018) and Yuval Ne'eman (Ne'eman, 1961) proposed a scheme to classify hadrons based on SU(3) symmetry. The idea of symmetries in the Standard Model is explored in further detail in the Symmetries section of this chapter, and will not be explored further here. Keeping to the narrative, both physicists constructed their classification schemes independently. Following this work, they independently proposed the quark model which suggested that hadrons actually were a collection of quarks bound together. Zweig called the particles “aces” while Gell-Mann coined the term “quarks”. The model postulated that there were three types or “flavors” of quarks: the up, down and strange quarks. They suggested that these quarks interacted via the strong nuclear force with gluons as the force mediating particles. Experimental evidence started appearing to support their quark model in the early 1970s. Here we see the emergence of QCD as a method to further explain strong interactions in quarks. Gell-Mann also coined the term “color” to describe the internal degree of freedom of the quark triplets, hence introducing the term Quantum Chromodynamics to classify the field of study concerning quarks and their interactions through the exchange of gluons as mediators of the strong nuclear force. Through the 1970s and beyond, advancements in particle physics experimental methods led to the discovery and confirmation of not just the three quarks predicted originally, but also of the charm, top and bottom quarks. The quantum field theory of QCD is now an integral part of the Standard Model.

Alongside QED and QCD we see the appearance of another set of QFTs, together forming one of the strongest theoretical frameworks in modern physics. This new sector is also referred to as Quantum Flavordynamics or QFD. This appears at a time where scientists had already discovered three types of radiation: α , β and γ . This was a result of the foundational work of scientists like Henri Becquerel, Marie & Pierre Curie, Ernest Rutherford, Paul Villard and many others. The story of QFD itself begins perhaps with a famous letter written by Wolfgang Pauli in 1930. In this letter he attempts to resolve the then prevalent beta-particle energy conundrum. In simple terms there was an observational inconsistency in the energy equations of known products in beta decay, and a seeming violation in momentum and angular momentum

conservation in the system. Pauli proposed the existence of a new extremely light and neutral particle which existed in atomic nuclei. He called this particle the neutron. He postulated that this light neutral particle was also emitted during beta decay and it was merely unobserved due to its comparatively small stature and inertness. This new particle would account for the missing momentum and resolve the beta-conundrum. Following up on Pauli's idea, in 1931 Enrico Fermi renamed Pauli's neutron and gave it the name neutrino, meaning little neutral one. This was required to accommodate the discovery of the particle we now refer to as the neutron, discovered by Chadwick in the meantime. In 1933 Fermi published his theory of weak interactions, applying the principles of quantum mechanics to elementary particles of matter (Fermi, 1934a, 1934b). He introduced the idea that these particles could also be created and annihilated just like light particles (photons) in atomic transitions. This implied that the neutrino was not present in the nucleus, but rather was being created in the beta decay process. With these predictions made, neutrinos were finally detected by Clyde Cowan and Frederick Reines in 1956 (Cowan Jr, Reines, Harrison, Kruse, & McGuire, 1956). This now established a model for describing weak nuclear interactions and laid the foundations for QFD. Things took a very interesting turn upon the discovery of parity violation in the weak sector. Tsung-Dao Lee and Chen-Ning Yang began this journey in 1956 when they attempted to understand why τ and θ mesons had different numbers of decay products (pions) (Lee & Yang, 1956). Following this, Chien-Shung Wu devised an ingenious experiment using ^{60}Co atoms in a magnetic field (Wu, Ambler, Hayward, Hoppes, & Hudson, 1957). The details of this experiment and the exploration of Parity and Charge-Parity violation are further explored in the Broken Symmetries section of this chapter.

Fermi's theory was now modified to include parity violation. Fast forward to 1964, Murray Gell-Mann and Herald Fritzsch introduced the term flavor to describe quarks in their new model. We see here how the field of QFD arises alongside the field of QCD. Quantum Flavordynamics derives its name from the weak interactions that grant quarks their ability to change from one flavor state to another, whereas QCD referred to their ability to exchange color charges via strong interactions. In the years leading up to this point, the work of researchers such as Steven Weinberg, Abdus Salam, Gerardus't Hooft and Martinus Veltman culminated in the unification of electromagnetic and weak interaction theories into the electroweak theory in 1972. By 1983, the W and Z bosons were discovered at CERN, firmly establishing the electroweak theory and solidifying the place of QFD in the Standard Model of Particle physics. The discovery of the Higgs boson at CERN in 2012 further proved the predictive power of electroweak theory.

With the establishment of the fields of QED, QCD and QFD we see the formation of the Standard Model of Particle Physics as we know it today. Referring to equation 2.1 once more, we can now see each of the components come together as one whole. $\mathcal{L}_{\text{gauge}}$ describes the kinetic energies and the self-interaction terms of all the gauge bosons (force carrying particles), $\mathcal{L}_{\text{fermion}}$ describes the interactions of all quarks and leptons (spin $\frac{1}{2}$ particles). $\mathcal{L}_{\text{Higgs}}$ describes the Higgs field and its interactions, while $\mathcal{L}_{\text{Yukawa}}$ describes the interactions between fermions and the Higgs field, yielding fermion masses. The Higgs field, mechanism and related topics are further explored in the Mass Terms section ahead. We now begin to see the Standard Model take shape in all its elegance and predictive power.

The contributions of many brilliant minds and vast amounts of research culminated in one of the most successful predictive theories till date. It describes every known fundamental particle and their interactions, how they gain mass and generate reality as we know it. But this period of glory would not last forever. There were some fundamental issues with the theory to begin with. The most obvious being its inability to describe gravity in a way that was consistent with one of the other monumental theories of modern Physics: Einstein's Theory of General Relativity. And when we arrive at the present state of Physics, we see the growing need for

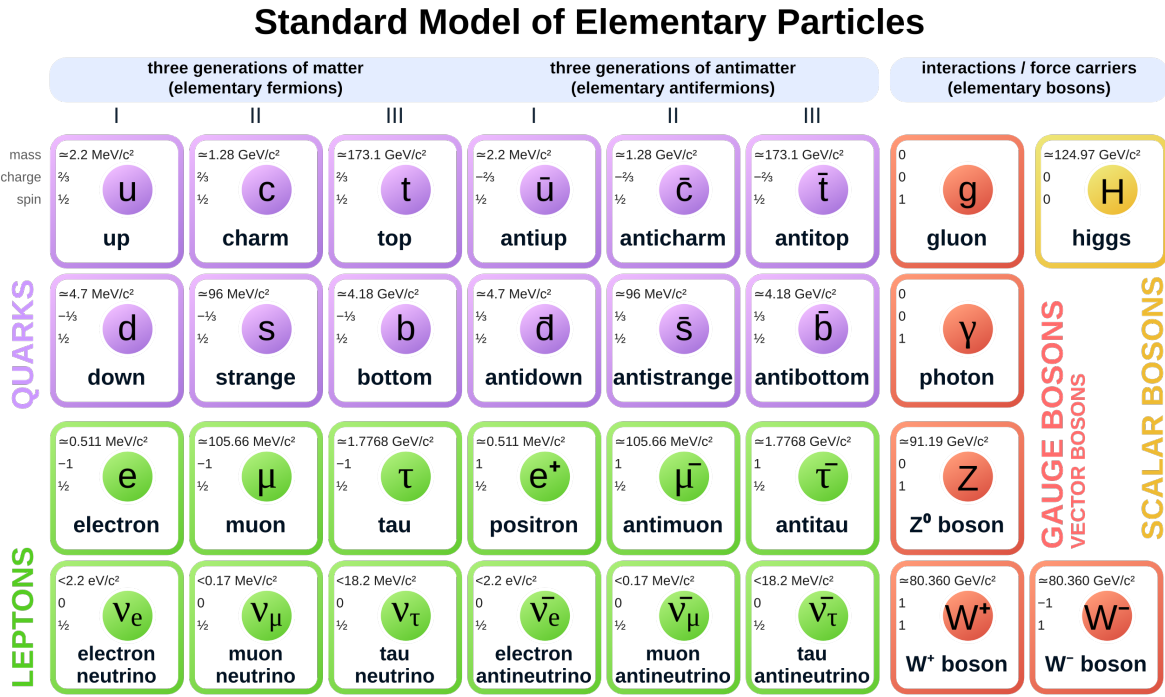


Figure 2.1: An Illustration of The Standard Model of Particle Physics, showing all the quarks, leptons, their respective anti-particle, gauge bosons and the Higgs boson.
Credit: Wikimedia Commons License

a set of extensions, or even a complete replacement of this theoretical behemoth with a novel framework to describe how physical reality is generated and sustained. The limitations and outlook for the Standard Model are discussed in more detail in the Limitations sub-section ahead.

2.1.2 Symmetries

Since the emergence of human civilization, we as a species have been captivated by the idea of symmetry. Early natural philosophers hypothesized that nature would embody the same perfection as the being(s) that they believed created the Universe. To them, mathematical symmetry in physical laws reflected an underlying perfection, which ultimately governed the seemingly imperfect external Universe. This idea has been carried historically through generations with its presence still found in modern physics. The belief that nature must be perfect and symmetric at its most fundamental level is still captured in most of our modern theories of reality. We have a tendency to believe that reality must fundamentally embody something perfect and predictable. Maybe this is simply an attempt to preserve our own sanity, lest we are rendered insane by the notion of an inherently chaotic and imperfect reality beyond our knowing and control. Luckily enough for us, evidence suggests that the Universe does not appear to be completely chaotic and there are many aspects of it that are indeed symmetric. When speaking of symmetries, perhaps the most iconic figure is the mathematician Emmy Noether. She presented the world with an elegant theory describing symmetries (Noether, 1918) which has far reaching implications in physical reality. Noether’s simple idea suggested that the presence of a symmetry in any physical system implies the existence of a conserved quantity associated with said symmetry. This seemingly simple concept is extremely powerful and sits at the very foundation of QFT and the standard model.

When deliberating in the context of the Standard Model, we are primarily focused on a specific type of symmetry: gauge symmetry. The Standard Model in a very simplified sense can be expressed by three gauge symmetry groups. These groups were developed over years, with the effort of many notable Physicists including Paul Dirac, Sin-Itiro Tomonaga, Julian Schwinger, Richard Feynman, Enrico Fermi, Werner Heisenberg, Chen Ning Yang, Robert Mills, Murray Gell-Mann, Yuval Ne'eman and George Zweig. The symmetries can be written in simple notation as:

$$SU(3) \times SU(2) \times U(1) \tag{2.2}$$

Let's take a moment and unpack this mathematical expression in a simplified manner, ignoring more complicated underlying symmetries and global symmetries, keeping our focus simply on gauge symmetries. To begin with, U here stands for Unitary Matrix and SU for Special Unitary Matrix. These matrices imply a transformation made to the system along one or more symmetric axes. In each case, there is an accompanying conservation law as necessitated by Noether's Theorem. Each symmetry describes how the respective interactions can undergo local modifications without affecting measurable physics. The U(1) symmetry group was originally associated with electromagnetism, the electromagnetic field and its gauge boson: the photon. Transformations under this symmetry would conserve electric charge. SU(2) symmetry originally provided a description of weak interactions, the weak fields and their accompanying gauge bosons: W^\pm and Z. Transformations under this group conserve weak iso-spin. It is important to note that in the new description of these symmetries, the SU(2) \times U(1) symmetries are described under the unified electroweak symmetry group and transformations under this symmetry group conserve weak iso-spin and electroweak hyper-charge. The SU(3) group describes strong interactions, the strong fields and their associated particles: quarks and gluons. Here the conserved quantity under transformation is color charge. Attempts are constantly being made to unify all the interactions including gravity, similar to how electroweak unification was done. Achieving this lofty goal would result in what Einstein referred to as Unified Theory or a theory of everything.

There are other symmetries also involved when describing nature, and the Standard Model houses many more than just the gauge symmetries described above. Quite important are global symmetries. A good example is Poincare symmetry which describes symmetries/conservation under translation, rotation and Lorentz boosting. Another important appearance of global symmetry is in the Higgs Mechanism. According to theory, the Higgs field develops a non-zero vacuum expectation value and spontaneously breaks a global U(1) symmetry (Higgs, 1964). This mechanism is essential to describe how particles gain mass in the Standard Model. We will explore this concept a bit further in the following section(s). Discussing every symmetry in the Standard Model would be highly interesting, and worth an entire publication in itself. Alas, it is beyond the scope of our work. While we see that the Universe appears to be largely symmetric, this isn't always the case.

2.1.3 Broken Symmetries

For human sensibilities, it is often expected or hoped at least, that nature is perfect and symmetric. But reality is not bound by the comfort of human sensibility, and often comes around to prove us wrong. The same applies in Physics and we have come to find certain fundamental physical symmetries to be broken by nature, shaking the foundation of humanity's historical beliefs of perfection in nature. While physical theories have managed to largely conserve the

notion of an overall symmetry in nature, this was not without complications. While the concept of broken symmetries is vast, let's explore the broken symmetries that pertain to the scope of the work undertaken here.

The story here begins in 1956 with Chien-Shiung Wu, who orchestrated an experiment to test parity symmetry. Parity symmetry is merely inversion symmetry, or in simple terms the symmetry of mirroring a system along its spatial axes. Wu devised an experiment using radioactive Co-60 nuclei, exposing them to strong magnetic fields after cooling them to around 1 K. In combination, this would cause the nuclei to align along the magnetic field. The expectation was that if Parity (P) symmetry was conserved, the electrons from the beta decay of the radioactive nuclei would emit in an isotropic manner with no preferred direction. However the observations showed a strong asymmetry in the emission, with the electrons exhibiting a preferred direction of emission (Wu et al., 1957). Thus, she provided the world with the first evidence of Parity symmetry being violated in weak interactions. In an attempt to restore the apparent loss of order in nature, it was postulated that symmetry is conserved as charge-parity symmetry or CP symmetry. This implied that if you were to conjugate the charge along with the parity transformation, the symmetry would be conserved. But this idea was not to last. It was debunked by Cronin, Fitch and their coworkers in 1964 with their observation of the anomalous behavior of K mesons (Christenson, Cronin, Fitch, & Turlay, 1964). They devised an experimental setup where a beam of long lived K mesons were produced and allowed to travel a vacuum beam-line. The long-lived K_L mesons would decay much slower compared to K_S meson counterparts, and only the K_L decay products were expected to be found at the end of the relatively long beam line. But alas, the results indicated the presence of the decay products of the short lived K meson. This proved there was indeed a violation of CP symmetry in the weak sector, not just P symmetry. Cronin and Fitch won the Nobel Prize in 1980 for their discovery, but Madame Wu was excluded, possibly due to politics and the attitude toward women in Science at the time. Regardless of the politics, these three scientists had conclusively provided evidence that nature violated a fundamental symmetry. This phenomenon is referred to as CP violation and is now accepted as a part of the SM. In one final attempt to conserve symmetry we see the introduction of Charge Parity Time symmetry which allows the conservation of an overall symmetry with the inclusion of time. As of this point, CPT symmetry is still conserved in all known physical processes and also conserves the human notion of a grand underlying symmetry in the Universe.

With the discovery of CP violation in the weak sector, it was seen as completely allowed to assume this violation could also appear in other interactions in nature. Theory suggested that this violation might exist in the strong sector. This idea is fundamental when it comes to the narrative of the axion and ALPs. Referred to as the Strong CP problem, this is explored further in this chapter. In summary, we acknowledge that modern research has led us to understand that nature is not perfectly symmetric in all regards as we once believed, and at fundamental scales it sometimes exhibits behavior that might go against our common sense. The necessity for broken symmetries has one more important role when concerning fundamental physics. It helps us answer the simple question of how fundamental particles gain their masses?

2.1.4 Mass Terms

The concept of mass as we know in modern Physics began with Sir Isaac Newton in his work *Principia Mathematica*. He generally described it as the amount of matter in an object, or by its resistance to acceleration. Newton gave the definition of mass by stating that “the quantity of matter is the measure of the same, arising from its density and bulk conjointly” (Newton, 1687). For most commonplace applications in Physics, this definition still remains adequate. But when speaking of the fundamental building blocks of reality, we are forced to approach the concept with a different perspective. We see the beginning of a new era in the understanding of

mass when Einstein published his most popular Mass-Energy equivalence equation, described in the most simple way as $E = mc^2$ (Einstein, 1905). The implications of Mass and Energy being interchangeable with such a simple relationship may have been considered outrageous at the time, but today is something we essentially take for granted.

Beyond the notion that mass and energy had become an interchangeable property, when exploring the smallest observable scales we see the need for a different physical definition for the concept. The picture gets truly bizarre when we take the fundamental particles themselves and ask how they gain their mass. Attempts to describe the mass of fundamental particles started in the 1920s with Oskar Klein and Walter Gordon independently proposing what is now referred to as the Klein-Gordon equation in 1926. This is a relativistic wave equation which describes spin-0 particles quite well, but not spin- $\frac{1}{2}$ particles (Klein, 1926; Gordon, 1926). It was Paul Dirac in 1928 who succeeded in deriving a relativistic wave equation specifically for spin- $\frac{1}{2}$ particles that was consistent with both the theories of quantum mechanics and special relativity. His equation successfully described fermions like electrons and also predicted the existence of anti-matter through negative energy solutions (Dirac, 1928). This set the stage for QED and the Dirac field in QFT.

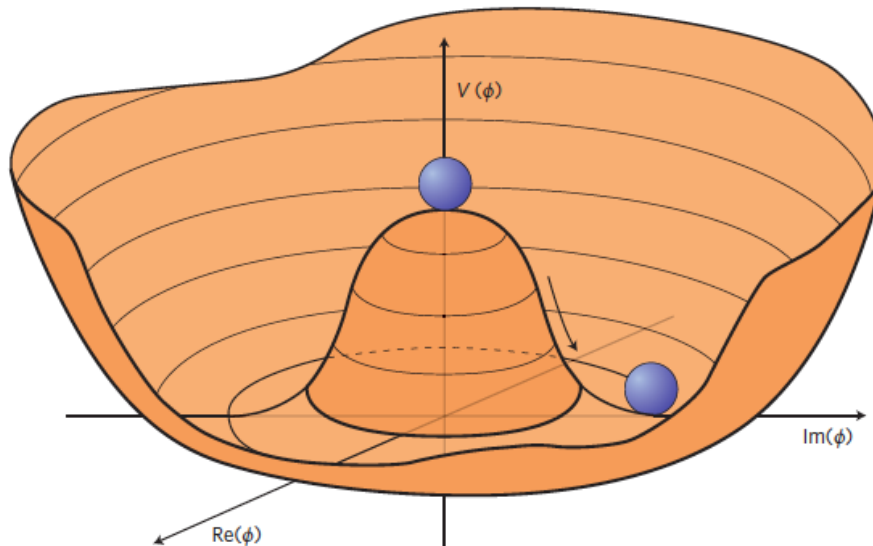


Figure 2.2: The Higgs Potential, shown as this Sombrero potential, where the global minimum can be any point along the “brim” of the hat. Credit: Ellis et. al. 2016

When we look at the Standard Model, mass generation is described primarily by the Higgs mechanism, with some possible exceptions. The Higgs mechanism describes mass generation of fundamental particles through spontaneous symmetry breaking (Higgs, 1964). It describes a scalar quantum field that pervades all space-time and has a non-zero expectation value in its ground state. Fermions gain their mass by interacting with this field through Yukawa couplings (Yukawa, 1955), giving them masses which are proportional to the vacuum expectation value of the Higgs field. Generally when writing out the mass term for a Dirac fermion, you include a right-chiral and left-chiral term for the particle. The physical implication of this being that a particle must change between these left and right handed states via interaction with the Higgs field. This is facilitated in the SM by an exchange of a weak hypercharge via interaction with the Higgs field. This weak hypercharge is imparted to left-chiral particles under the electroweak symmetry and is progressively gained and lost as the particle changes chiral states. To summarize, every massive fermion constantly interacts with the Higgs field, alternating its chirality between left and right states, thus impeding its free motion at luminal velocities. This forces

upon it a sub-luminal velocity, and thus an “inertia” which manifests to an observer as a mass. These fermions can be likened to a little quantum “clock”, ticking back and forth between two momentum states as it propagates through space-time, keeping its own time relative to a Universal Higgs field. Our observation of this ticking is as an apparent mass for the particle, separating these particles from the massless ones propagating freely at luminal velocity c . This narrative is of course limited to fermions, and not even all fermions at that. The neutrino is a source of controversy in the field, being how the SM predicts a massless neutrino, yet experimental evidence motivates phenomena such as neutrino oscillations (Pontecorvo, 1957) which cannot occur without specific neutrino mass eigenstates and their mixing. The mechanisms by which neutrinos gain mass, and their true nature is an on-going problem in Physics. This discussion is beyond the scope of our work so we do not explore this much further here.

Beyond the fermions, there remains one class of massive particles in the SM: the gauge bosons. Their masses are accounted for by the standard Higgs mechanism. These masses also arise from interactions with the Higgs field, but these are different from the fermion case. Simplistically speaking, spontaneous symmetry breaking of the electroweak symmetry generates the masses for the W^\pm and Z boson by the mixing of gauge fields. An illustration of a similar symmetry is given in Fig. 2.2. This plot visualizes the potential of the field after spontaneous symmetry breaking, and is referred to as the sombrero potential. This mechanism is able to account for the SM gauge bosons exactly, leaving no room for any more massive bosons. In the case of axions and ALPs, this poses a problem since these particles are expected to be massive. An exploration of how the axion/ALP might gain mass is done ahead in the “Axion/ALP mass” section. We see through our discussion, how while the SM framework elegantly explains a whole range of experimental observations, there are a number of rising observations it cannot accommodate.

2.1.5 Limitations

The culmination of QED, QCD and QFD, the Standard Model became one of the the most successful theories of physical reality, having one of the highest levels of predictability among all physical theories of reality thus far. With decades of effort from many brilliant minds, it stood the test of time for many years. Despite its success, the theory now finds itself at an impasse. Starting with the obvious, the Standard Model only manages to successfully describe 3 of the 4 fundamental interactions. While there are proposed QFT formulations for gravity, none have been experimentally validated or have gained enough traction to be considered accepted into the framework of modern Physics. Should there exist a quantum field for gravity, it requires the accompanied of a gauge boson carrying the gravitational force: the graviton (Blokhintsev & Gal’perin, 1934). This particle yet remains undiscovered with no strong indications as to its existence at the time this thesis is being written.

Another important failure of the Standard Model as it stands today is its inability to account for dark matter. There is an ever increasing amount of observational evidence which suggests the existence of dark matter including observations of galactic rotation curves, dampening of baryonic acoustic oscillations in the power spectrum of the CMB, the anomalous structure of the bullet cluster etc. While some alternative theories exists which attempt to explain these anomalous observations and keep the Standard Model from becoming obsolete, none of these have been experimentally motivated or accepted as of yet. Another failure appears in the inability to explain dark energy, which still remains a largely unexplored sector of physics with a now increasing momentum.

Additionally, the Standard Model fails to account for neutrino mass, predicting massless neutrinos as mentioned in the previous section. It remains unable to explain the vast scale gap

between the masses of elementary particles and the strengths of their interactions, often referred to as the hierarchy problem. It is yet unable to explain the matter-antimatter asymmetry in the Universe. The SM faces limitations when dealing with very high energies, such as that during the early Universe. The list of shortcomings of the SM is an ever growing one. Though our focus is on one particular shortcoming of the SM which lays the foundation for axions and ALPs.

2.2 Axions and ALPs

2.2.1 The Strong CP Problem

Following the foundational experiments by Madame Wu, Fitch and Cronin, CP violation in the weak sector was established firmly in the field of Physics. A logical follow up for this was to verify the existence of any similar violations in other sectors. From a purely theoretical standpoint, such a violation was also highly motivated for the strong sector. This appears as a CP violating term in the QCD Lagrangian, given as:

$$\mathcal{L}_{\text{QCD}} = -\frac{1}{4g^2} F_{\mu\nu}^a F^{a\mu\nu} + \sum_f \bar{q}_f (i\gamma^\mu D_\mu - m_f) q_f + \theta \frac{g^2}{32\pi^2} F_{\mu\nu}^a \tilde{F}^{a\mu\nu} \quad (2.3)$$

where $-\frac{1}{4g^2} F_{\mu\nu}^a F^{a\mu\nu}$ is the gluon kinetic term, where $F_{\mu\nu}^a$ is the gluon field strength tensor and g is the strong coupling constant. $\sum_f \bar{q}_f (i\gamma^\mu D_\mu - m_f) q_f$ is the kinetic term of the quarks, describing the quark fields q_f with masses m_f , where the sum is over quark flavors f . D_μ is the covariant derivative. Finally $\theta \frac{g^2}{32\pi^2} F_{\mu\nu}^a \tilde{F}^{a\mu\nu}$ is the CP violating term, where θ is the CP-violating parameter and $\tilde{F}^{a\mu\nu}$ is the dual of the gluon field strength tensor (Dine, 2001).

To experimentally verify the existence of CP violation in the strong sector, it was proposed that CP violation in these interactions would result in the observation of a permanent electric dipole moment in the neutron. And thus, Physicists set about attempting to measure the dipole moment of the neutron to verify the presence of a neutron dipole moment. The results showed that there was in fact practically no discernible permanent dipole moment in the neutron, at least not within the expected ranges which would indicate CP violation in the strong sector. The latest constraints have placed the neutron dipole moment at $|dn| < 3.0 \times 10^{-26}$ e cm (Abel et al., 2020). These results continue to contra-indicate the existence of any CP violation in the strong sector. The ongoing efforts of experimentalists demonstrate a clear lack of CP violation in the strong sector, and is described in the field as the ‘‘strong CP problem’’. The proposed solutions to this problem have some interesting consequences which shall become apparent as we proceed.

2.2.2 The QCD Axion

Experimental searches for CP violation in the strong sector appear to indicate a lack of any such violation placing limits much lower than would be allowed. In an attempt to fix the theoretical discrepancy with experimental results, in 1977 Roberto Peccei and Helen Quinn introduced a new U(1) global symmetry which is referred to as the Peccei-Quinn symmetry (Peccei & Quinn, 1977a, 1977b). They introduced their symmetry by promoting the CP violating term θ in the QCD Lagrangian to a dynamic term rather than a static constant term, consequently introducing a new field alongside their new global U(1) symmetry. This allowed the coefficient of the

CP violating term in the QCD Lagrangian to be dynamically set to zero, thus resolving the discrepancy.

Soon after in 1978, Frank Wilczek (Wilczek, 1978) and Steven Weinberg (Weinberg, 1978) predicted and formulated that through the promotion of the Peccei-Quinn symmetry to a quantum field and through spontaneous symmetry breaking, a new spin-0 particle emerges as a pseudo-Nambu-Goldstone boson. The particle through its interactions with gluons via the color anomaly term would lead to a potential which would then cancel out the CP violating term in the QCD Lagrangian. Wilczek suggested the name *axion* which is a popular detergent brand, since it “cleaned up” the strong CP Problem. Weinberg wanted to name the particle *Higglet* due its similarity to the Higgs boson, but it was ultimately the name axion which stuck. Weinberg was optimistic that the particle would be quite easy to find, but alas the search for these particles is still an ongoing effort in the particle and astro-particle Physics communities, almost 50 years since its prediction.

The field currently takes two approaches to the QCD axion model: the Dine-Fischler-Srednicki-Zhitnitsky (DFSZ) and Kim-Shifman-Vainshtein-Zakharov (KSVZ) models. The DFSZ model (Dine, Fischler, & Srednicki, 1981; Zhitnitskij, 1980) requires two Higgs doublets and imposes a charge on SM particles under the Peccei-Quinn symmetry. In this model the axion-photon coupling can vary over a wide range and it can be extended with additional Higgs doublets. The KSVZ model (Kim, 1979; Shifman, Vainshtein, & Zakharov, 1980) is a minimal hadronic model which introduces new heavy quarks. It doesn’t charge SM particles under the PQ symmetry and generally has a simpler structure than the DFSZ model. Both models are targeted with modern experiments and searches and are relevant in the field. Beyond the QCD axion models, there are other models which are also a subject of modern experiment: Axion Like Particles.

2.2.3 Axion Like Particles

While the QCD axion offered a great solution to the strong CP problem it was soon realized that axions and particles with properties similar to the axion could also be great candidates to solve another problem in Physics: dark matter. The QCD axion requires a specific relation between the particle’s mass and coupling to the EM field to be able to resolve the strong CP problem. But were we to relax this condition, we open up the possibility for a wide range of these parameters in our candidate particles, simply by setting aside the possibility of them solving the strong CP problem.

One particularly strong motivation for ALPs arises from string theory. In the framework of string theory, the compactification of extra dimensions on small manifolds is predicted to naturally lead to the emergence of additional pseudo-scalar and scalar fields. These fields could possibly have very small masses and could be identified as ALPs (Chadha-Day, Ellis, & Marsh, 2022). The string theory prediction of ALPs include the idea of something referred to as the “axiverse”, which postulates the existence of a large number of ultralight ALPs, along a wide range of masses (Ringwald, 2014).

2.2.4 Axion/ALP Interactions

Axions and ALPs are generally quite inert when it comes to their interaction with SM particles, making them incredibly hard to detect. On the other hand, this general inertness is also what qualifies them to be great dark matter candidates. When speaking of the specific interactions of hypothetical particles such as axions or ALPs, we maintain some amount of skepticism and

stay open to new and improved theoretical models consistently coming to light as research in the field progresses. While there is a growing number of predicted secondary interactions of axions and ALPs, our focus remains on the primary interaction which still remains prevalent in most axion/ALP searches: the Primakoff effect (Primakoff, 1951). This effect predicts a unique mixing of the axion with photons in the presence of strong electro-magnetic field resulting in an oscillation of the combined eigenstates. This is also treated experimentally as a conversion between photon and ALP states through a 3-vertex interaction where a virtual photon is provided by the EM field as illustrated in Feynman diagram in Fig. 2.3.

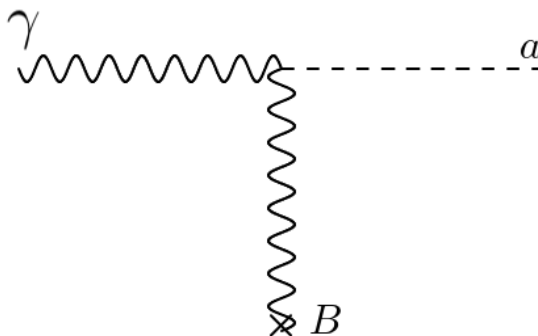


Figure 2.3: The Primakoff Effect, showing a 3-vertex interaction where a photon converts into an axion by interaction with a virtual photon, provided by an external EM field.

The Lagrangian for photon-ALP mixing as illustrated in the Feynman diagram is described in slightly varying ways depending on the publication and context, but it generally takes the form:

$$\mathcal{L} = -\frac{1}{4}F_{\mu\nu}F^{\mu\nu} + \frac{1}{2}(\partial_\mu a\partial^\mu a - m_a^2 a^2) + \frac{g_{a\gamma\gamma}}{4}aF_{\mu\nu}\tilde{F}^{\mu\nu} \quad (2.4)$$

where a is the axion field, $F_{\mu\nu}$ is the electromagnetic field tensor, $\tilde{F}^{\mu\nu}$ is its dual, m_a is the axion mass, and $g_{a\gamma\gamma}$ is the axion-photon coupling constant. This mixing and resulting oscillation leads to many interesting phenomena which may be observed across the Universe, wherever strong EM fields and photons are present. These secondary effects are exploited in the search for axions and ALPs, with many novel approaches being taken in highly sophisticated experiments across the world. Additionally, this interaction also allows for axion decays, provided the particle has high mass, a sufficiently high coupling constant and a decay constant with a reasonable lifetime where we might observe said decay (Overduin & Wesson, 2004) within the age of the Universe. The primary decay channel is to two photons, which may be detected in a number of ways. Though it is important to note here that this is largely model dependent.

In the context of the work we undertake, our concern is primarily regarding photon/ALP superpositions propagating across Cosmological distances and the secondary effects which arise from their mixing in the presence of vast astrophysical magnetic fields. In order to model and predict the behavior of the particle, we apply equations of motion concerning the ALP. These offer us a calculable description of how these particles propagate through our Universe, particularly in the presence of magnetic fields. As dictated by the Primakoff effect, the dynamics of the particle are altered when in the presence of an external magnetic field causing a mixing of

photon and ALP states. This consequently leads to an oscillation between states as the particle propagates. The dynamics of this oscillation effect is described by the equation:

$$i \frac{d}{dz} \Psi(z) = \mathcal{M}_0 \Psi(z) \quad (2.5)$$

where $\Psi(z) = (A_x(z), A_y(z), a(z))^T$ represents the photon polarization states assuming propagation in the z direction along with the ALP field, and \mathcal{M}_0 is the mixing matrix which determines the photon-ALP oscillation (Raffelt & Stodolsky, 1988). We can note here the similarity in its dynamics to neutrino oscillations (Pontecorvo, 1957) which are also described using a mixing matrix of their own, and results in an oscillation effect between neutrino eigenstates as the particle superposition propagates through spacetime. Though, it is important to note that there is a distinct difference between the two when regarding the origin of this oscillation effect. While ALP oscillations are dictated by the mixing of photon and ALP states in the presence of an external magnetic field, neutrino oscillations arise as a consequence of the mixing of the different neutrino mass eigenstates.

When applying the ALP equations of motion to our study cases, we tend to describe the interaction with a conversion probability. This enables us to express the complex dynamics of these oscillations in a predictive observational model. This conversion probability is described for a simple homogeneous magnetic field using the equation:

$$P_{\gamma \rightarrow a}(E, z) = \left(\frac{g_{a\gamma\gamma} B_T l_{osc}(E)}{2\pi} \right)^2 \sin^2 \left(\frac{\pi(z - z_0)}{l_{osc}(E)} \right) \quad (2.6)$$

where $g_{a\gamma\gamma}$ is the ALP-photon coupling constant, B_T is the transverse component of the magnetic field, z is the position, z_0 is the initial position, E is the Energy, and $l_{osc}(E)$ is the photon-ALP beam oscillation length (Raffelt & Stodolsky, 1988). While this equation defines a simple case, in the systems we observe we deal with complex and inhomogeneous magnetic field models and must account for these as best we can. To calculate the photon survival probability in these more complex cases including multiple turbulent models within our total model requires a more rigorous approach. This is implemented through the use of the open source software package *gammaALPs* (Meyer, Davies, & Kuhlmann, 2021) which we implement for our model construction and ALP modeling. The methodology implemented by the software treats the different magnetic field environments along the propagation path as different domains. A transfer matrix represents the solution for the photon-ALP equations of motion in a given domain/environment $m = 1, \dots, M$ and is implemented such that $m = 1$ indicates the environment closest to our source. Thus, the total transfer matrix is given by:

$$T_{tot} = T_N \cdot T_{N-1} \cdot \dots \cdot T_2 \cdot T_1 \quad (2.7)$$

where given each environment m in our model, they make an assumption that each path can be split into N_m consecutive domains, where the magnetic field, ψ , electron density, and dispersion terms χ are constant in each domain. In this manner, the software then calculates the conversion probability using the formula:

$$P_{\gamma\gamma} = \text{Tr} \left[(\rho_{11} + \rho_{22}) T_{\text{tot}} \rho(0) T_{\text{tot}}^\dagger \right] \quad (2.8)$$

where $\rho_{11} = \text{diag}(1, 0, 0)$, $\rho_{22} = \text{diag}(0, 1, 0)$, $\rho(0) = \text{diag}(1/2, 1/2, 0)$ for an un-polarized beam, and T_{tot} is the total transfer matrix. A detailed explanation of the various methods implemented in *gammaALPs* is available in the associated publication as cited above.

Using this more complex conversion model enables us to make more effective predictions of our observed events, and is thus seen implemented in various studies concerning ALP searches. When searching for verification of any theoretically predicted particle including ALPs, we attempt to model and predict behavior based on often new and exotic physics. This also implies the necessity to conduct our searches with plenty of room for variation and improvement upon the model. Further, in order to accommodate the particle model into our existing theoretical frameworks, we must also be able to account for various predicted properties and parameters of the candidate particle.

2.2.5 Axion/ALP Masses

The mechanisms by which most particles in the Standard Model gain mass have been well established. Unlike most fermions with $\frac{1}{2}$ spins, bosons in the SM do not gain their mass by interaction and exchange of weak hypercharge with the Higgs field. The standard Higgs mechanism accounts exactly for the masses of all SM bosons through electroweak symmetry breaking. This leaves no room for another boson(s) such as the axion/ALP to gain a mass via the standard Higgs mechanism. As already mentioned earlier in the chapter, an important exception is the neutrino which represents a unique case. The specific case of the neutrino is complex and interesting, but not within the scope of this discussion.

When considering axions and ALPs, these particles are described by theory as pseudo-Nambu-Goldstone bosons, implying they carry a mass unlike typical Nambu-Goldstone bosons. True Nambu-Goldstone bosons are massless and arise when a spin-zero boson moves freely around the global minimum in a Sombrero potential. This is visualized as a free motion along the “brim” of the sun hat as illustrated in Fig 2.2. While it is viable for a spin-1 particle to gain mass by mixing with another spin-1 particle (Ellis, Gaillard, & Nanopoulos, 2016), the spin-0 axion/ALP and its mass cannot be explained in a similar way. Therefore theorists have suggested alternate means by which these particle might gain mass.

The primary explanation of the mechanism by which axions and ALPs gain mass involves spontaneous symmetry breaking of the global U(1) symmetry introduced for the axion/ALP field. At high energy scales, the axion or ALP begins as a massless Nambu-Goldstone boson and after spontaneous symmetry breaking, non-perturbative effects generate a potential for the axion/ALP field. This leads to a small mass for the particle. By this mechanism, the QCD axion mass is described using the following equation (Adams et al., 2022):

$$m_a = 5.69(1.51) \mu\text{eV} \left(\frac{10^{12} \text{ GeV}}{f_a} \right) \quad (2.9)$$

where f_a is the axion decay constant, and it incorporates factors like the pion mass, pion decay constant, and up and down quark masses.

When concerned specifically with ALPs, string theory offers possible mechanism by which it may gain mass. The mechanism follows specific compactifications and Non-Abelian group effects similar to that in QCD which contribute to the potential. This predicts that the ALP mass would be sensitive to instanton action and can lead to wide range of possible ALP masses (D. J. Marsh, 2017). A detailed discussion of these mechanism is highly complex and beyond the scope of this work which is primarily focused on verification and not fundamental theory. For those interested, many publications are available excluding the ones already mentioned which describe these theoretical mechanisms in great depth.

2.3 AGN and Blazars

2.3.1 Early Observations

The story of AGN observation begins in the 1900s, with the first notable events happening quite early. In 1908, Edward Fath made a series of landmark observations at Lick Observatory, attempting to understand the nature of what they categorized as “spiral nebulae”, now known as galaxies (Fath, 1909). He performed spectrographic studies and discovered emission lines from NGC 1068 observing that it had a composite spectrum composed of emission and absorption lines. This is considered the first historical detection of emission lines from an AGN. He also made observation of Messier 81. In 1918, Heber Curtis reported the first AGN jet from his observations of Messier 87 (Curtis, 1918). He observed what he described as a curious straight ray. He was also working at the Lick Observatory at the time and the true nature of what he observed was yet not understood. A turning point for the field came in 1943 when Carl Seyfert published a highly influential paper (Seyfert, 1943), in which he described his observations of nearby galaxies with bright nuclei and uncharacteristically broad emission lines. This began the classification of Seyfert galaxies.

The field picked up pace after the invention of radio telescopes in the 1950s, which led to the rapid advancement of AGN research. Early detections include Messier 87 and Centaurus A. The 3C radio survey then led to the discovery of many new radio sources and their optical counterparts. The modern understanding of AGN really started taking shape after Maarten Schmidt identified the first quasar, 3C 273 in 1963. In the early 1950s, Viktor Ambratsumian introduced the concept of AGN to the field, putting forth the idea that galactic nuclei could contain highly massive bodies, which were still not known to be black holes at the time. Here begins the modern era of AGN research and we have since observed many such sources and understand them with greater depth and a growing collection of supporting data.

2.3.2 Modern Understanding

Active Galactic Nuclei, by modern definition are compact regions located at the center of galaxies, which emit a significant amount of energy which exceeds the energy emitted by the stellar population of the galaxy itself by far. These objects are some of the most energetic and luminous sources discovered by us in the known Universe. The energy generated by these monstrous sources is emitted and observed across the EM spectrum, spanning radio, infrared, optical, X-ray and γ -rays.

An AGN primarily consists of a supermassive black hole (SMBH) surrounded by an accretion disk, with active accretion taking place. This constant accretion leads to the formation of jets along the magnetic axis of the SMBH, spewing high energy, high velocity particles into the Universe. These jets often extend far beyond their host galaxy and emit a high amount of radio

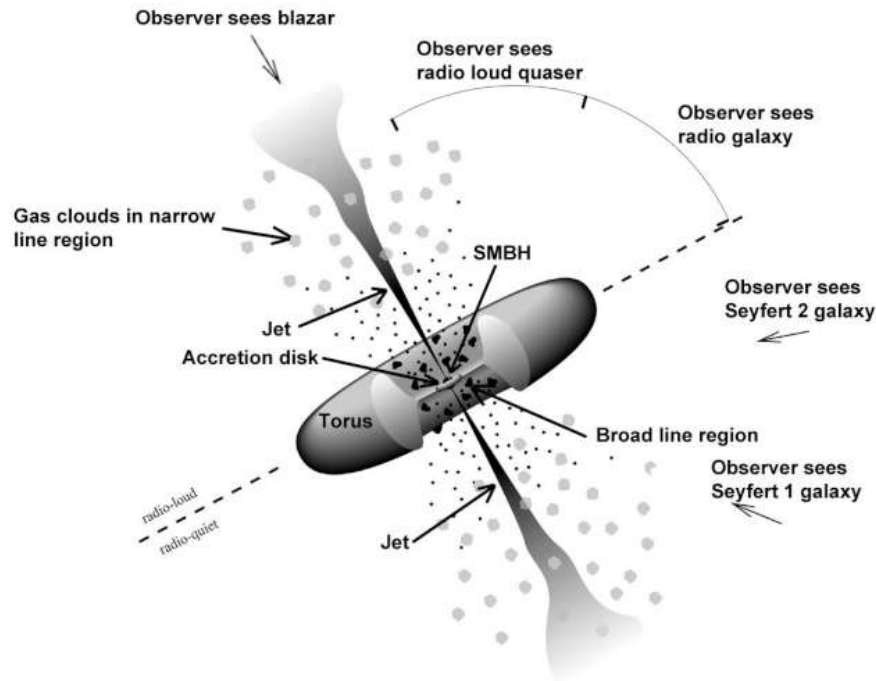


Figure 2.4: The typical structure of AGN, illustrating its various components in a unified manner. What we observe depends on our viewing angle. Credit: Fermi, NASA.

waves. Besides these primary components, AGN also usually include a torus of dust and gas surrounding the accretion disk. This dusty torus often obscures the central regions of the AGN, posing challenges for our instruments to directly probe this region. When speaking from an observational perspective, an AGN usually has two main ionic emission regions: the broad-line and narrow-line regions. The broad-line region is located closer to the central SMBH and emits broader lines due to the higher density and velocity of the ionic gas, while the narrow-line region is located farther out, is less dense and moves at lower velocities.

Our primary interest in these sources is their VHE γ -ray emission which can be predicted and modeled fairly well. These sources often vary greatly in their states of activity, often “flaring” and emitting a large amount of energy in the highest ranges of the γ -ray spectrum, well into the TeV scale. These flares are understood to be set off by numerous processes including a spike in the accretion rate, changes in jet structure, tidal disruptions, binary SMBHs at the center etc. The field of AGN research is vast and deeply interesting, but discussion of this is beyond the scope of this work.

When it comes to our observational classification of these AGN, how they have been historically categorized depended largely on the angle at which we viewed the source. It was only with a growing understanding of the sources, that we could categorize them all under the same title of AGN. The first classification method came from Seyfert as discussed above. Seyfert galaxies are characteristically those with bright nuclei and broad emission lines. Then came quasars, which are extremely powerful, luminous AGN located at high redshifts. After this we see the emergence of radio galaxies, characterized by their strong emission in the radio wavelengths, often having large jets and lobes. Blazars are some of the brightest known sources, which we now understand to be AGN with their jets aligned to our line of sight, beaming directly at us. This causes relativistic beaming and rapid variability in our observations of the source. These objects include BL Lacertae objects and Flat Spectrum Radio Quasars (FSRQs). More recently, we see the appearance of Machine Learning based classification methods, but this is a

field which is only just gaining traction at time this Thesis is being written.

2.4 The Extragalactic Background Light

2.4.1 Origin & Contributions

When speaking of the Universe and its possible constituents, one of the most abundant particles present across our vast Universe is the photon. At the end of the Cosmic dark ages, the first stars collapsed from cosmic gas clouds, emitting stellar light, sent streaming across the vast expanse of space-time for the first time since the Universe itself began. But long before this, electromagnetic radiation of other wavelengths, predominantly in the form of thermal radiation, was already abundant in the early Universe. This radiation is initially trapped within the primordial plasma of the early Universe, trapped in the highly dense and hot environment, until eventually the Universe condenses enough for the light to stream freely across the Universe as it cools to form more stable structures like the first galaxies and stars. A significant fraction of all photons emitted since the Universe became optically transparent still stream freely across spacetime as it expands. The longer they are able to stream without interaction, the more they get red-shifted over Cosmic time. A significant fraction of these photons are also absorbed and re-emitted as infra-red radiation by vast dusty nebulae. As the Universe evolves, more stars are created and destroyed in an ongoing cycle. Galaxies evolve and the cosmic web becomes more intricate, with dark matter driving structure formation. Large voids and dense packets of mass develop in juxtaposition across the Universe. Many processes lead to the generation of a constantly evolving background of photons across space-time. This photon background contains within it information of the entire history of our vast Universe. Photons across all wavelengths contribute toward this background and are collectively referred to as the Extragalactic Background Light, or EBL. Each energy/wavelength/frequency range is referred to by specific terms to categorize them. Of these, perhaps the most well known is the Cosmic Microwave Background or CMB. As the name suggests this refers to the EBL within the microwave range of energies. When dealing with the EBL the primary interest is usually regarding two major regions: the Cosmic Optical Background (COB) and the Cosmic Infra-red Background (CIB).

The various contributions to this vast cosmic background can be broadly categorized as: Stellar, Dust and AGN, with other lesser contributions from various sources. Stellar light is one of the largest contributors to the EBL, constituting the majority of the COB. This is composed of all free streaming stellar light emitted into the Universe since the first stars collapsed and ignited fusion in their cores. The next major contributor is absorbed stellar light re-emitted as thermal photons from Cosmic dust clouds, contributing largely toward the CIB. Active galactic nuclei are some of the brightest and most energetic objects in the Universe, contributing to the EBL across various ranges in the EM spectrum. There are also many other minor contributors, essentially being any object in the Universe which emits light, but for the sake of modeling the EBL we tend to neglect insignificant contributors.

2.4.2 Existing Models

The EBL is a crucial component when modeling and studying high energy sources, particularly at high redshifts. One key consequence of this photon background is the attenuation of VHE γ -ray photons as they propagate through this background of photons, leading to a functional “opacity” of the Universe to these high-energy photons. The ability to model γ -ray opacity and the clear nature of the attenuation of these photons is key to modeling and studying these

types of sources and their intrinsic behavior. There have been various models developed for the EBL and there are many competing models currently visible in the field. Each model tends to perform better in certain aspects, keeping many of these models relevant and also making the choice of EBL model important depending on the nature of the study being undertaken.

Each models tends to cover wide, but specified range of wavelengths, or have a range at which they perform ideally. Many models like Finke (Finke et al., 2022) track parameter evolution with redshift. This opens the door to study the evolution of the EBL through Cosmic history. The models also might vary on the way they treat dust absorption and re-emission. Other relevant models include Dominguez (Dominguez et al., 2011), Franceschini (Franceschini, Rodighiero, & Vaccari, 2008), Saldana-Lopez (Saldana-Lopez et al., 2021), Kneiske (Kneiske & Dole, 2010). We explore the specifics of certain models further in the context of our work with the EBL in upcoming chapters.

Chapter 3

Experimental Foundation

3.1 VHE γ -ray Astronomy

3.1.1 History & Development

Long before the detection of the first astrophysical γ -rays, their existence was already theorized by Scientists. Henry Primakoff, Eugene Feenberg (Feenberg & Primakoff, 1948) and later Sachio Hayakawa and I.B. Hutchinson in 1952 theorized the interactions of cosmic rays with stellar light and interstellar and intergalactic gas, which would result in the production of γ -rays. In 1958, Phillip Morrison laid the foundations for γ -ray production in Supernova explosions (Morrison, 1958). These violent explosions release tremendous amounts of energy into the Universe, part of which is emitted in the form of γ -rays. The production of γ -rays was also theorized to occur due to interactions between energetic electrons and astrophysical magnetic fields, resulting in synchrotron emission. Though the theoretical motivation for astrophysical γ -rays was strong, and the potential for Astronomy with these high energy particles was a tantalizing concept, the development of the field faced many challenges. The primary roadblock toward the development of γ -ray Astronomy was the simple fact that nearly all γ -rays are absorbed by the Earth's atmosphere. This made it seemingly impossible for ground based telescopes to detect these high energy messengers from the depths of the Universe. Overcoming this obstacle, the first γ -ray telescope was launched into orbit in 1961 aboard the Explorer 11 satellite. This telescope was able to detect fewer than 100 γ -ray photons.

The first significant detection of γ -rays came with the OSO-3 satellite which was able to detect extragalactic photons for the first time (Brandt, 1969). This set the stage for the ensuing exploration of the high-energy Universe and the evolution of the field of γ -ray astronomy. The launch of satellites such as SAS-2 (Fichtel, Kniffen, & Hartman, 1973) and COS-B (Bignami et al., 1974) in the 1970s pushed the field forward by providing for the first time, detailed maps of the γ -ray sky. They managed to identify numerous point sources, though the resolution of the instruments was not significant enough to be able to connect them to specific known sources. However this represents a fundamental obstacle for γ -ray telescopes. The very high energy of these particles makes it functionally impossible to focus these particles by conventional means. The use of any sort of lens or mirror for focusing is impossible as the photons readily interact with the atoms in the device and are lost in the process. This requires new approaches to be developed toward the field of γ -ray astronomy, different from conventional techniques implemented in astronomy.

In the narrative of γ -ray astronomy, an unexpected discovery came to us in the form of γ -ray bursts. The detection was first reported from an unlikely source: the Vela constellation of military satellites. These satellites were initially launched by the U.S. in the 1960s to monitor

nuclear activity on the Earth’s surface, ensuring compliance with the Nuclear Test Ban Treaty. Their detection of short bursts of γ -rays from deep space was initially a great mystery, but eventually led to our discovery and understanding of GRBs in the Universe. With the foundations built for the field, more resources and focus came to γ -ray astronomy and astrophysics paving the way for the modern field that we see today.

3.1.2 Current Status

The start of modern γ -ray astronomy is marked by the deployment of the Compton γ -ray Observatory (Gehrels, Chipman, & Kniffen, 1994) launched in 1991 and the Fermi γ -ray Telescope (Thompson & Wilson-Hodge, 2022) in 2008. Alongside these, we see the emergence of a groundbreaking new approach to γ -ray Astronomy using Cherenkov Telescope Arrays. This method of detecting γ -rays relies on the detection and reconstruction of Cherenkov radiation emitted by cascade particles resulting from γ -ray interactions in the upper atmosphere. This new detection methodology, combining approaches from particle and astrophysics, allowed us to overcome the limitations posed by the atmosphere for ground based detectors. The first functional Cherenkov telescope array was the Whipple 10 m telescope (Kildea et al., 2007). As a pioneering breakthrough in 1989, Whipple detected the Crab Nebula with a clear signal above 1 TeV. The Whipple telescope was succeeded by instruments such as H.E.S.S. (Pühlhofer, Leuschner, & Salzmann, 2024), MAGIC (Bigongiari, 2005) and VERITAS (Holder et al., 2006) which represent the current generation of IACTs. With the operational lifetimes of these pioneering telescopes slowly drawing to an end, there are many new telescopes on the horizon like the CTAO (Hofmann & Zanin, 2024).

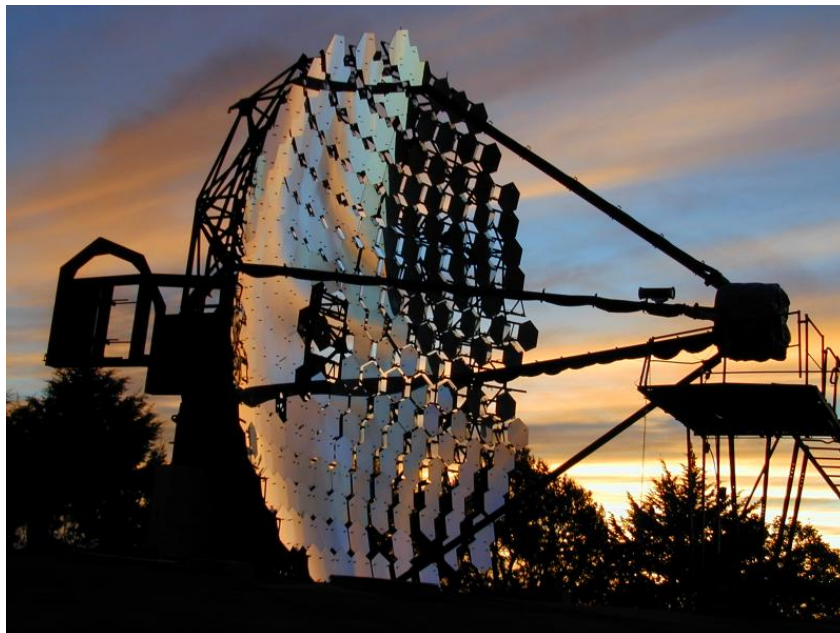


Figure 3.1: The Whipple 10m Telescope in Arizona. A first of its kind Imaging Atmospheric Cherenkov Telescope. Credit: VERITAS Collaboration

Armed with an extensive set of detection instruments, the field of γ -ray astronomy is currently growing at an immense rate with more advanced instruments still on the horizon. We are able to observe the high-energy Universe with unprecedented depth and accuracy. With this, our understanding of various high energy phenomena like Supernovae, black hole mergers, neutron star mergers and many more are advancing at breakneck pace. What lies ahead is a truly exciting time for the field, and we stand on its precipice.

3.2 Axion/ALP Searches

3.2.1 Lab Searches

The hunt for the hypothetical class of particles under the umbrella of axion and ALPs has now been ongoing for decades. With the goal of direct detection of the particle, many experiments across the globe have developed their own approaches to face the seemingly Herculean challenge. Each of these experiments aims to exploit specific interactions of the candidate particle with known SM particles. A significant fraction of these approaches follow various secondary effects which are expected to appear as a consequence of the Primakoff effect (Primakoff, 1951) as discussed in the Theoretical Foundations chapter.

One of the flagship experiments for axion/ALP searches is the Any Light Particle Search (ALPS) and its successor ALPS II (Bähre et al., 2013). These experiments follow the “shining-light-through-a-wall” approach for their searches, attempting to convert laser photons to axions/ALPs via an artificially generated magnetic field. This would allow them to penetrate an otherwise impenetrable barrier, passing through to the other side where an attempt is made to re-convert them into photons for detection.

Other novel approaches taken toward the search for axions/ALPs include interferometer based searches like WISPMI (Batllori, Gu, Horns, Maroudas, & Ulrichs, 2023), qubit based searches (Moretti et al., 2024; Dixit et al., 2021) and measurements of atomic clock deviance (Alonso, Blas, & Wolf, 2019). The ingenuity found in the approaches to such searches are very interesting with new ideas being conceived and applied even at this time. The growing efforts of a global community will hopefully lead us toward the ultimate verification of the existence of this class of particles.

3.2.2 Astrophysical Searches

The search for axions and ALPs takes broadly two approaches. While laboratory experiments allow us to do extremely precise searches within strictly controlled environments, there always exist limitations concerning the availability of resources and sufficiently advanced technology. Generating extremely low temperatures, extremely high energies, strong magnetic fields etc. is often simply not feasible given the current level of human advancement. Therefore an alternate approach to search for elusive theoretical particles is to exploit extreme systems which occur naturally in the Universe. This approach pioneered the rise of Astro-particle Physics. This term generally refers to research approaches which utilize naturally occurring systems in deep space which can be exploited to conduct particle research which could otherwise not be conducted in ground-based or orbital labs. The inherent challenge accompanying these approaches concerns our ability to model away natural systems which cause background and foreground noise. These sources of interference are difficult to model and often lead to results being highly model dependent. Additionally the systems themselves are difficult to model with reasonable accuracy, considering most natural systems have an apparent chaotic nature.

There are various approaches taken to searching for axions and ALPs under the astrophysics paradigm. One popular approach in the field searches for keV range axions expected to be produced in the Sun in processes such as PP chains and the CNO cycle, analogous to that of other particles such as neutrinos. Referred to as *helioscopes*, these highly specific detectors include notable experiments such as CAST (Aalseth et al., 1999), IAXO (Armengaud et al., 2019), BabyIAXO (Abeln et al., 2021). Beyond our local star, some researchers conduct studies expecting thermal loss in stars beyond that via neutrinos, through axion channels. A

review of these types of experiments is given in (Giannotti, Irastorza, Redondo, Ringwald, & Saikawa, 2017). Yet another “stellar” approach toward axion/ALP searches involves searching for signatures from neutron stars and pulsars by virtue of their extremely strong magnetic fields (Pshirkov & Popov, 2009). Various other astrophysical approaches and their current status have been reported in (Caputo & Raffelt, 2024).

The specific properties of axions/ALPs make them promising candidates for dark matter particles. Assuming them to be as such opens the door for various search methodologies in this context. A category of detectors termed *haloscopes* explore the potential for the search of local axionic dark matter. Following the original concept proposed by Sikivie (Sikivie, 1983), these detectors aim to covert axions into photons using magnetic fields and resonant cavities. Notable experiments include, but are not limited to, ADMX (Asztalos et al., 2010), MADMAX (Caldwell et al., 2017), HAYSTAC (Brubaker, 2018) and CAPP (Adair et al., 2022). Beyond local dark matter searches, some studies attempt to detect signatures of axions/ALPs via their decay over Cosmic history (Balázs et al., 2022; Guerrero & Rigolin, 2023). There was also one interesting study which explored nuclear decay anomalies to constrain axion dark matter (Zhang, Houston, & Li, 2023)

Through the various methodologies developed by teams worldwide, astrophysical searches are a driving force in placing constraints over the axion/ALP parameter space. With many novel approaches still appearing in the field, there are competing ideologies and experimental methods pushing the field forward. Only time will tell what new innovations might lead us to an ultimate verification of our hypothetical particle.

3.3 EBL Measurements

3.3.1 Direct Measurement

The direct measurement of the EBL is not a viable option given our current technological advancement. Any measurements made of background light from within the solar system is overwhelmed by Zodiacal light and interplanetary dust. If we were to make a measurement from beyond the solar system we would face significant noise from galactic light produced by neighboring stars. There have been attempts to make direct measurements regardless, by modeling and excluding these components, but these are often accompanied by large uncertainties.

One notable direct measurement came from the New Horizons probe (Zemcov et al., 2017). The New Horizons probe offers a unique opportunity, currently being located beyond the orbit of Pluto. This vastly reduces the Zodiacal and interplanetary dust foreground. This measurement was focused on the COB part of the EBL, predicting that the EBL is twice as bright as expected by prevalent models. This result is seen as controversial and in conflict with indirect measurements.

3.3.2 Indirect Measurement

When considering EBL measurements, the more practical approach is to make indirect measurements of it, thus circumventing the vast experimental challenges of direct measurements. There are a few approaches generally taken toward this: γ -ray absorption, large sample analysis, optical depth reconstruction, spectral intensity measurement, galaxy count surveys, redshift evolution studies etc. Various studies have been conducted using telescopes like Fermi-LAT (Biasuzzi, Hervet, Williams, & Biteau, 2019) and H.E.S.S. (Abdalla et al., 2017), with more studies currently ongoing toward measuring and constraining the EBL across all wavelengths.

These measurements are generally seen as preferred and tend to indicate a lower EBL intensity than direct measurements. There are on-going efforts to advance both direct and indirect measurements with a growing number of techniques and instruments at our disposal and their apparent disparity is quickly being bridged. The field is currently very active with many new publications on the horizon.

Chapter 4

Instrumentation

4.1 The H.E.S.S. Array

The High Energy Stereoscopic System or H.E.S.S. telescope array, located in the Khomas highlands of Namibia is an Imaging Atmospheric Cherenkov Telescope (IACT) array. It utilizes multiple mosaic telescopes arranged in an array to optimize its detection ability. The stereoscopic view of the air showers provided by the array enables a highly precise reconstruction. Being located in the Southern Hemisphere, it has the ability to observe the galactic disk and center. The telescope was initially installed in 2003 with four small 12 m telescopes. The initial plan was to construct another twelve telescopes of similar dimensions, but this plan was scrapped in lieu of constructing and installing a large 28 m telescope in the center of the array. The smaller telescopes are referred to as CT1-4, while the large central one is given the name CT5.

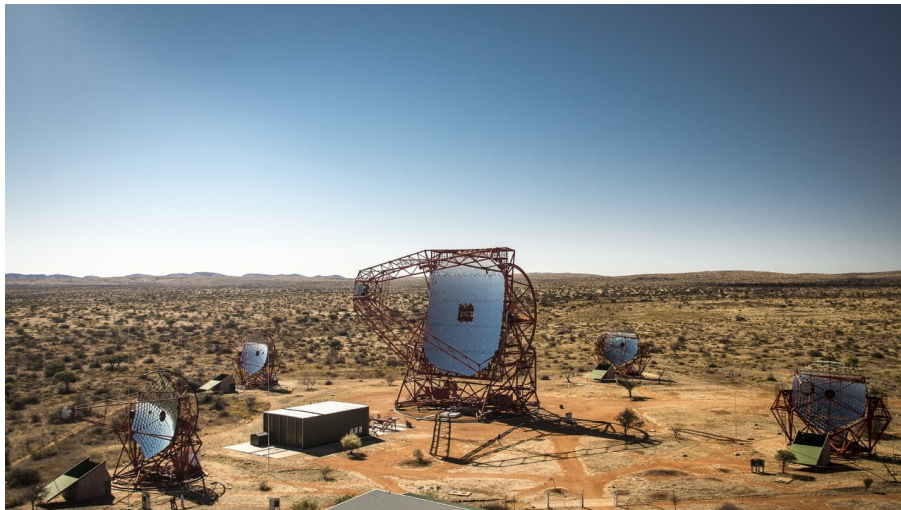


Figure 4.1: The H.E.S.S. Telescope Array with CT1-5 in the Khomas Highlands, Namibia. Credit: Christian Foehr, H.E.S.S. Collaboration

IACTs are in some ways similar to particle detectors, making them more than just a conventional telescopes which make direct observations of the incoming signal photons. Invented to circumvent the limitations of high energy astronomy due to the high rate of interaction of γ -rays with the Earth's atmosphere, these telescopes rely on detecting Cherenkov radiation emitted by the products of the high energy particle interactions in the upper atmosphere. High energy particles like γ -ray photons or cosmic rays interact readily with the atmosphere, generating

a cascade of particles which rain down toward the surface. Depending on the nature of the incident particle, a specific set of new high energy particles are generated in the interaction. In the case of a high energy γ -ray interacting with the atmosphere, the process begins with pair production by interaction between the incident photon and an atmospheric particle. The electron and positron produced via this interaction emit radiation through bremsstrahlung (braking radiation), by interaction with the electric fields of neighboring nuclei. These secondary photons can then in turn produce more electron-positron pairs which undergo radiative braking themselves and so on, leading to a cascade of particles showering down onto the surface, slowly dissipating away the energy of the original photon. This is illustrated in Fig. 4.2.

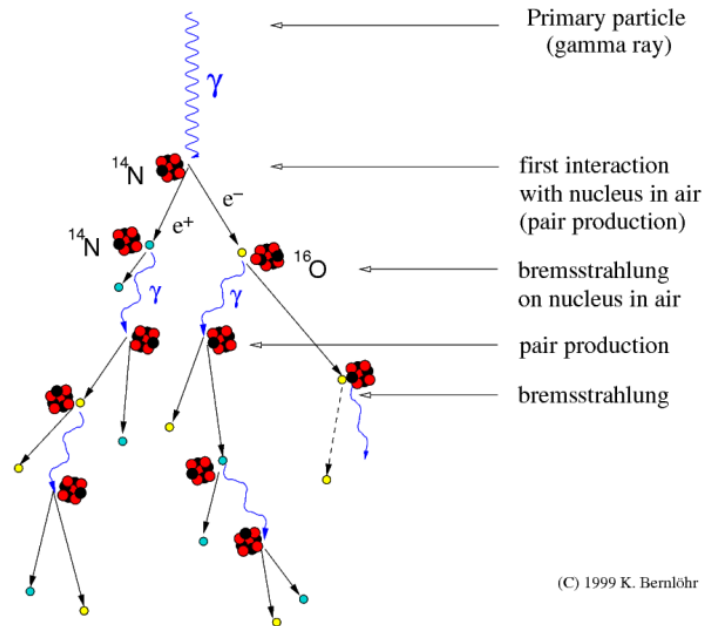


Figure 4.2: An illustration of the cascade formed by an incident γ -ray in the atmosphere by an alternating chain of pair-production and bremsstrahlung. Image credited to Konrad Bernlöh (1999).

These highly energetic, charged particles travel through the atmosphere at velocities exceeding the speed of light in air. This conditional “super-luminal” propagation does not violate the Universal speed limit of c as imposed by special relativity, and leads to the emission of Cherenkov radiation in the form of light cones, with a large fraction of its energy emitted in the UV range. This effect can be compared to the formation of a sonic boom when an object breaks the sound barrier. These Cherenkov light cones appear in faint and short bursts, on the order of nano- to micro-seconds, rendering them invisible to the naked eye. It is these light cones that the IACT can detect from the ground, usually with the help of photo-multiplier tubes. They reconstruct the light cone and determine the trajectory and energy of the original particle. In essence, an IACT is thus an astronomical particle detector which utilizes the atmosphere as a scintillator and not a conventional telescope which focuses incoming photons onto a camera using refractive or reflective optics.

The large mosaic mirrors of each telescope in the H.E.S.S. array collect the Cherenkov radiation from such atmospheric particle showers and reflect it into UV sensitive cameras installed along their focal plane. While CT1-4 house the same cameras, CT5 has its own camera. All of the cameras have received major updates during their service lifetimes. In each of the cameras, a combination of Winston cones and photo-multiplier tubes help generate a signal which is

then sent onward through a sophisticated system of electronics. The resulting information can then ultimately be used for reconstruction and further research. This intricate and ingenious setup allows H.E.S.S. to observe photons between 50 GeV and 100 TeV approximately. It has an angular resolution of $\sim 0.08^\circ$. For more technical details and general information regarding the telescope, please refer to the 2024 article published by the H.E.S.S. Collaboration which provides a detailed overview (Pühlhofer et al., 2024).

4.2 Data Handling

For the process of data reduction and analysis we utilize various software tools. H.E.S.S. data analysis is typically done along one of two analysis chains: the Heidelberg chain or the Paris chain. For our analysis, we follow the Heidelberg chain and access data through the archives maintained at the computational cluster in Heidelberg. It is operated and maintained by the Max Planck Institute. All data is required to be cross checked with the Paris chain before presentation and/or publication. This process is carried out for all datasets utilized for our work, complying with all collaboration requirements. While H.E.S.S. analysis is usually performed on the Heidelberg cluster using the proprietary software tool-set referred to as HAP tools, we focus on a newer approach to H.E.S.S. and γ -ray analysis in general: *gammapy* (Donath et al., 2023). This is an open source Python package aimed at simplifying data analysis in γ -ray astronomy. This package which is still under development and undergoes regular updating. The analysis for our work began before the release of the first stable version, but continued on into the first release, with our analyses being updated to conform to changes made with the release of *gammapyv1.1*. Additionally, custom higher level tools were developed by myself using the low level framework of *gammapyv1.1*. This involved fixing existing bugs, simplifying work flow and improving the reproducibility of our analyses. It additionally provides methods for bookkeeping and other “quality-of-life” features to make analyses more intuitive, interactive and simple. This customized high level interface has been made available on GitHub, and can be accessed upon request.

One important note regarding *gammapy* analysis has to do with the fact that the observations available for use with *gammapy* are generated and made available by the collaboration in the form of FITS files (Nigro et al., 2019) stored in the cluster database. Observations are made available in this form after standard cuts have already been applied to them by collaboration members. These cuts range from hard to standard and loose cuts. The choice of cut for analysis is made depending on the type of source being observed. Standard cuts are optimized for sources with a flux level of $\sim 10\%$ of the Crab Nebula’s flux. Hard cuts for those with $\sim 1\%$ and loose cuts for those with above 100% . A zeta cut configuration is also available, which categorizes and filters gamma-like events from cosmic ray or background events using a zeta parameter. In the process of making these FITS files for *gammapy* usage, often some observations face errors and are unavailable for use. This results in a reduced run-list as opposed to the original run-lists generated using HAP tools. Thus, it is often expected that we observe a difference in the final observations hours, counts and other values between a HAP based analysis and a *gammapy* analysis.

For the purpose of ALP related simulation work, we utilize the open source Python framework *gammaALPs*, created by Manuel Meyer, Jamie Davies and Julian Kuhlmann along with other contributors (Meyer et al., 2021). This framework is an actively updated software framework, with new models and updates being applied even at the time of this thesis being written. The software package houses built-in methods to solve axion/ALP equations of motion, while accounting for various astrophysical magnetic fields with built-in modeling methods. We implement *gammaALPs* based calculations in our work consistently. This includes the utilization

of methods to model turbulence and various components of each magnetic field. It provides users with a simple framework to simulate photon-ALP oscillations and their resultant effects. This allows us to set up specific magnetic fields models as we require for our study cases, and assign parameters to these models as required for our work. We can additionally also specify ALP parameters which allow us to produce the final simulations we require for ALP searches. The specifics of how we utilize the framework in each case is described in the relevant chapters ahead.

Chapter 5

Constraining EBL Using M87

5.1 Overview

A preliminary analysis of the data set we constructed using the observations of Messier 87 during its reported flares revealed a distinct curvature in the spectrum of the source. Despite being a historically well observed source, such a curvature in the γ -ray spectrum of M87 has never been observed and/or reported. We proceeded to perform a thorough analysis over the spectrum, motivating this discovery in a statistically rigorous manner. We perform fits against the data, applying different spectral models and verifying the observed curvature through Likelihood analyses. In the process of publication, we combined our analysis with another ongoing project in the H.E.S.S. Collaboration. This project attempted to place constraints on the normalization of certain EBL models commonly used in the field of γ -ray astronomy. The project utilized data similar to ours, focused on observations of M87 during flaring/high states. This motivated a combined analysis, with mutual benefit regarding collaboration and publication related procedures.

The EBL as described in the Theoretical Foundation chapter is an extensive photon background present across our Universe. This constantly evolving background, composed largely of starlight and thermal emission from Cosmic dust contains within it the entire history of our Cosmos. The presence of these relic photons renders the Universe conditionally opaque to photons through photon-photon interactions, leading to pair production and the consequent attenuation of photon signals. While this effect is negligible at lower energies below the GeV range, as we approach the Very High Energy (VHE) threshold around 100s of GeV to TeV ranges and above, this attenuation effect become more significant and renders the Universe increasingly opaque to propagating photons. The opacity is also largely dependent on the distance of the source, expressed as Cosmological redshift. This functional “opacity” of the Universe is denoted by τ and is expressed as a function of energy and redshift (Dwek & Krennrich, 2013):

$$\tau_{\gamma\gamma}(E_\gamma, z) = \int_0^z dz' \frac{dl}{dz'} \int_{-1}^1 d\mu \frac{1-\mu}{2} \int_{\epsilon'_{th}}^\infty d\epsilon n_\epsilon(\epsilon, z') (1+z')^3 \sigma_{\gamma\gamma}(\beta', z') \quad (5.1)$$

where $n_\epsilon(\epsilon, z) \equiv dn(\epsilon, z)/d\epsilon$ is the specific comoving number density ($\text{cm}^{-3} \text{eV}^{-1}$) of background photons with energy ϵ at redshift z , and the $(1+z)^3$ term represents its conversion to a proper number density. The pair-production threshold energy is $\epsilon'_{th} = \frac{2(m_e c^2)^2}{E_\gamma(1-\mu)(1+z)}$, where the $(1+z)$ factor takes into account that the observed γ -ray photon had a higher energy at the redshift of the interaction. The parameter $\beta' = (1 - \epsilon'_{th}/\epsilon)^{1/2}$, and $dl/dz = c|dt/dz|$, where l is the proper distance.

where E is the observed gamma-ray energy, z is the redshift of the source, ϵ is the EBL photon energy, $n_\epsilon(\epsilon, x) \equiv dn_\epsilon(\epsilon, x)/d\epsilon$ is the specific co-moving number density, and $\sigma_{\gamma\gamma}$ is the cross-section for pair production.

We see here that the Universe increases in opacity as we observe sources at higher energies and redshifts. This leads to a visible cut-off in the spectra we observe for such sources. When concerning VHE γ -ray astronomy, such as is conducted using IACTs like H.E.S.S., it becomes crucial to model this attenuation and subsequent cut-off of our photon signals with reasonable accuracy. There are a few models of the EBL which are regularly utilized in the field to model extra-galactic sources, with constant improvements being made to said models. Through our combined analysis, we attempt to place upper limits on the normalization term for some frequently used EBL models: the Finke (Finke et al., 2022), Kneiske (Kneiske & Dole, 2010) and Dominguez (Dominguez et al., 2011) EBL models. We implement a custom model in *gammapy* which allows us to read in the model dependent values of EBL opacity from the *ebhtable* module and free the normalization term of the EBL model for fitting. This allows us to confidently place constraints/limits on the normalization of each chosen model.

Note: The combined analysis we performed towards this project was published as a H.E.S.S. Collaboration paper and is cited as (Aharonian et al., 2024) in the following Chapter(s). My individual contribution toward the publication was the original discovery of curvature in the source spectrum, along with the primary analysis performed for the project using the *gammapy* analysis pipeline. The remaining work required for publication was a combined effort led by Dr. Victor Barbosa Martins. The figures and tables presented in this Chapter directly reference our joint publication and have been cited accordingly throughout the text, acknowledging the important contributions of our colleagues and the H.E.S.S. Collaboration.

5.2 Data Selection

5.2.1 Messier 87

Messier 87 is a supergiant elliptical galaxy located in the Virgo constellation, at the center of the Virgo galaxy cluster, around 53.8 ± 0.3 Mly away from us at a redshift of $z \sim 0.0042$ (Mei et al., 2007). It was discovered in 1781 by Charles Messier, and was later included in the New General Catalogue with the name NGC 4486. It hosts a powerful AGN, powered by a $6.6 \pm 0.4 \times 10^9 M_\odot$ (Gebhardt et al., 2011) supermassive black hole at its core. It has been observed spewing powerful jets of highly energetic particles into the local Universe. M87 is one of the most massive galaxies in our Cosmic neighborhood, influencing the region in many significant ways. This source is also of particular historical and scientific significance when concerning the field of AGN, as explored in the Theoretical Foundations section of the Thesis. This is one of the most observed AGNs in history, being well observed over many years and across the EM spectrum, spanning energy ranges all the way from radio to VHE γ -rays.

Messier 87 has been observed in high or flaring states on numerous occasions since its first discovery. These flares have been detected primarily in γ -rays and sometimes with corresponding unusual activity in the X-ray band. The flares were detected by numerous instruments like H.E.S.S., MAGIC, VERITAS and Fermi-LAT. The very high energies reached during these flares, combined with the sheer amount of data available for the source makes it an ideal candidate for various studies which concern interactions with VHE γ -rays, including ALPs searches and EBL opacity measurements.

5.2.2 Observations

The primary goals of our study are to verify the presence of curvature in the spectrum of M87, and to exploit the highest energy photon statistics available from H.E.S.S. to probe EBL attenuation and the subsequent opacity of the Universe to VHE γ -rays. Since M87 is located relatively close to us at $z \sim 0.0042$, we require photon statistics at very high energies, on the order of TeVs, in order to effectively probe the ranges where EBL opacity is significant. Taking this into consideration, we focus our attention on observations surrounding the flares of M87 reported during H.E.S.S. observational campaigns. There have been 3 major flares reported by the H.E.S.S. Collaboration: the first in 2005 (Aharonian et al., 2006), the next in 2010 (Abramowski et al., 2012) and finally one in 2018 (Benkhali, Chakraborty, & Rieger, 2019). There have been other minor flares reported in the source, but our interest lies solely on the strongest flares and the highest energy statistics. We begin with a larger set of observations, between 2004 and 2022, limiting ourselves to observations where a minimum of 3 telescopes were triggered, with a mean zenith angle $< 57.7^\circ$. We gather data in the form of FITS files provided by H.E.S.S. for use with *gammapy*. We specifically use those which have had the proprietary standard zeta cut configuration applied to them for preliminary data reduction. We reduce these observations further to extract the spectra, limiting the energy to events above 300 GeV. We impose this limit in order to minimize systematic uncertainties in the Instrument Response Function (IRF). The upper energy limit is set at 31.6 TeV, being the limit until which each data point in the spectrum has a minimum of 2σ significance. The background estimation is performed using the reflected-region method (Berge, Funk, & Hinton, 2007) with a minimum angular separation of 0.15° to M87.

In order to strictly limit our data to the highest energy statistics, we consider only observations which comprise the 10th percentile (top 10 %) of the flux above 1 TeV as our high state observations. Fig. 5.1 shows the estimated flux of all observations we initially consider, and the highest 10% we select for our final analysis. Each point in the figure represents an estimated flux for the respective H.E.S.S. observation, and illustrates a light curve of M87 between 2004 and 2022, plotting the trend in flux variation over this time period. Based on a cumulative distribution function, a selection is made for the high states as denoted in red. These observations are included in the final analysis and amount to ~ 20.2 hrs of observational time.

We observe from Fig. 5.1 that our definition of a high state is a stringent one, as is evident when considering that the flare reported in 2008 is excluded under these conditions. This is deemed reasonable, considering that H.E.S.S. was unable to observe this flare at its peak intensity. With the final selection of observations made, we gather our final data set and proceed with our analysis and our exploration of the intrinsic and extended spectra of our source.

5.3 Detection of Curvature

5.3.1 Intrinsic Spectrum

With the goal of verifying curvature in the intrinsic spectrum of our source, we first establish constraints over our analysis to ensure we are truly studying the intrinsic spectrum of the source without other influences affecting our results. For similar sources, any curvature suggested by model fitting often tends to arise from the EBL attenuation component at higher energies. To strictly rule out this possibility, we limit the spectrum to energies where the gamma-ray opacity $\tau \leq 0.1$, which in this particular case is at ~ 10 TeV. We obtain this value by making calculations using the *ebltable* Python module (Meyer, 2024). This value is assumed as a general case by comparing the results from applying different EBL models. This energy limitation in

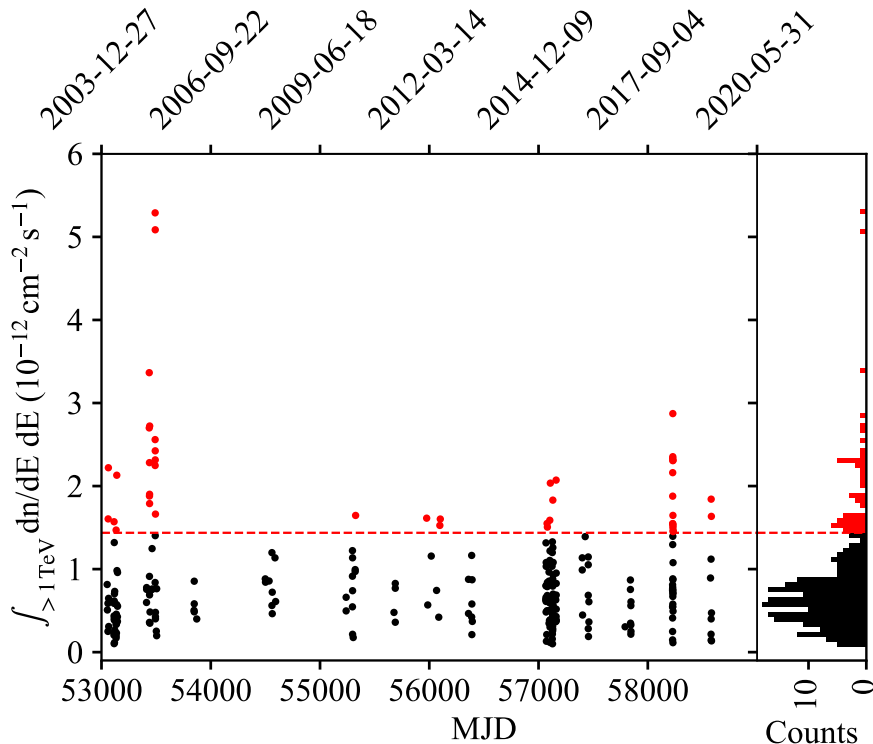


Figure 5.1: Caption A light curve of M87 showing observations extracted from 2004-2022. In red, we see the highest 10% of the flux, defining the high state for M87 as the 10th percentile of all observed fluxes. Extracted from (Aharonian et al., 2024).

our fit ensures that we do not fit the EBL attenuation component into our intrinsic model and introduce any bias. We fit the limited spectrum, now between 300 GeV - 10 TeV against a Power Law and a Log Parabola spectral model with the intention of testing for a significant preference for the curved model via Likelihood analysis.

In the case of the power law, we apply the standard model available with *gammapy*, described by the equation:

$$\phi(E) = \phi_0 \left(\frac{E}{E_0} \right)^{-\Gamma} \quad (5.2)$$

where $\phi(E)$ is the flux as a function of energy, ϕ_0 is the amplitude or normalization factor E is the energy, E_0 is the reference energy, and Γ is the spectral index.

For the log parabola model, we also implement the standard model available in *gammapy*, described with the equation:

$$\phi(E) = \phi_0 \left(\frac{E}{E_0} \right)^{-\alpha - \beta \log(E/E_0)} \quad (5.3)$$

where α is the spectral index, β is the curvature parameter and the other parameters are the same as in the power law model. When reporting our results we use α and Γ interchangeably

for the spectral index value.

The results of our fits have been reported in Table 5.1, along with the fit results of the next stage of the project. We see a clear preference for the curved Log Parabola model when comparing the $-2 \ln \mathcal{L}$ values. These values, also referred to as the C statistic represent the goodness of fit with a lower value indicating a higher Likelihood.

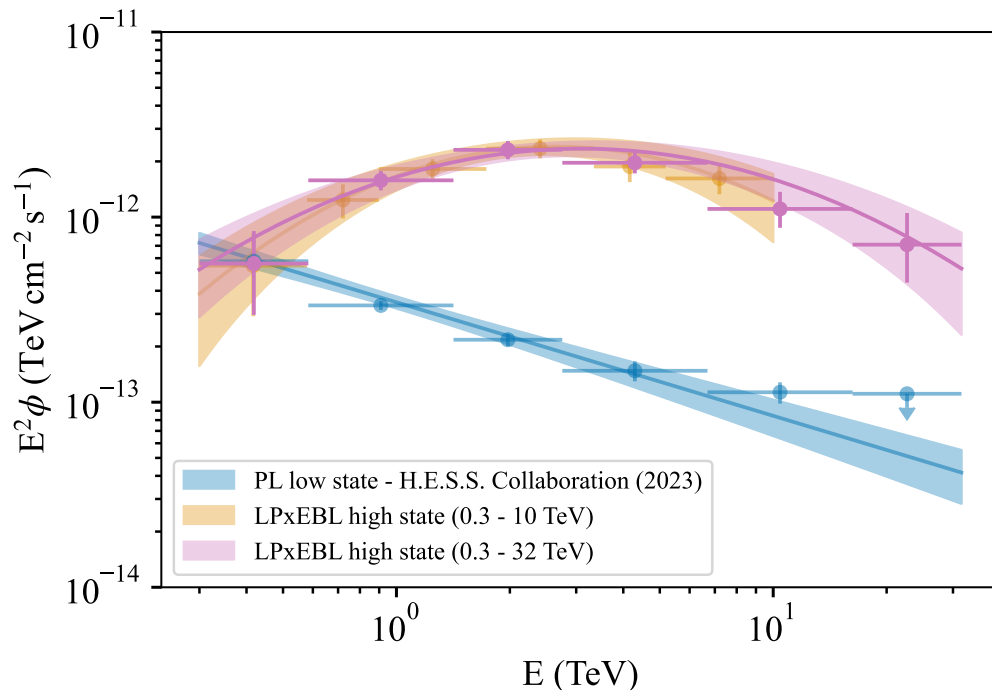


Figure 5.2: An illustration showing the flux points and spectral models in two cases. The curved models are fit against our data, while we see the flux points for M87 in the low state fit against a Power Law as published by H.E.S.S. in 2023. Extracted from (Aharonian et al., 2024).

Our fit results suggest a preference for the curved log parabola model over the power law. As illustrated in Fig. 5.2, we see a clear curvature in the spectrum when comparing the best fit models from our fits performed for both the limited and full range of energies. Also shown here is a comparison against the spectrum of M87 during low states as published by the H.E.S.S. Collaboration in 2023 (H. Collaboration et al., 2023), which exhibits a flatter spectrum and is better described by a Power Law.

5.4 EBL Constraints

5.4.1 EBL Models

The second part of this combined analysis aimed at placing constraints on the normalization value of some EBL models currently considered relevant in the field. After review and deliberation, we opted to use 3 EBL models, thus effectively covering the entire range of possible EBL spectra:

The Finke 2022 EBL model (Finke et al., 2022) is an improvement upon an earlier model (Finke, Razzaque, & Dermer, 2010) which was a widely utilized one in the field of astronomy

and astrophysics. It is compiled using a large amount of galaxy data, incorporating star formation rates, initial mass functions and luminosity density observations. It estimates the EBL spectral energy distribution for up to redshift $z \sim 6$. Its energy density falls close to the lower limits placed by galaxy counts.

The Kneiske model (Kneiske & Dole, 2010) was constructed with the intention of emulating the lower boundary of EBL flux. It gives us EBL estimates spanning a wide range of wavelengths, from ultraviolet through far-infrared. It also includes a redshift based evolution of the EBL. It is often used for lower bound estimates.

The Dominguez model (Dominguez et al., 2011) is made using a data driven approach, based on galaxy luminosity functions. It includes data spanning the ultraviolet to far-infrared wavelengths and provides EBL estimates up to redshift $z \sim 4$. We use the upper limits model from Dominguez which gives the upper end uncertainties outlined in the original publication.

5.4.2 Constraining α_{norm}

With the goal of placing constraints on our chosen EBL models, we introduce the respective EBL models to our data for fitting and further analysis. Our goal here is to place constraints specifically on the EBL normalization given by α_{norm} , rather than the overall normalization of our spectral model which is denoted by ϕ_0 . We do this by explicitly providing the EBL models to our fit models in the form of an exponential function raised to the opacity values τ provided explicitly from the Python module *ebhtable* (Meyer, 2024) as a function of energy and redshift. This allows us to then manually introduce a normalization term here to fit for. For example, if we introduce it alongside the power law model, it takes the form:

$$\phi(E) = \phi_0 \left(\frac{E}{E_0} \right)^{-\Gamma} e^{-\alpha_{norm}\tau(E,z)} \quad (5.4)$$

It should now be evident how introducing the normalization value α_{norm} explicitly enables us to perform fits and constrain our EBL models effectively. Additionally, for each fit we set the reference energy to the de-correlation energy obtained from a best fit performed with a simple power law model. Table 5.1 shows the results of our fits with the 3 EBL models, as well as the results of our intrinsic spectrum fits, within a limited energy range. We can effectively study the intrinsic spectral model by setting $\alpha_{norm} = 1$, and subsequently freeing the parameter to fit for EBL constraints. To place the constraints in a statistically motivated and rigorous manner, we perform an in-depth analysis of our fits.

5.4.3 Upper Limits

When attempting to place constraints on our EBL models, we choose to take an in-depth look at our fit results to make meaningful statements about our results. To this end, we construct statistical surfaces for our fits, as illustrated in Fig. 5.3. This aids us in exploring the trends in our best-fit as it converges along the parameter space created between our fit parameters α_{norm} and β . Each point along the space is color mapped to the square root of the C-statistic value for the given combination of parameters, indicating a confidence level.

Model	$-2\ln\mathcal{L}$	ϕ_0	Γ	β	Energy range
PL \times EBL <i>finke2022</i>	30.68	4.7 ± 0.3	1.81 ± 0.08	-	0.3 – 10 TeV
LP \times EBL <i>finke2022</i>	18.69	6.0 ± 0.5	1.76 ± 0.10	0.38 ± 0.13	0.3 – 10 TeV
PL \times EBL <i>kneiske</i>	36.23	3.7 ± 0.2	1.94 ± 0.06	-	0.3 – 32 TeV
LP \times EBL <i>kneiske</i>	16.86	4.8 ± 0.4	1.81 ± 0.08	0.29 ± 0.07	0.3 – 32 TeV
PL \times EBL <i>finke2022</i>	34.38	3.8 ± 0.2	1.92 ± 0.06	-	0.3 – 32 TeV
LP \times EBL <i>finke2022</i>	17.04	4.9 ± 0.4	1.80 ± 0.08	0.27 ± 0.08	0.3 – 32 TeV
PL \times EBL <i>dominguez-upper</i>	31.28	3.9 ± 0.2	1.88 ± 0.06	-	0.3 – 32 TeV
LP \times EBL <i>dominguez-upper</i>	18.20	4.9 ± 0.4	1.79 ± 0.08	0.25 ± 0.08	0.3 – 32 TeV

Table 5.1: Best fit results for the spectral VHE gamma-ray distribution of the high state of M87. We compare the PL and the respective LP best-fit spectral model for the reduced energy range and for the full energy range for each EBL model considered. The energy range is given in TeV and ϕ_0 is given in units of $10^{-12}\text{cm}^{-2}\text{s}^{-1}\text{TeV}^{-1}$.

Constructing such surfaces allow us to better understand how our fit converges to a certain best fit, and where our confidence intervals lie. This allows us to make more meaningful statements about our final results and how we arrive at them. From Fig. 5.3, we see how we can confidently place an upper limit for the EBL normalization for the Finke22 model at $\alpha_{norm} \leq 5.5$ at a 95% confidence level. Similarly we arrive at upper limits on the other two EBL models as well. We get $\alpha_{norm} \leq 8.7$ for the Kneiske model, and $\alpha_{norm} \leq 2.0$ for the Dominguez-upper model at a 95% confidence level. Upper limits of this nature help us gain a deeper understanding of the EBL and how it affects our observations of γ -ray sources such as M87. The conclusions we are able to make based on these results and their implications are discussed further in the Conclusions & Outlook section at the end of the Thesis along with a brief discussion on the implications of the detected intrinsic curvature in the spectrum of the source.

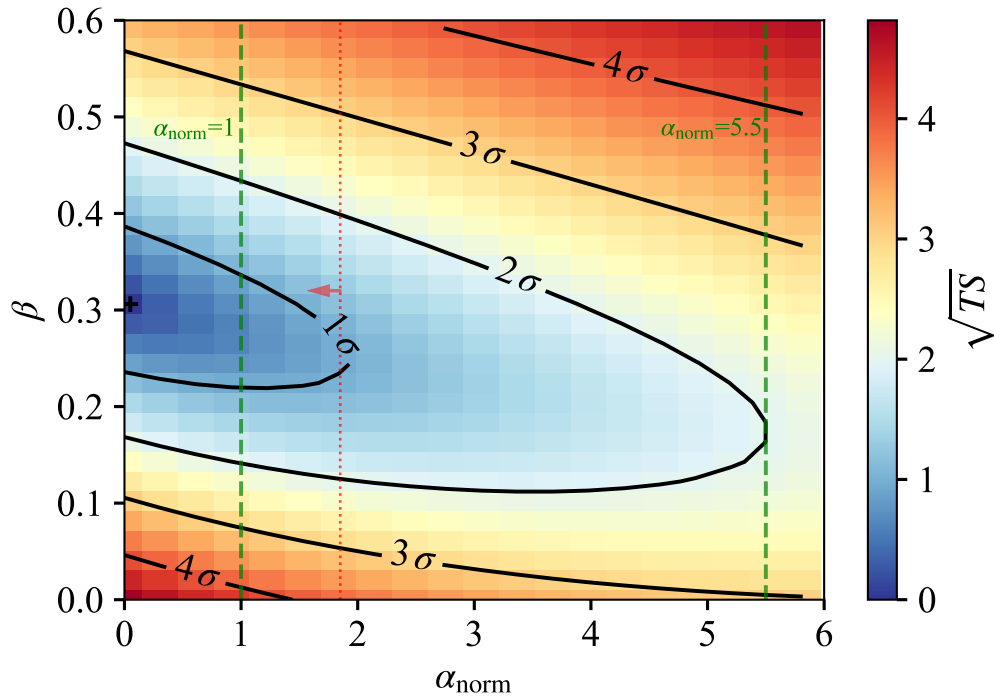


Figure 5.3: Statistical surface for the *finke22* model, mapping the parameter space between α_{norm} and β . It illustrates the change in std deviations as the color map. The lowest values show the convergence toward the best-fit. We see the contours for various levels of uncertainty (1, 2, 3... σ), giving us a better understanding of our best-fit.

The red dotted line shows the upper limit normalization value, above which it would contradict earlier upper limits (Biteau & Williams, 2015) placed on the *finke22* model.

Extracted from (Aharonian et al., 2024).

Chapter 6

ALP Searches in Virgo Using M87

6.1 Overview

The central AGN hosted by Messier 87 emits energy in the form of various particles and radiation spanning a vast range of energies along the EM spectrum. During states of high activity, it emits heavy amounts of radiation, reaching the highest energies and leading to a visible change in its activity across the EM spectrum. This change is particularly noticeable in the γ -ray energy ranges as observed by our instruments on Earth. As these high energy photons arrive at the Earth, they interact with the upper atmosphere causing cascades of energetic particles to shower down on us. These showers are ultimately detected by instruments like H.E.S.S. and other IACTs which provide us the opportunity for research. In order to accurately model and reconstruct the original source of emission, we attempt to predict and account for all known effects which may alter the state of the signal photons as they traverse the local Universe to arrive at the Earth. One well known and accepted phenomenon which alters the course of our high energy messenger photons is attenuation caused by EBL photons. This concept was already explored in the previous Chapter where we constrained the EBL normalization for various models existing in the field.

Another predicted effect which might alter the course of our high-energy messengers is photon-ALP oscillations induced by astrophysical magnetic fields. On the journey these highly energetic photons undertake from their creation at their source until their annihilation in the Earth's atmosphere, they traverse various astrophysical magnetic fields which are expected to induce photon-ALP mixing by the Primakoff effect (Primakoff, 1951). The Primakoff effect in turn is predicted to result in photon-ALP oscillations, whereby the particle periodically oscillates between photon and ALP eigenstates as it propagates through an external magnetic field. This implies an observationally probabilistic chance for the particle to exit the magnetic field in the ALP eigenstate, rendering them invisible to our detectors. By simulating the combined effects of all known magnetic fields along the line of propagation, we can attempt to predict and search for signatures of this so called "photon extinction" effect. In constructing our models, we primarily consider the Virgo cluster and the Milkyway magnetic fields as contributing to this effect. The equations of motion describing the propagation of the photon/ALP superposition through these magnetic fields help us calculate a probability for photons to survive their journey, implying that they arrive at our detectors in the photon eigenstate. We can thus calculate the survival probabilities of our signal photons and simulate the expected spectrum for our source while accounting for various magnetic fields, varied ALP parameters and the resultant photon extinction.

The first step in this undertaking is to set up precise models for the magnetic fields involved in our simulations. This is facilitated using the *gammaALPs* open source framework (Meyer et

al., 2021) which allows us to construct models and calculate the photon-ALP equations of motion. We utilize the pre-existing Jansson and Farrar model (JF12) (Jansson & Farrar, 2012) for the Milkyway magnetic field and attempt to improve the model for the Virgo cluster magnetic field. To account for the turbulent nature of the magnetic field of the Virgo cluster, we choose to apply a Gaussian turbulence model as opposed to a randomized cell-by-cell model as utilized in previous works of this nature (M. D. Marsh et al., 2017). We model the magnetic field in two distinct regions: an inner and an outer region. We describe the magnetic field as a function of the central magnetic field, varying radially with a change in electron density with a fall-off factor. We can obtain electron density measurements from the CHANDRA and ROSAT X-ray observatories, interpolating over the data for a function describing the electron distribution. To make a precise estimation of the central magnetic field, we begin by calculating Faraday Rotation Measures along two lines of sight within the cluster magnetic field: one aimed at M87 which resides at the center of the cluster, and one aimed at M84 situated in the outer region of the cluster. We run simulations of the magnetic field with varying values for the central magnetic field and the falloff term, using these results to make comparisons against reported values for the RM values for both M87 and M84. We constrain the values for the central magnetic field and the fall-off factor this way.

Using the values we obtain for the central magnetic field and the fall-off factor, we now construct the models for our ALP searches in *gammaALPs*. To accommodate for the chaotic nature of our turbulent magnetic fields, we run ~ 1000 pseudo-randomized simulations for each set of ALP parameters in our chosen parameter space. We obtain photon survival probabilities for each case and convert these into spectral models for our source. We then fit our spectrum against every single one of these simulated models and congregate the fit results. We treat the fit results for each separate combination of parameters as a non-Gaussian distribution and use the 5th percentile value of each distribution to represent the respective “pixel” in the parameter space for our final analysis. We take these results from each pixel and conduct a Likelihood ratio test against a simple log parabola with EBL spectral model, in order to check for any significant preference for either the ALP or no-ALP case.

Note: The work undertaken in this project has been presented and published as Proceedings of Science at the 7th Heidelberg International Symposium on High-Energy Gamma-Ray Astronomy 2022 (Cecil & Meyer, 2023) and the 38th International Cosmic Ray Conference 2023 (Cecil, Barbosa, Lypova, & Meyer, 2023). The following report resembles our publications and utilizes similar or identical plots as it represents the same work product. Appropriate citations have been made where necessary to avoid confusion.

6.2 Modeling Virgo

6.2.1 Virgo Cluster

The Virgo cluster is one of the most well studied structures in our Cosmic neighborhood. It is located between the Virgo and Coma Berenices constellations in our night sky. This cluster is at the heart of the Virgo super cluster and is one of the largest galaxy clusters in the Earth’s proximity. It spans ~ 4.5 Mpc and is located ~ 16.5 Mpc away (Mei et al., 2007). It has an estimated mass of $6.3 \pm 0.9 \times 10^{14} M_{\odot}$ and houses an estimated 1500 galaxies (Kashibadze, Karachentsev, & Karachentseva, 2020), including many notable Messier galaxies such as M87, M49, M84, M86, M91 and M100.

This galaxy cluster has been the subject of many observations and studies, helping us gain better insight into topics such as galaxy interactions, galaxy evolution & large-scale Cosmic

structure formation. This particular cluster also provides us with opportunities to study dark matter distribution, primarily with respect to structure formation and Cosmic evolution. The immense mass of the cluster influences the dynamics of nearby galaxies, including our own Milkyway through a phenomenon termed Virgocentric flow (Bothun, 1998). The intra-cluster medium is filled with a hot plasma, making it optimal for X-ray astronomy (Lea, Mushotzky, & Holt, 1982). The extended electron density profile of Virgo occupies nearly the entire volume of the cluster, with previous studies suggesting the presence of a relatively strong magnetic field by virtue of said electrons (Owen, Eilek, & Keel, 1990; Algaba, Asada, & Nakamura, 2016). The strong magnetic field and expansive dimensions of the cluster lend itself to us as an ideal laboratory to conduct axion and ALP searches. While its proximity might prove a limiting factor in terms of redshift, we expect it to compensate greatly with available data.

6.2.2 B-Field Model

In the context of ALP searches, one of the most significant features of our model is the magnetic field. The magnetic field of the Virgo cluster is quite extensive, spanning almost the entirety of the ~ 4.5 Mpc wide cluster. Previous studies indicate the presence of a strong central magnetic field of $\sim 35 - 40 \mu\text{G}$ (Owen et al., 1990; Algaba et al., 2016). In our approach, we opt to model the cluster magnetic field in two distinct regions: an inner and outer region. The expectation here is that the two regions behave in significantly different ways and display different magnetic field profiles, thus motivating a clear distinction in our model.

Many systems we encounter in nature are inherently chaotic, making them difficult to model and predict in a truly deterministic manner. The magnetic field of the Virgo cluster is no exception, being inherently turbulent in nature. This renders the magnetic field quite difficult to model in a purely analytical manner, leading us to utilize a more numerical and statistical approach when predicting the outcomes of our model(s). While the general methodology we use follows similar steps to that of a previous study (M. D. Marsh et al., 2017), the primary difference in our approach lies in the model we choose to account for the turbulence in the magnetic field. The approaches taken previously involve utilizing a cell-like morphology, with the field strength magnitude remaining the same, but the orientation changing randomly with each cell. They take the coherence length to be on the order of the size of the galaxy cluster itself at ~ 10 kpc.

We opt for a Gaussian turbulence model which is divergence free, homogeneous and isotropic with zero mean and a variance B^2 in a similar manner to another previous study (Murgia et al., 2004). We make the assumption that the power spectrum of the turbulence follows a power law with wave numbers $M(k) \propto k^q$ between $k_L \leq k \leq k_H$ and zero otherwise (Meyer, Montanino, & Conrad, 2014). As discussed above, we choose to model the field in two distinct regions: an inner and outer region. We model both to exhibit different magnetic field profiles with respect to the change in the matter distribution profile. We take $k = -2.9$, $k_L = 0.42$, $k_H = 6800$ and $k = -2.5$, $k_L = 0.42$ and $k_H = 12$ for the inner and outer regions, respectively. In the case of region 1, we select these values in order to match the coherence length of 0.2 kpc found in another study (Guidetti, 2011). For region 2 we choose values from (Vacca et al., 2012) following along with (M. D. Marsh et al., 2017).

The expectation in our model regarding the variation of the magnetic field is quantified such that \vec{B}_i varies as a function of the central magnetic field and the electron density, varying radially from the core. The specific equation is:

$$(\vec{B})_i = B_0 \left(\frac{n_e(r)}{n_e(0)} \right)^\eta \quad (6.1)$$

where B_0 is the central magnetic field, $n_e(r)$ represents the radially varying electron density and η (also given by α in some publications) is the fall-off factor.

In order to construct and constrain the models for our study, we utilize the open source python library *gammaALPs* (Meyer et al., 2021) which includes built-in options for modeling different types of magnetic fields, and to generate pseudo randomly seeded realizations of the selected turbulent fields.

6.2.3 Constraining B_0

Before we begin to simulate for ALP effects from our turbulent magnetic field, we need to obtain realistic values for B_0 , $n_e(r)$ and η as seen in eq. 6.1. In order to achieve this, we begin by gathering electron density measurements from CHANDRA and ROSAT observations (Nulsen & Böhringer, 1995; Russell, Fabian, McNamara, & Broderick, 2015; Urban, Werner, Simionescu, Allen, & Böhringer, 2011). We perform a best fit over the obtained distribution for n_e with the electron density chosen to be flat at low radii as illustrated in Fig. 6.1.

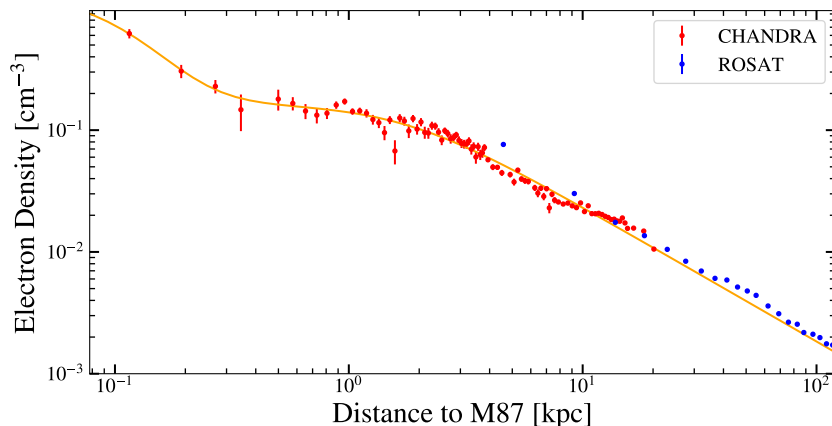


Figure 6.1: Plot showing the electron density distribution in Virgo from the utilized X-ray data, with the best fit model obtained for the points. (Cecil & Meyer, 2023)

In order to constrain B_0 and η , we follow similar steps to (M. D. Marsh et al., 2017) and calculate the Faraday Rotation Measure values of radio photons along two lines of sight. Faraday Rotation is a magneto-optical phenomenon where linearly polarized light passing through a magnetic field parallel to the direction of light propagation decomposes into left and right-hand circularly polarized light. This occurs due to a birefringence introduced by the magnetic field in the medium. Here, we can exploit this phenomenon to constrain the magnetic field of the Virgo cluster.

We do this by making calculations for the RM values along two lines-of-sight (l.o.s.). The first l.o.s. we take is toward our candidate source M87 lying at the center and in the inner region 1, while the second is toward M84 which lies in the outer region 2. These values were calculated in (Guidetti, 2011) using VLA observations of the Virgo cluster and we follow similar

methods. We calculate the Rotation Measure (RM) as a l.o.s. integral over the electron density and magnetic field component which is parallel to the l.o.s.:

$$\text{RM} = \frac{e^3}{2\pi m_e^2} \int_{l.o.s.} n_e(l) \vec{B}(l) \cdot d\vec{l} \quad (6.2)$$

We calculate the RM values along both l.o.s. to M87 and M84 setting their distances at 16.520 Mpc and 16.830 Mpc respectively (Tully, Courtois, & Sorce, 2016). This also gives us a distance of 535.39 kpc between the two sources. We calculate the RM values along both l.o.s. and produce 2000 randomly realized B-fields for a set of possible combinations of B_0 and η . We then obtain a distribution for each set of these values as a spread of calculated RM values. We expect the distribution to be centered around, and peaked at zero. This is an expected behavior since the orientation of the field is pseudo-randomized. We calculate the standard deviation σ for each of these histograms, respective to each combination of B_0 and η values. These values allow us to obtain a measure of the dependence $\sigma(\text{RM})$ on each of the two parameters when keeping the other fixed. All this has been illustrated in Fig. 6.2 as an example. Shown in the figure are just 3 histograms representing 3 combinations of B_0 and η .

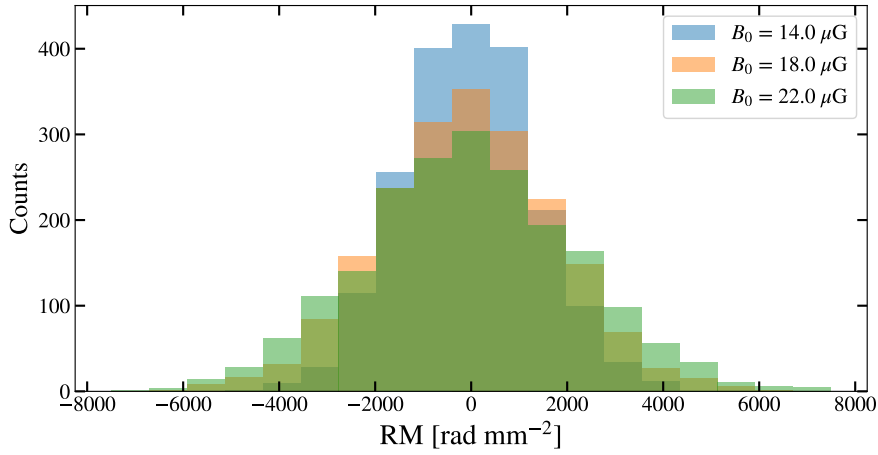
As illustrated in Fig. 6.2 we plot contours along our parameter space for constant $\sigma(\text{RM})$ between B_0 and η . This allows us to constrain the optimal values for these parameters. We now compare and restrict the values of RM and η within known or realistic limits from past studies. We expect the RM values along the M87 l.o.s. to be between 1000 - 2000 rad mm⁻², while that for the M84 l.o.s. to generally be quite small (M. D. Marsh et al., 2017; Guidetti, 2011). Additionally, we expect $\eta \sim 0.5$ by equi-partition, where we expect the energy density in the magnetic field to scale with the energy density in the intra-cluster plasma (M. D. Marsh et al., 2017). We consider the points where our contour lines intersect to represent realistic cases, and finally arrive at a value of $B_0 = 34.2 \mu\text{G}$ and $\eta = 0.42$ as shown the point marked in Fig. 6.3.

6.3 Searching For ALPs

6.3.1 Modeling Spectra

The predicted effects emerging from photon-ALP mixing has many implications in the field of astrophysics as is described by (Raffelt & Stodolsky, 1988) among others. We focus here on the appearance of so-called “wiggles” in the spectra of VHE energy γ -ray sources caused by the extinction of photons through the process of photon-ALP oscillations in the presence of astrophysical magnetic fields. Theory predicts that the incoming photons will undergo photon-ALP oscillations as they traverse various magnetic fields along their path. The fraction of these particles which arrive at our detectors while in the ALP state will go undetected. Evidence of these lost photons are predicted to appear as “wiggles” in the spectrum of our source. We can compute the equations of motion for ALPs as described in the Theoretical Foundations chapter and apply a statistical analysis to predict the possible wiggling effects on the spectra.

We can construct detailed models to predict the effects of the photon-ALP oscillations using the open source Python framework *gammaALPs* (Meyer et al., 2021). The software package allows us to easily incorporate various astrophysical magnetic fields and specify ALP parameters like mass and coupling to the EM field. While constructing these models, we attempt to account for the inherent turbulent nature of the magnetic fields we expect along the line of propagation



(a) Distribution of RM values

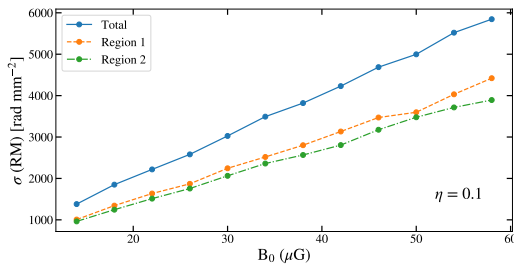
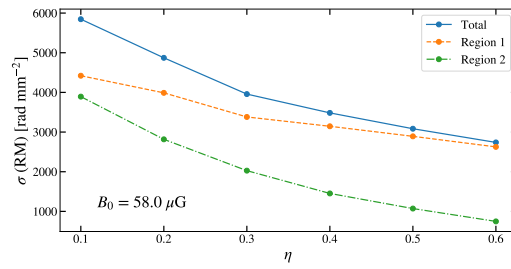
(b) RM vs B_0 (c) RM vs η

Figure 6.2: Plots illustrating the results of the RM calculations along the M87 l.o.s. (a) A histogram showing the RM distributions of 3 combinations of B_0 and η values. From these histograms we calculate $\sigma(\text{RM})$ values. An example for the dependence of $\sigma(\text{RM})$ on B_0 for a fixed η value is shown in panel (b) and vice versa in panel (c). (Cecil & Meyer, 2023)

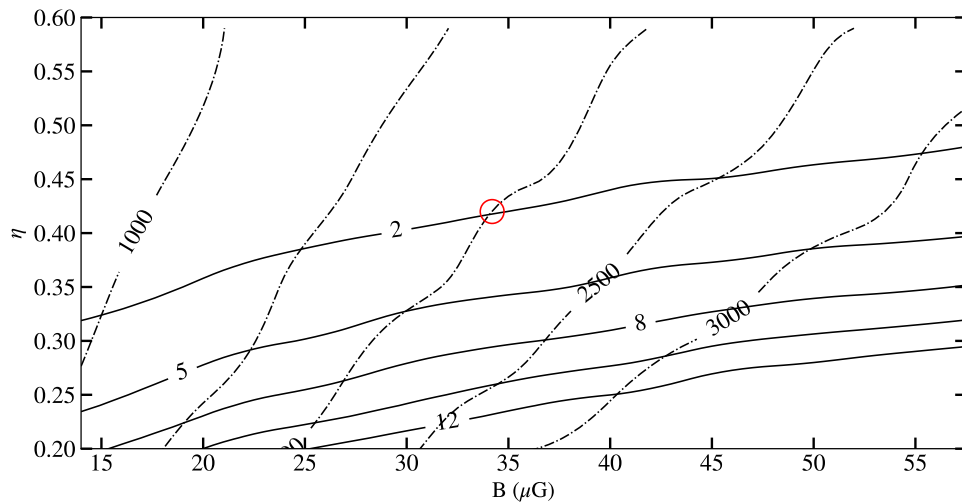


Figure 6.3: The possible $\sigma(\text{RM})$ in rad mm^{-2} values of M87 (dashed) and M84 (solid) plotted in a space of B_0 vs η . Circled here in red is the chosen intersection point of the contour lines at $B_0 = 34.2 \mu\text{G}$ and $\eta = 0.42$. (Cecil & Meyer, 2023)

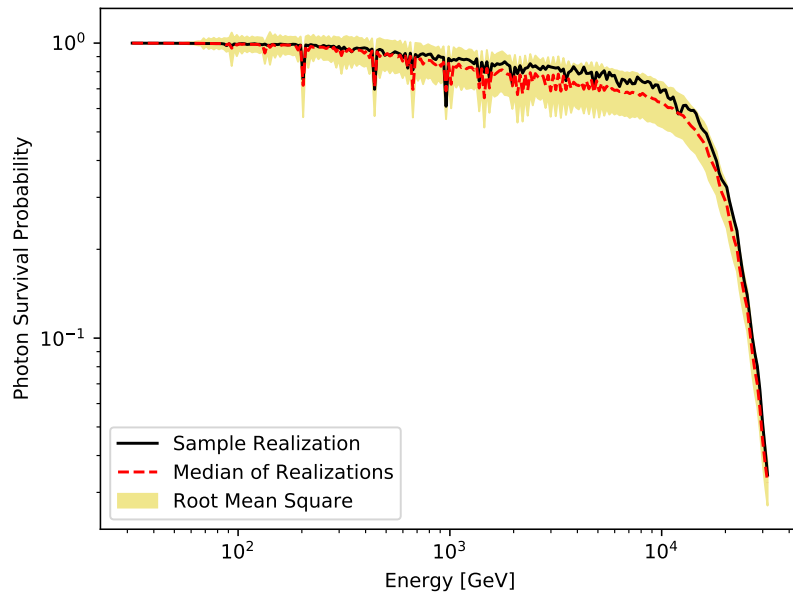


Figure 6.4: One realization of photon survival probability plotted against the rms values and the median of all rms value over all realizations ($m_{ALP} = 100$ neV; $g_{a\gamma} = 10^{-11}$ GeV $^{-1}$). (Cecil & Meyer, 2023)

of our particles as described earlier. To effectively account for the inherent randomness of the system, we decided to simulate 1000 pseudo-randomized realizations of the entire journey our candidate particles would undertake and to treat the results in a statistical manner henceforth. Simulating these realizations of photon-ALP oscillation effects in *gammaALPs* produces photon survival probabilities along our simulated energy range. An example of such a distribution of photon survival probabilities is shown in Fig. 6.4. We can easily convert this into an expected spectral model by combining it with the basic spectral model for M87, which we select to be a log parabola with EBL attenuation following the Dominguez model (Dominguez et al., 2011), as motivated in our previous study.

Our search for ALPs here is specifically aimed at ultralight ALPs at the neV mass ranges. We select a range in the parameter space between $m_{ALP} = 3.162 - 316.2$ neV & $g_{a\gamma\gamma} = 4.6 \times 10^{-12} - 10^{-10}$ GeV $^{-1}$ and construct a coarse grid of 5×5 pixels in log scale to probe the parameter space. The mid point of each pixel represent a specific combination of mass and coupling values. We run 1000 simulations per pixel, resulting in a total of 25,000 models to fit against the spectrum of M87.

6.3.2 Fitting & Interpretation

Having successfully performed our simulations and constructed ~ 1000 model spectra per pixel in our parameter space, we attempt to handle this bulk of information in a sensible and statistically valid manner. We begin by fitting every one of our 25,000 models against the spectrum. The 1000 fit results per pixel are collected and organized into 25 individual distributions of C-statistic ($-2 \ln \mathcal{L}$) values, with one corresponding distribution per pixel. We consider each distribution to be reasonably represented by the 5th percentile value of the total distribution, and thus representing the Likelihood of the ALPs case for the respective mass and coupling values. We consider this Likelihood against the no-ALPs case, which is represented by a log parabola with EBL attenuation as described by the Dominguez model (Dominguez et al., 2011).

We perform a Log Likelihood ratio test to check for a preference for either case for each pixel in our parameter space. The results for this are illustrated in Fig. 6.6.

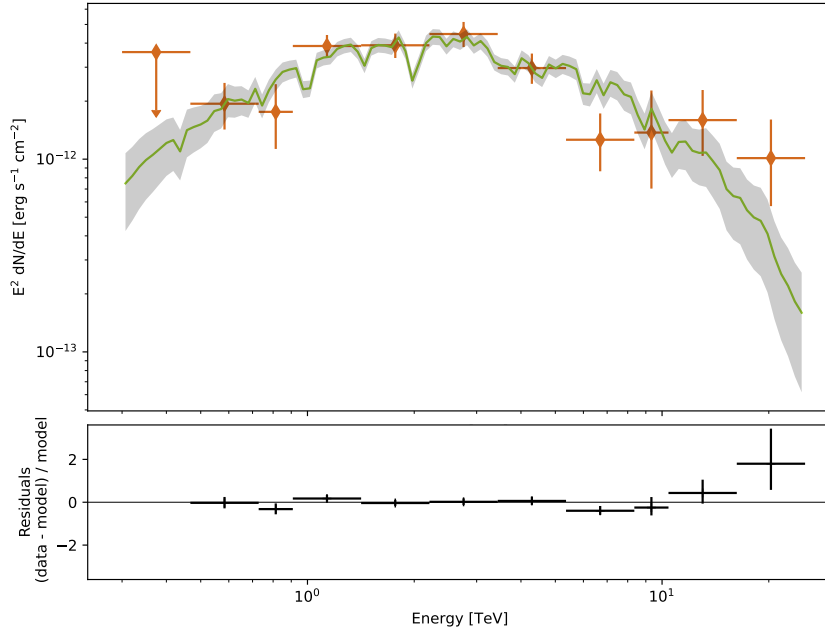
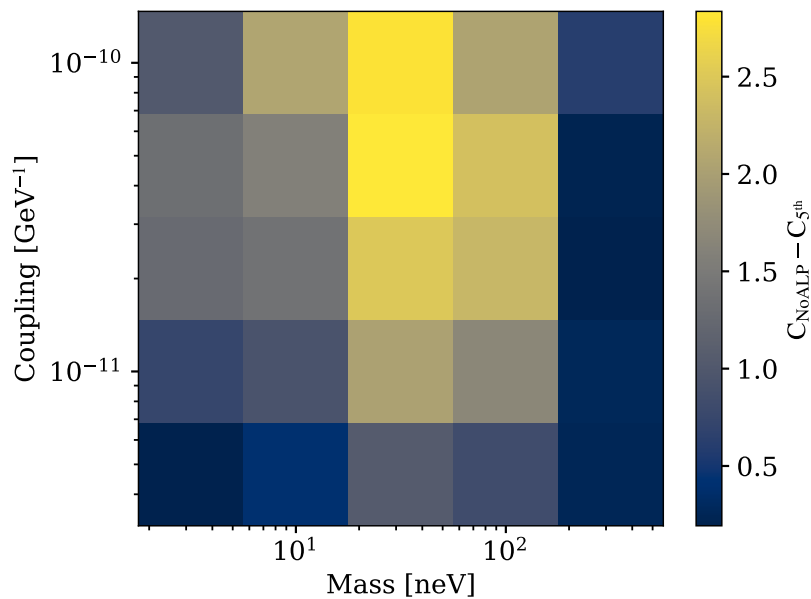
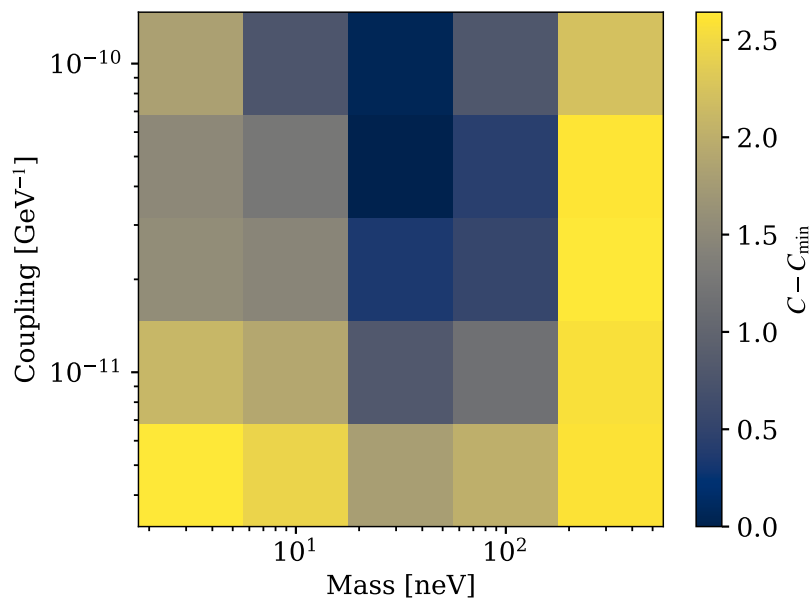


Figure 6.5: A sample plot showing one pseudo-randomly simulated model with ALP wiggles, shown as fitted against the spectrum of M87. This model is specifically for $m_{ALP} = 100$ neV & $g_{a\gamma\gamma} = 10^{-11}$ GeV $^{-1}$ and illustrates only the 5th percentile pseudo-random realization of the 1000 we performed for the same parameters.

The results of our Log Likelihood ratio test prove largely inconclusive. We see at best a preference for our ALPs model at $< 2\sigma$. In contrast, we also do not see any strong preference for the no-ALP case either, rendering it impossible to rule out the presence of ALPs with statistical confidence as well. This implies an inability of our fitting methodology to separate the photon-ALP “wiggles” from statistical fluctuations and noise. This may be due to the lack of enough data or instrumental limitations. We discuss the implications of our results, the limitations we face, and possible future outlook for similar work in the Conclusions & Outlook Chapter.



(a)



(b)

Figure 6.6: Illustrated here are the final results of our ALPs search, showing our coarsely binned parameter space of 5×5 pixels. The color map shows us the results of our Log Likelihood ratio test, indicating a preference for either model. The color map in Fig (a) shows us the distribution of the results of our ratio test, while Fig (b) shows the deviation of the other values from the highest Likelihood value in our parameter space.

Chapter 7

Upturn Searches for ALPs

7.1 Overview

In the journey a VHE γ -ray photon makes from its extra-galactic source toward the Earth, it encounters an extensive background of photons in the form of the EBL. Higher energy γ -rays in the high GeV to TeV ranges readily interact with these background photons leading to pair-production and attenuation. The functional opacity of the Universe to γ -rays, as described by Eq. ??, leads to a cut-off in our photon signals. This effect becomes increasingly significant as we attempt to observe sources at higher energies and redshifts. Being able to model EBL attenuation of γ -rays is thus not only a crucial component in γ -ray astronomy, but also a limiting factor for our observational capability in general. Various EBL models have been developed and are being applied in the field at the time, with a growing importance for these models and their accuracy. We placed upper limits on 3 such models in our earlier work as described earlier in the thesis. Despite the concept of the EBL being widely accepted, and the hard cut-off via the EBL being considered a norm in the field, we have growing indications of anomalous behaviors in our observations. Some studies suggest the possibility of γ -rays having somehow evaded this attenuation, appearing in our detectors while our models do not predict their arrival. These studies include the anomalous detection by LHAASO which reports the apparent detection of an unexpected TeV event from GRB 221009A, and a few PeV detection reports from the Cygnus region (L. Collaboration et al., 2023; Cao, 2023). Other seemingly improbable observations by other IACTs and Fermi LAT contribute toward the mystery of this anomalous transparency of the Universe to γ -rays.

While there are many explanations and models being offered to explain the presence of these anomalous photons, we make the case here for these being a secondary effect of photon-ALP oscillations caused by mixing of the photon and ALP states due to the presence of astrophysical magnetic fields. This secondary phenomenon is expected to appear as a consequence of the Primakoff effect (Primakoff, 1951) as discussed in the Theoretical Foundation chapter. Thus we see how by the introduction of axions and ALPs into our Cosmological model, we open ourselves to the various secondary effects that arise from photon-ALP interactions which in turn might offer us explanations for certain anomalous observations. The anomalous photon events can be modeled as a consequence of a significant fraction of the particle's propagation being made in an ALP eigenstate state, only to oscillate back into the photon eigenstate locally and appearing in our detectors. This could be simplistically compared to a “shining-light-through-a-wall” experiment, but on Cosmic scales with naturally occurring systems. With many known astrophysical magnetic fields present across the Universe, photon-ALP oscillations of this nature are largely feasible. The relative weakness of the fields compared to artificially generated ones are easily compensated by the sheer scale of these fields. In a Universe with ALPs, we might be able to provide reasonable models to explain the anomalous VHE photon events reported by numerous

detectors at this point of time.

We use this possible secondary effect from photon-ALP oscillations to attempt to search for these particles and/or constrain their properties along their mass-coupling parameter space. By modeling such anomalous VHE γ -ray photons as upturns in the spectra of VHE γ -ray sources, we are able not only to search for more anomalous events in the regions of spectra beyond the EBL cutoff, but also to fit our ALP model(s) against these spectra to test for statistical preference. We select a number of blazars observed by H.E.S.S. and reported to have been in high/flaring states throughout the years of their observation. Our primary goal here being to gain as much possible statistics at the highest energies, where the Universe would lend itself to the highest relative opacity values. We select our candidate blazars, consolidate all available data surrounding flaring periods, and attempt to filter and segment the data if/when required. After the careful construction of an elaborate and partially segmented data set, we search for upturning spectra by statistical fitting. We further attempt to relate these upturns to ALP induced transparency by preparing and comparing ALPs based models which we build using the *gammaALPs* open source framework (Meyer et al., 2021).

7.2 Data Selection

7.2.1 Sources

To pursue an ALP search using spectral upturns, we require large amounts of photon statistics in the regions where our Universe lends itself to being functionally opaque. This requires observations at very high energies and/or redshifts. We selected a set of blazars to build our data set, hoping to exploit these VHE sources, particularly during “high” states as seen with Messier 87 in our earlier work. Due to their jets being directed along our l.o.s. we expect to gain the highest energy statistics from these sources. While our focus remains largely on the statistics in the optically thick regions, the importance of data available in the lower ends cannot be undermined. Having this data enables us to model intrinsic spectra and motivate any upturning against the intrinsic model. Thus, we focus not only on data available during flare but also surrounding these flares. We begin with a list of blazars with published reports of flaring detected during H.E.S.S. observational campaigns and consolidate all data available during and surrounding the reported flares. Table 7.1 provides a list of all 13 blazars which were selected for creating our data set, their Equatorial coordinates and their Cosmological redshifts. This information was primarily gleaned from NASA/IPAC Extragalactic Database. With our sources shortlisted and their reported flares noted, we can proceed to the next step of our analysis: obtaining and organizing all available data that fit our requirements.

Note: In the context of our work, we are not concerned with studying the behavior of blazars themselves and do not attempt to pursue any in-depth exploration of the individual sources. We simply treat each source as a powerful γ -ray generator which we can exploit to search for ALP signatures. While many of these sources certainly hold the potential for in-depth research, a study of this nature is beyond the scope of our work. The dataset we construct would generally prove useful for studies of this nature, as discussed more in the Conclusions & Outlook section at the end.

Source Name	Coordinates [RA, DEC]	Redshift
1ES 0229+200	38.2025, 20.288	0.1396
1ES 0347-121	57.3467, -11.9908	0.1880
1ES 0414+009	64.2183, 1.0900	0.2870
1ES 1101-232	165.9071, -23.4919	0.1860
1ES 1312-423	198.7642, -42.6139	0.1050
1RXS J101015.9-311909	152.5662, -31.3193	0.1420
H2356-309	359.7825, -30.6275	0.1650
Markarian 421	166.1138, 38.2088	0.0300
Markarian 501	253.4880, 39.7530	0.0340
PG 1553+113	238.9293, 11.1901	0.4339
PKS 0447-439	72.3529, -43.8358	0.3430
PKS 1510-089	228.2106, -9.1000	0.3610
PKS 2155-304	329.7167, -30.2256	0.1170

Table 7.1: Table showing the candidate blazars, their Equatorial coordinates and Cosmological redshifts as utilized for our work.

7.2.2 Observations

With the goal of gathering all available data surrounding the flares of these sources, we begin by generating run-lists using the proprietary HAP toolkit. We limit our run-list to observations where a minimum of 3 telescopes were triggered. We consider observations both with and without CT5 to maximize available statistics. We merge the run-lists for each source, bridging temporal gaps and begin to locate and reduce the data available as FITS files for *gammapy*. As mentioned before, the final run-lists in *gammapy* often vary due to technical errors in the conversion to *gammapy* usable formats. We utilize data which has been cut using the standard “ImPACT” cut configuration, performed by collaboration members before being made available for analysis with *gammapy*. We further reduce each observation to be limited within a cone of radius $\leq 0.0707^\circ$ around the source coordinates. The background is estimated by the reflected-region method (Berge et al., 2007) and the data is reduced for spectral analysis. Table 7.2 shows each source, the number of observation hours that were available to us, and the detection significance of each source with the available observations.

With the initial data sets prepared for each of the respective sources, we begin to take a deeper look at each source. We begin by generating light curves for each source in order to better understand their variability over time, and verify reported flaring. Each light curve is generated using methods made available in *gammapy*, with some minor modifications made as necessary. Each light curve is constructed by utilizing average flux values, which are obtained by fitting the source spectra against simple Power Law models. We generate individual light curves binned by season and by night for each source, and make a simple preliminary analysis of their behavior using these preliminary results. Needless to say, simple visual analysis is insufficient for any kind of real inference, and merely provides us with a starting point in order to further direct our searches. We note which sources appear to show high variability and make initial considerations for which sources might require further segmentation of data. Once we generate light curves for each source, we utilize these data points to do a proper statistical analysis and begin our first steps toward determining the need for segmentation if/where statistically motivated.

Source Name	Available Data [hrs]	Det.Significance [σ]
1ES 0229+200	170.33	15.94
1ES 0347-121	59.23	15.26
1ES 0414+009	82.22	6.19
1ES 1101-232	105.40	22.32
1ES 1312-423	115.88	6.45
1RXS J101015.9-311909	56.21	7.27
H2356-309	173.88	24.61
Markarian 421	20.28	41.98
Markarian 501	5.59	31.91
PG 1553+113	78.54	24.56
PKS 0447-439	18.48	9.66
PKS 1510-089	28.25	7.33
PKS 2155-304	68.09	332.15

Table 7.2: Table showing the candidate blazars, the hrs of observations utilized from H.E.S.S., and the detection significance with the available data.

7.2.3 Bayesian Blocks

Having obtained detailed light curves for each of our sources, we now attempt to make meaningful, statistically motivated choices on if/how each data set requires segmentation. The initial criteria we employ for segmentation concerns the variability in average flux of the source over time. Or in simpler terms, we segment the data sets based on any significant variation in the light curve of the source. In order to identify any periods with significant variation in average flux, we utilize a Bayesian statistics methodology. Specifically, we pass our night-by-night light curves for each source through the Bayesian blocking algorithm made available through *astropy*v6.1¹. Each light curve is passed through the algorithm, which then determines segments or “blocks” of the data set which have significantly different flux values. Such segmentation is made only if it proves statistically significant, otherwise the algorithm produces a single final block suggesting that no segmentation is required based on flux variability. As would be expected, the sources display all manner of different emissive behavior. A significant number of sources produced no individual Bayesian blocks, and were thus deemed as requiring no segmentation in their data sets. Some sources show slight variability in the light curve with a few blocks produced, and a few show greater and more complex variability and indicate a need for further investigation.

While these Bayesian blocks provide us with a good initial segmentation, we do not take this as a final means of segmentation for our data. We leave the sources which did not show significant variability as such, but for the sources which did produce two or more Bayesian blocks, we begin a more in-depth analysis to determine what amount of segmentation the data set would logically require to minimize biases. This requires studying their individual spectra in each of the Bayesian blocks generated by the algorithm. Understanding variation in the spectra over these blocks, if any, would provide a better indicator for significantly different behavior in the sources, and would motivate further necessity for segmentation.

¹<http://www.astropy.org>

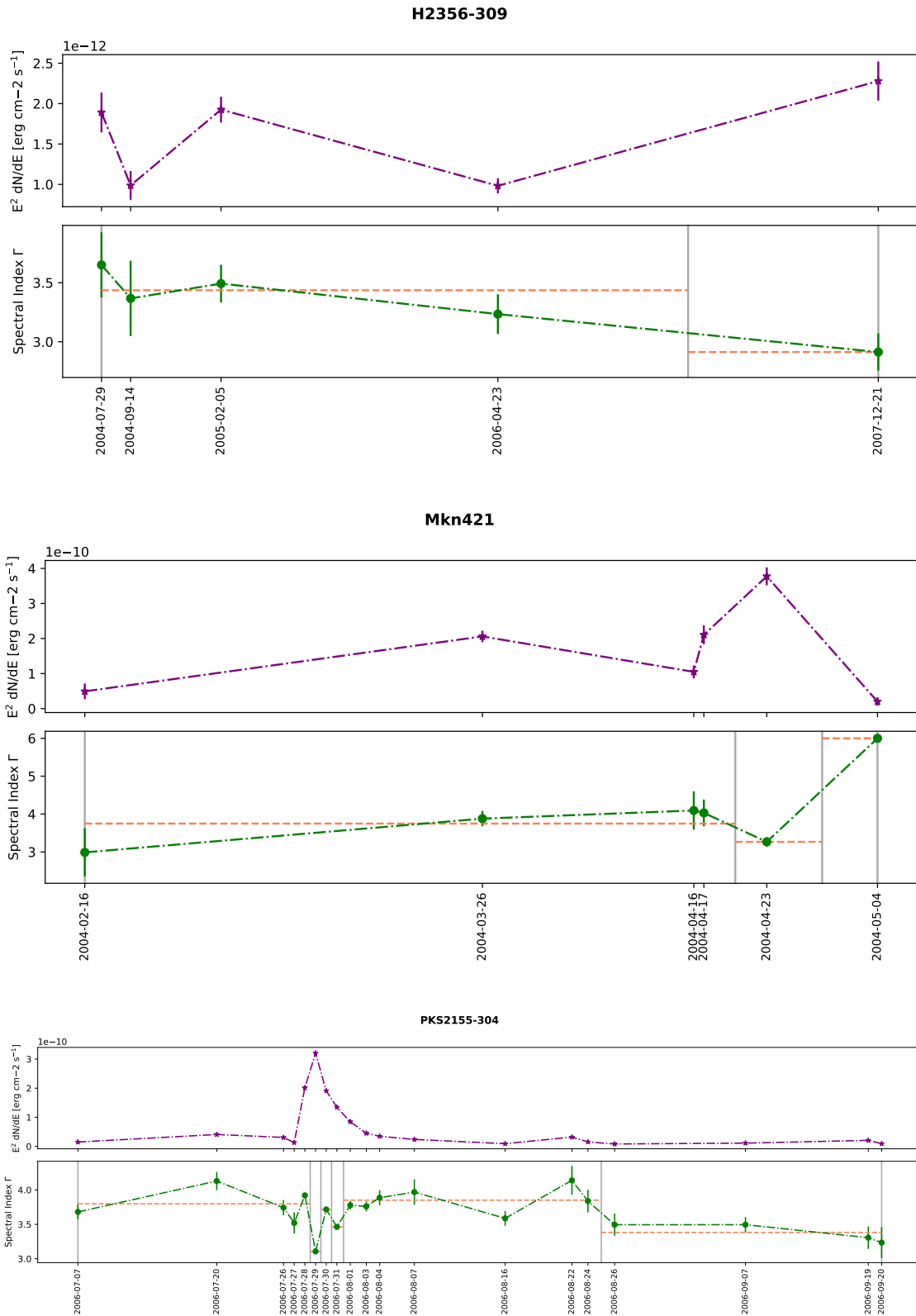


Figure 7.1: Light curves from a few interesting sources [H2356-309, Mkn 421, PKS2155-304] showing the light curve, and below is the respective change in Spectral Index Γ . The vertical lines indicate the segmentation of the data and the orange dotted line is the average spectral index in each block.

7.2.4 Final Segmentation

We begin the process of final segmentation by exploring each individual Bayesian block generated by the previous step. We begin by fitting the spectrum from each block with a simple power law as available with *gammapy* (refer Eq. 7.1). From each, fit we observe the spectral index and flux normalization values and study trends in these parameters over time. By understanding how the spectral index changes with respect to the observed flux, we gain clearer indications of how the source is behaving over time in each block. Illustrated in Fig. 7.1 are three sources which displayed relatively significant variability. Shown in the plots are the individual Bayesian blocks for each of the data sets. The plot shows a light curve (average flux over time), and the relative spectral index at each point in time. Plotted with the spectral index points are the data segment boundaries and the average spectral index for each block. Such plots allow us to make educated choices when making decisions regarding the segmentation of our data.

Having determined blocks where the trends in spectral index relative to the respective change in flux normalization are significant, the final decisions regarding data segmentation can be made. We manually check each of our sources and determine where it is reasonable to merge blocks and where it is important to keep the data segmented. The general rule of thumb we follow here is to merge data blocks which do not show significant variability ($< 2\sigma$) in spectral hardness relative to the flux normalization, and leave the rest segmented. We arrive at the final segmentation after careful consideration and deliberation of each individual data set. The final data segments have been shown in Table 7.3, which also details results of spectral model fits which we perform in the upcoming stages of analysis to determine the intrinsic spectra of our sources.

7.3 Upturn Searches

7.3.1 Intrinsic Spectra

Having constructed our data set with segmentation where necessary, we proceed toward our end goal of searching for ALP induced upturns in the spectra of our sources. The first step in performing such an analysis is to establish the best intrinsic spectral models for each data segment we have available after the last step. In order to determine this in a statistically motivated manner, we perform fits for each data segment against three standard spectral shapes: a Power Law, a Smooth Broken Power Law and a Log Parabola. We can then compare best fit values for each model to make a meaningful choice for the intrinsic spectral model.

For the Power Law fits we assign the default Power Law model built into *gammapy*, given by the equation:

$$\phi(E) = \phi_0 \left(\frac{E}{E_0} \right)^{-\Gamma} \quad (7.1)$$

where ϕ_0 is the amplitude or flux normalization, E is the energy, E_0 is the reference energy, and Γ is the spectral index.

As a preliminary check for curvature we use a Log Parabola model, with the default model available in *gammapy*. It is described by the equation:

$$\phi(E) = \phi_0 \left(\frac{E}{E_0} \right)^{-\alpha - \beta \log\left(\frac{E}{E_0}\right)} \quad (7.2)$$

where ϕ_0 is the amplitude or flux normalization, E is the energy, E_0 is the reference energy, α is the spectral index, and β is the curvature parameter.

When assigning curved models for the intrinsic spectra, we ultimately choose to assign Smooth Broken Power Law models where a curved model is preferred. We make this choice in order to ensure consistency for the upcoming steps where we introduce an additional Broken Power Law component to our spectral model to fit and search for upturns. With the intention of simplifying our searches in the proceeding steps of our analysis, we modify the built-in spectral models available from *gammaipy* for Smooth Broken Power Laws (single and double break models). The modified equation we use for the Smooth Broken Power Law is as follows:

$$\phi(E) = \phi_0 \cdot \left(\frac{E}{E_0} \right)^{-\Gamma_1} \left(1 + \left(\frac{E}{E_{break}} \right)^{\frac{\Delta\Gamma}{\beta}} \right)^{-\beta} \quad (7.3)$$

where ϕ_0 is the amplitude or flux normalization, E is the energy, E_0 is the reference energy, E_{break} is the break energy, Γ_1 is the index before the break, $\Delta\Gamma$ is its difference with the index after the break, and β is the smoothness parameter.

When performing our intrinsic spectral fits with increasingly complicated models, we always face the risk of over-fitting and producing unrealistic results. To minimize any over-fitting, we actively constrain various parameters to be within expected and/or reasonable limits for each source. First, we limit the fit range for the curved component in every case to be within energies in the optically thin region ($\tau < 1$) for each source. We calculate the energy at which $\tau = 1$ for each source using the *ebtable* python library (Meyer, 2024) and actively apply this limitation to each fit. This ensures that our fit does not include the EBL cut-off feature and only provides us with information regarding the intrinsic spectrum alone.

Shown in Table 7.3 are the individual segments, their selected date ranges and the respective C statistic ($C = -2 \ln \mathcal{L}$) values of our fits for the different intrinsic spectral models over each segment. We perform the fits alongside a Dominguez EBL model for completeness, but ensuring the EBL cutoff component is not included in the intrinsic spectrum using the limits we describe earlier. Shown in the final column is the choice we make for the intrinsic spectral model for each segment. The respective intrinsic model will be utilized for each segment in the proceeding steps of our analysis.

Source Name	Range [yyyy.mm.dd]	Power Law	SB PowerLaw	Log Par.	Chosen Spectral Model
1ES 0229+200	2005.01.01 - 2012.12.31	13.08	13.09	13.07	Power Law
1ES 0347-121	2006.01.01 - 2009.12.31	17.23	17.29	16.63	Power Law
1ES 0414+009	2006.01.01 - 2010.12.31	11.97	11.59	11.61	Power Law
1ES 1101-232	2004.01.01 - 2008.12.31	26.41	25.59	25.97	Power Law
1ES 1312-423	2004.01.01 - 2010.12.31	10.69	10.69	10.46	Power Law
1RXS J101015.9-311909	2007.01.01 - 2010.12.31	9.98	9.98	4.46	Power Law
H2356-309	2004.01.01 - 2006.12.31	12.89	12.88	12.88	Power Law
	2007.01.01 - 2007.12.31	15.64	15.65	15.03	Power Law
Markarian 421	2004.02.15 - 2004.04.18	13.21	12.65	10.93	Power Law
	2004.04.19 - 2005.01.01	23.99	22.43	20.10	Power Law
	2010.01.01 - 2010.12.31	15.93	9.82	8.86	SB Power Law
Markarian 501	2014.01.01 - 2014.12.31	17.96	12.85	12.76	SB Power Law
PG 1553+113	2012.01.01 - 2012.12.31	8.33	8.04	9.80	Power Law
	2019.01.01 - 2019.12.31	21.61	20.66	20.89	Power Law
PKS 0447-439	2009.01.01 - 2010.12.31	14.45	14.17	13.95	Power Law
PKS 1510-089	2016.01.01 - 2016.12.31	39.70	39.70	36.74	Power Law
	2006.07.07 - 2006.07.29	20.72	20.23	9,336.33	Power Law
PKS 2155-304	2006.07.29 - 2006.07.30	676.29	91.03	117.24	SB Power Law
	2006.07.30 - 2006.07.31	39.05	21.50	9,971.38	SB Power Law
	2006.07.31 - 2006.08.01	62.74	18.91	21.40	SB Power Law
	2006.08.01 - 2006.08.25	83.71	60.88	63.54	SB Power Law
	2006.08.25 - 2006.10.01	22.44	20.95	21.16	Power Law

Table 7.3: Table showing all the final segments used for our analysis, along with the $-2 \ln \mathcal{L}$ statistic values for fits against a Power Law, Smooth Broken Power Law and a Log Parabola, each with a Dominguez EBL model in order to check for intrinsic curvature in each spectrum. Also indicated in the last column is the final chosen intrinsic spectral model for each segment.

Source Name	Range [yyyy.mm.dd]	Power Law		Broken Power Law				Log Parabola		
		Γ	ϕ_0	Γ	$\Delta\Gamma$	E_{break}	ϕ_0	α	β	ϕ_0
1ES 0229+200	2005.01.01 - 2012.12.31	1.74	1.5e-12	1.49	0.39	0.28	4.27e-12	1.73	0.02	1.57e-12
1ES 0347-121	2006.01.01 - 2009.12.31	2.33	1.32e-11	2.18	0.27	0.24	2.8e-11	2.45	-0.21	1.26e-11
1ES 0414+009	2006.01.01 - 2010.12.31	1.84	1.01e-11	0.00	2.50	0.33	3.37e-11	1.61	0.47	1.08e-11
1ES 1101-232	2004.01.01 - 2008.12.31	1.78	1.05e-11	0.18	1.77	0.16	1.02e-10	1.73	0.09	1.09e-11
1ES 1312-423	2004.01.01 - 2010.12.31	2.35	1.49e-12	2.35	0.01	0.84	2.98e-12	2.44	-0.15	1.40e-12
1RXS J101015.9	2007.01.01 - 2010.12.31	2.56	4.52e-12	2.56	0.01	0.58	9.04e-12	3.07	-0.62	3.71e-12
H2356-309	2004.01.01 - 2006.12.31	2.23	9.62e-12	2.05	0.33	0.52	1.87e-11	2.22	0.01	9.67e-12
	2007.01.01 - 2007.12.31	2.05	1.05e-11	2.04	0.02	0.10	2.13e-11	2.19	-0.21	9.71e-12
Mkn 421	2004.02.15 - 2004.04.18	3.64	6.00e-12	0.001	3.77	0.79	2.38e-10	3.22	0.71	6.92e-12
	2004.04.19 - 2005.01.01	2.53	2.45e-12	1.16	1.62	1.05	1.63e-11	2.19	0.84	3.07e-12
	2010.01.01 - 2010.12.31	2.20	8.36e-13	1.14	2.00	5.28	1.73e-12	1.35	4.00	1.44e-12
Mkn 501	2014.01.01 - 2014.12.31	2.22	3.76e-12	0.004	3.00	3.58	1.84e-11	2.06	1.03	4.54e-12
PG 1553+113	2012.01.01 - 2012.12.31	8.24	2.21e-10	5.52	4.99	0.19	3.07e-9	-5.60	10.3	3.48e-10
	2019.01.01 - 2019.12.31	9.72	3.76e-11	6.75	4.96	0.15	1.16e-9	14.42	3.16	8.61e-12
PKS 0447-439	2009.01.01 - 2010.12.31	1.92	7.60e-11	0.39	1.96	0.26	2.90e-10	1.65	0.57	8.11e-11
PKS 1510-089	2016.01.01 - 2016.12.31	1.75	4.99e-11	1.76	0.00	0.24	1.00e-10	2.96	43.51	1.55e-10
	2006.07.07 - 2006.07.29	2.86	7.70e-10	2.66	0.44	0.74	1.36e-9	-0.78	0.03	6.70e-9
	2006.07.29 - 2006.07.30	2.23	1.08e-9	0.39	2.89	0.50	3.14e-9	1.89	0.67	1.37e-9
	2006.07.30 - 2006.07.31	2.96	1.25e-9	2.46	1.18	0.76	1.99e-9	-324.5	1.91e4	1.92e-7
	2006.07.31 - 2006.08.01	2.70	8.29e-10	1.72	1.96	0.57	1.51e-9	2.51	0.37	9.24e-10
	2006.08.01 - 2006.08.25	2.93	1.80e-10	2.26	1.71	0.76	2.69e-10	2.78	0.27	1.92e-10
	2006.08.25 - 2006.10.01	2.61	6.46e-11	1.67	1.31	0.27	1.98e-10	2.53	0.13	6.70e-11

Table 7.4: Table showing all the fit parameter values obtained from the fits for each of the final segments used for our analysis. Shown are the best fit values against a Power Law, Smooth Broken Power Law and a Log Parabola, each along with a Dominguez EBL model, in order to check for intrinsic curvature. ϕ_0 is given in $TeV^{-1} s^{-1} cm^{-2}$ and E_{break} in TeV.

7.3.2 Modeling & Fitting Upturns

With the intrinsic spectra finalized for each data segment, we proceed with searching for upturns in the spectra. We achieve this by introducing an additional break in the Power Law for each spectral model with the goal of fitting for any possible upturns. This results either in a Smooth Broken Power Law or a Smooth Double Broken Power Law being applied to each spectrum for the upturn search. For the Smooth Double Broken Power Law we use essentially the same equation as Eq. 7.3, simply introducing one more smooth break. The equation is specifically given by:

$$\phi(E) = \phi_0 \cdot \left(\frac{E}{E_0}\right)^{-\Gamma_1} \cdot \left(1 + \left(\frac{E}{E_{b1}}\right)^{\frac{\Delta\Gamma_1}{\beta_1}}\right)^{-\beta_1} \cdot \left(1 + \left(\frac{E}{E_{b2}}\right)^{\frac{\Delta\Gamma_2}{\beta_2}}\right)^{-\beta_2} \quad (7.4)$$

where the parameters are the similar to those in Eq. 7.3, but for two breaks and the respective indices indicating which break each respective parameter describes.

Employing the additional break we introduce to our model, we can now probe our spectrum for any indications of upturning. We minimize the risk of over-fitting by limiting the break energy to be strictly above the point at which our Universe becomes optically thick to γ -rays, for the respective source. We calculate this energy similarly to the previous step where we establish the intrinsic spectra by calculating the energy at which $\tau \sim 1$ for the given source. We further ensure that the Power Law is strictly upturning by limiting the $\Delta\Gamma$ value for the upturning break to be only negative values as required by Eqs. 7.3 & 7.4 which describe the spectral models we have applied.

After performing fits over all our data segments, we begin with a preliminary interpretation of our data. While it might seem as apparent as simply checking the fit results, we aim to be more rigorous in our search methodology. The number of photon events we expect to contribute toward an ALP induced upturn are relatively low to begin with. In addition, we have the added limitations of current generation IACTs regarding their sensitivity and resolution. In order to effectively search for these upturns, we explore the fit statistics and trends in depth. We generate statistical surface plots similar to what we did in our work constraining EBL normalization. These indicate the relative change in our goodness of fit: the C statistic ($C = -2 \ln \mathcal{L}$) over a chosen parameter space. Here, we observe the trends in the C statistic value in a parameter space constructed between two parameters as it approaches convergence. The space is constructed between the break energy E_{break} and the spectral index Γ for each data segment. In order to make our results more robust, we perform strictly enforced fits along the parameter space, explicitly selecting ranges for the two relevant parameters in our spectral model. We divide the parameter space into a coarse grid and manually set and freeze the parameter values corresponding to each 2D pixel's coordinates in our space. We then perform the fit and collect the C-stat values. These are then mapped to each corresponding pixel in our grid and coded with a color map. This produces a statistical surface from which we can attempt to gain a deeper insight into the possibility of any significant upturning in any of the spectra in our data set.

The surface shown in Fig. 7.2 illustrates an example of such a statistical surface. The figure on the left shows the color mapped surface of C statistic values across our parameter space, while the figure on the right shows the surface values as a deviance from the pixel which corresponds to the most likely case and thus the lowest value. These types of plots allow us

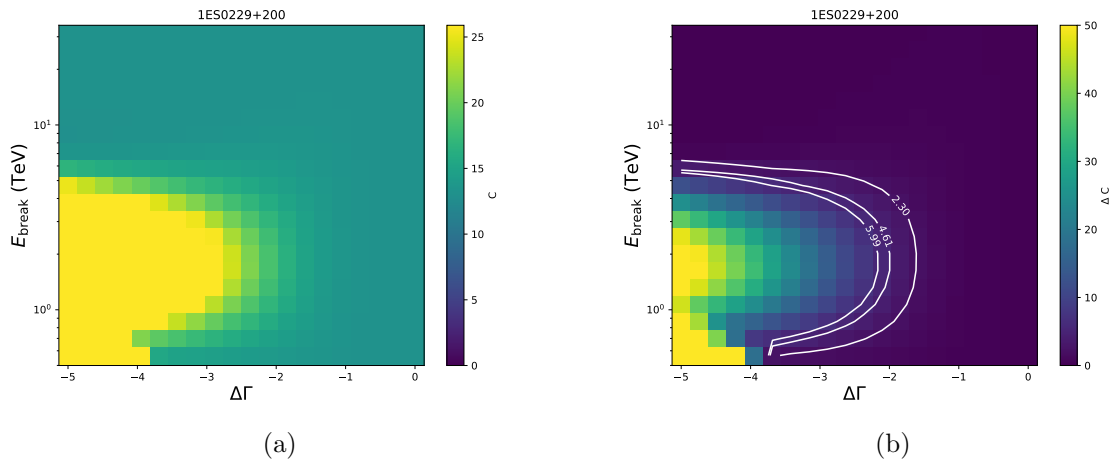


Figure 7.2: Shown here are the statistical surfaces for 1ES0229+200 created for the fit of its spectrum against a Smooth Broken Power Law and Dominguez EBL model. The surfaces are built in a specific parameter space between E_{break} and $\Delta\Gamma$. Fig (a) illustrates as a color map, the C statistic values obtained by forced fits corresponding to each pixel of the parameter space. Fig (b) shows the same space, but with each pixel illustrating its respective difference to the lowest C statistic value, which represents the highest Likelihood. The contours show the p-values corresponding to 1, 2 & 3 σ confidence levels.

to better understand how each of the spectra behave and to make more informed choices when considering the presence of any upturning.

7.4 Searching for ALPs

7.4.1 Simulating ALP upturns

With the searches for general upturning in our spectra having been performed, we can now begin our search for ALPs. We begin this process by modeling the upturns we expect as a consequence of photon-ALP oscillations and the resulting transparency of the Universe to VHE γ -ray photons. To simulate the expected photon-ALP oscillations and the consequent spectral upturns caused by these oscillations, we employ the *gammaALPs* open source framework (Meyer et al., 2021). We follow a similar process as in the earlier study regarding ALP induced wiggles. For this project, we run simulations by specifying an ALP mass, a coupling $g_{a\gamma\gamma}$, an Inter-Galactic Magnetic Field (IGMF) value, a Milky way magnetic field model, and an EBL model.

For the purposes of our simulations here, we limit our search to a single ALP mass, $m_{ALP} = 10^{-3}$ neV. We limit the coupling values $g_{a\gamma\gamma} = 1.0, 3.0 \text{ \& } 5.0 \times 10^{-11}$ GeV $^{-1}$. We provide an IGMF value of 1 nG and use the Jansson and Farrar (JF12) model (Jansson & Farrar, 2012) for the Milky way magnetic field as provided with the *gammaALPs* package. The JF12 model incorporates numerous components like a large-scale regular field including the disk, halo and out-of-plane components. It includes a random field component which accounts for small-scale turbulence, and a striated random field which provides randomly oriented field lines.

For EBL models we chose the Dominguez (Dominguez et al., 2011), Finke (Finke et al., 2022) and Saldana-Lopez (Saldana-Lopez et al., 2021) models. These are widely used in the

field and each have certain advantages for specific use cases. We run simulations for each source by providing the respective position and redshift, running 100 pseudo-random simulations per source. Our analyses concerning these simulations are treated in a statistical manner with the results from the 100 realizations being treated as distributions which statistically represent the overall ALPs case for each source and each set of parameters and/or models.

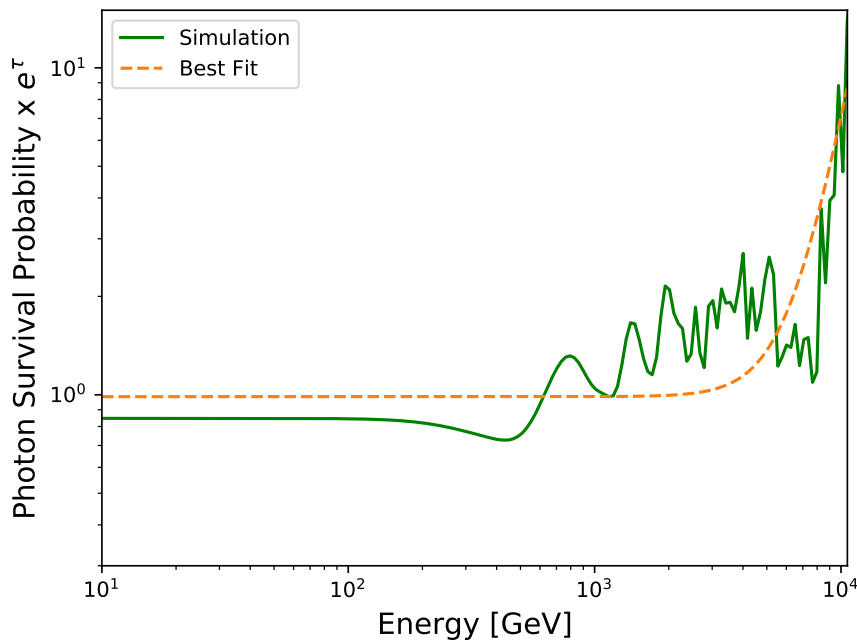


Figure 7.3: Shown here is one example of a pseudo-randomly generated realization of an ALP induced upturn and its best fit against a Smooth Broken Power Law. This is specifically for the source 1ES0229+200, using the Dominguez EBL model and with $m_{ALP} = 10^{-3}$ neV and $g_{a\gamma\gamma} = 5.0 \times 10^{-11}$ GeV $^{-1}$.

Once the simulations for every possible combination of mass, coupling and EBL model are produced for each source, we proceed with the next step in our analysis. The simulations initially produce photon survival probabilities along the energy range for each pseudo random realization of the magnetic fields along the l.o.s. We multiply these probability values by e^τ to obtain the expected upturns for each source. What we obtain are these wiggly upturning spectra as shown in the example provided in Fig. 7.3. In order to effectively compare our simulated upturns with our observational data, we fit each wiggly pseudo-randomized realization against a smooth broken power law, as is also shown in Fig. 7.3. We extract the best fit values for the curve parameters for each realization, producing a set of 100 best fit parameter values per source. These are then utilized in the final stage of our analysis, where we attempt to make statistically motivated comparisons between our models and make meaningful statements regarding statistical preferences for either an ALP or a no-ALP scenario.

7.4.2 Comparing Fits

For the final step in our analysis, we must be able to meaningfully compare our simulated upturns against the fits we performed with our observational data. To achieve this, we first return to the statistical surfaces we created from our upturn searches in the individual source spectra. To make a statistically fair comparison between our pseudo-random models and real data, we

need to establish what parameter values fairly represent each case: the ALPs & no-ALPs. For the ALPs case, we consider the distribution of E_{break} and $\Delta\Gamma$ best fit values from each fit we perform against the simulated spectra. For each data segment, we take the 100 simulation based parameter sets as a non-Gaussian distribution, considering the E_{break} and $\Delta\Gamma$ values from each of the individual simulations as contributing toward the overall result. We perform a rectilinear bivariate spline against the upturn statistical surface for each respective data segment using the method available in the Python library *scipy*v1.14 (Virtanen et al., 2020). We use the interpolation method to estimate the C-statistic value for each given combination of E_{break} and $\Delta\Gamma$ on the provided statistical surface, thus ensuring its compliance with the trend in our fits.

Thus, we obtain a list of C-statistic values, one for each of the 100 pseudo-random ALP models per data segment. This gives us a distribution of 100 C-statistic values per data segment which we consider as collectively representing the ALPs case. We consider the 5th percentile of this non-Gaussian distribution to be fairly representative of the overall distribution, and thus consider this to be the C-statistic value representing the ALPs case for the respective data segment and respective parameters. For the no-ALPs case, we utilize the C-statistic value from the top right pixel in our statistical surface to reasonably represent that particular case. This choice implies that $\Delta\Gamma$ is 0, thus enforcing strictly no upturn in the spectral index, and that the break energy is at the maximum, further ensuring that there is no upturn in this case.

With our likelihood values for the two cases now available, we can make meaningful comparisons using a log likelihood ratio test. Following the rules for such a test, we subtract the C-statistic values ($-2 \ln \mathcal{L}$) in order to test for preference of one or the other model. Here, we subtract the C-statistic value of the no-ALPs case from the ALPs case to check for preference in each data segment. The implication of our results would be that a negative value for this difference indicates a preference for the ALPs model, whereas a positive value would contradict any such preference. The values we obtain for these ratio tests have been reported in Table 7.5 for each coupling value and each EBL model. We add the individual values of all data segments for each specific case to make a final comparison, as is permitted by the rules of a log likelihood analysis. This brings us to the conclusion of our main analysis, and we can now attempt to make meaningful and statistically motivated interpretations of our results.

		$C_{ALP} - C_{NoALP}$								
		Dominguez			Finke22			Saldana - Lopez		
Source Name	Range [yyyy.mm.dd]	1.0	3.0	5.0	1.0	3.0	5.0	1.0	3.0	5.0
1ES 0229+200	2005.01.01 - 2012.12.31	0.0016	0.0076	0.2728	-0.0436	-0.4918	-0.6514	-0.0243	-0.1059	-0.1520
1ES 0347-121	2006.01.01 - 2009.12.31	-0.0440	-0.1595	-0.5330	-0.0188	-0.1376	-0.5169	-0.0365	-0.2731	-1.0704
1ES 0414+009	2006.01.01 - 2010.12.31	0.0724	0.1557	0.1797	0.0419	0.1176	0.1348	0.0545	0.1322	0.1348
1ES 1101-232	2004.01.01 - 2008.12.31	0.0474	0.1332	0.4520	0.0288	0.1313	0.3629	0.0284	0.1302	0.3022
1ES 1312-423	2004.01.01 - 2010.12.31	-0.0354	-0.0282	-0.1353	-0.0484	-0.0276	-0.0959	-0.0559	-0.0423	-0.1373
1RXS J101015.9	2007.01.01 - 2010.12.31	-0.0717	-0.1335	-0.6447	-0.0610	-0.1098	-0.4794	-0.0636	-0.1395	-0.5728
H2356-309	2004.01.01 - 2006.12.31	0.0097	0.0347	0.2375	0.0140	0.0625	0.2741	0.0041	0.0194	0.0925
	2007.01.01 - 2007.12.31	-0.0409	-0.1494	-0.6403	-0.0381	-0.2183	-0.6675	-0.0490	-0.1741	-0.5632
Markarian 421	2004.02.15 - 2004.04.18	0.0130	0.0449	0.7330	0.0098	0.0383	0.0440	0.0084	0.0372	0.0384
	2004.04.19 - 2005.01.01	0.0188	0.0651	1.2733	0.0164	0.0638	0.0734	0.0125	0.0548	0.0567
	2010.01.01 - 2010.12.31	-0.0417	-0.0736	0.0087	-0.0435	-0.0778	-0.0772	-0.0472	-0.0864	-0.0848
Markarian 501	2014.01.01 - 2014.12.31	-0.3491	-0.3491	-0.8258	-0.1503	-0.1928	-0.1934	-0.3339	-0.3408	-0.3418
PG 1553+113	2012.01.01 - 2012.12.31	0.0544	0.051	0.0510	0.0216	0.0214	0.0218	0.0349	0.0350	0.0341
	2019.01.01 - 2019.12.31	-0.1523	-0.1518	-0.1529	0.0165	0.0165	0.0171	-0.0394	-0.0387	-0.0387
PKS 0447-439	2009.01.01 - 2010.12.31	0.2057	0.228	0.2392	0.1192	0.1814	0.1992	0.1556	0.2033	0.2074
PKS 1510-089	2016.01.01 - 2016.12.31	0.5967	0.6029	0.6625	0.3165	0.4529	0.4606	0.4499	0.5132	0.5096
	2006.07.07 - 2006.07.29	0.0484	0.3618	6.2779	0.1127	0.9115	2.7944	0.0574	0.8483	3.5036
	2006.07.29 - 2006.07.30	-2.1616	-3.1249	8.8230	-3.0664	-4.9930	2.5807	-2.7692	-4.3252	4.5299
	2006.07.30 - 2006.07.31	0.0112	0.0631	3.5869	0.0010	0.0035	1.1433	0.0056	0.0461	2.1219
	2006.07.31 - 2006.08.01	-0.0846	-0.4352	-0.7812	-0.1307	-0.7504	-1.2135	-0.1344	-0.6714	-0.1828
	2006.08.01 - 2006.08.25	-0.0542	-0.1706	0.1922	-0.1294	-0.4589	-0.1605	-0.0929	-0.3173	-0.0517
	2006.08.25 - 2006.10.01	0.0135	-0.9980	-1.0917	0.0254	-0.7869	-1.6606	0.0273	-0.5326	-0.9964
Total:		-1.9427	-4.0258	18.1848	-3.0064	-6.2442	2.3900	-2.8077	-5.0276	7.3392

Table 7.5: Table reporting the preference values of no-ALP vs. ALP cases, where negative values indicate a preference for the ALP model and vice versa. Values are reported for $g_{a\gamma\gamma} = 1., 3. \& 5 \times 10^{-11} \text{ GeV}^{-1}$, for the Dominguez, Finke and Saldana-Lopez EBL models.

7.4.3 Statistical Interpretation

Each total value obtained in Table 7.5 represents the preference for that specific EBL model and coupling value when comparing a no-ALPs model with an ALPs model. These values reflect the overall result of our complete data set. We approximate the statistical confidence level of each value by its square root. This implies that our largest value of 18.1848 indicates a preference for the no-ALPs case at $\sim 4\sigma$ for $m_{ALP} = 10^{-3}$ neV, $g_{a\gamma\gamma} = 5 \times 10^{-11}$ GeV $^{-1}$, for an IGMF value of 1 nG, using the JF12 model for the Milkyway B-field and the Dominguez model (Dominguez et al., 2011) for the Extra-galactic Background Light. This can also be re-phrased as excluding the ALPs case for said parameters at $\sim 4\sigma$.

We can interpret the rest of our values in a similar fashion, observing indications of preference for either case, depending on the specifics of our analysis. As is evident, no other results seem to indicate any strong preference for either model. We see the strongest preference for the ALPs case at $g_{a\gamma\gamma} = 3 \times 10^{-11}$ GeV $^{-1}$ for the Finke22 EBL model (Finke et al., 2022), giving us a preference of $\sim 2.5\sigma$. This may speculatively hint at a possible ALP signal in this region, but cannot be considered to have enough statistical significance to claim a detection of any sort.

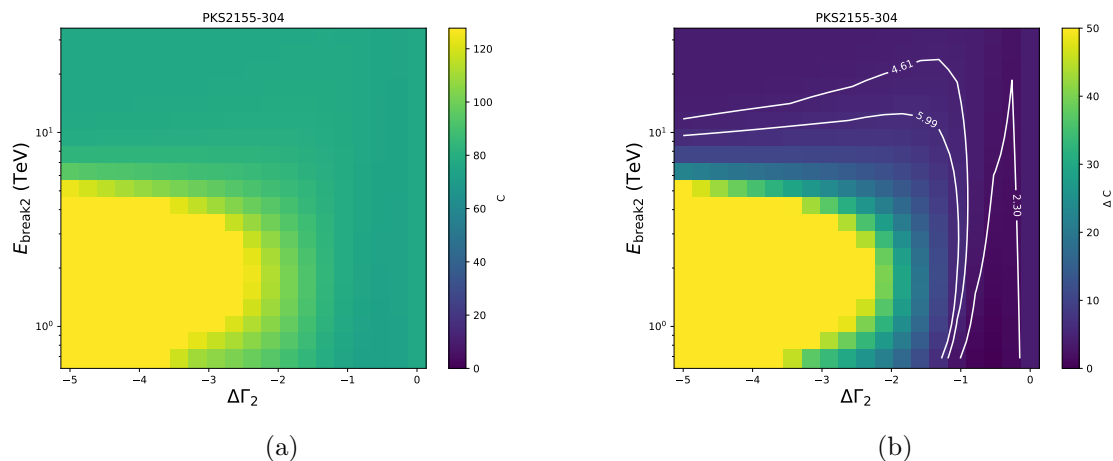


Figure 7.4: Shown here are the statistical surfaces for PKS 2155-304 created for the fit of its spectrum against a Smooth Double Broken Power Law with the Dominguez EBL model. The surfaces are built in a specific parameter space between E_{break2} and $\Delta\Gamma_2$.

Just as earlier, Fig (a) illustrates the C statistic values obtained by forced fits corresponding to each pixel of the parameter space. Fig (b) shows the same space, but with each pixel illustrating its respective difference to the lowest C statistic value. The contours show the p-values corresponding to 1, 2 & 3 σ confidence levels.

In general we see here that one particular data segment seems to have a dominant contribution toward the total: the segment with data from PKS 2155-304 between 2006.07.29 & 2006.07.30. Referring to Fig. 7.1, we see that this segment is during the peak of a flare. Such dominance is then expected during such strong flares where the blazar emission is atypically high, particularly at the highest photon energies. Fig. 7.4 shows the statistical surfaces produced for that data segment when fit against a smooth double broken power law, with our specific parameter constraints.

Further, we can take a closer look at how these final results compare across the coupling values and for each individual EBL model. Shown in Fig. 7.5 is a plot illustrating how our preference behaves with respect to the coupling values, and for the three EBL models. We define a

parameter λ here which is the deviance of the $C_{ALP} - C_{noALP}$ values from the best case scenario.

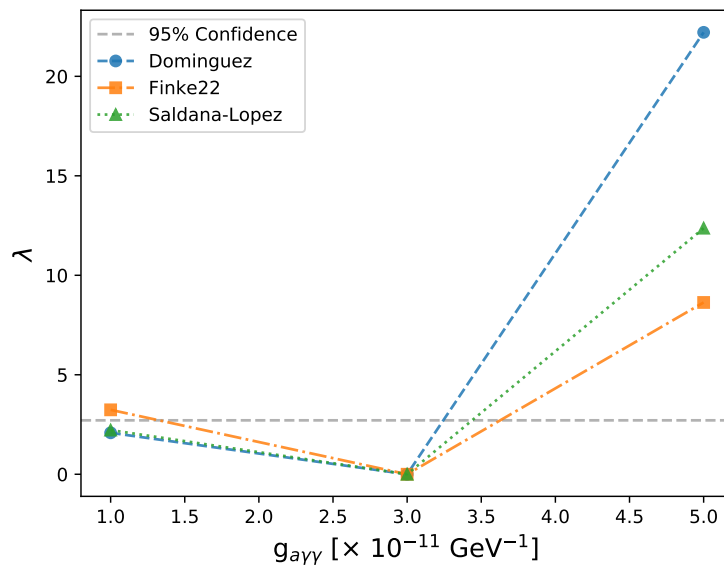


Figure 7.5: A plot illustrating how the preference for ALPs deviates from the respective best case scenario. We show this as a deviance from the lowest $C_{ALP} - C_{noALP}$ value for each EBL model, represented by λ . The grey horizontal line represents a p-value of 2.71 which signifies a confidence level of 95%.

We observe here that for all three EBL models, we have the highest preference for the ALP case at $g_{a\gamma\gamma} = 3.0 \times 10^{-11} \text{ GeV}^{-1}$. The grey horizontal line represents a p-value of 2.71 indicating 95% confidence for the corresponding x-values on the plot. The plot of course does not show a symmetric change around our best case, so we treat it differently in both directions.

What we have demonstrated here through this simple study within a limited parameter space is the potential for this type of work. With further research including an extended data set, more complex models and a wider range of ALP parameters we can expect more comprehensive results. Such an undertaking is already being carried out by colleagues in our working group. The outlook and potential for the foundational work, preliminary searches performed here and the data set itself is explored further in Conclusions & Outlook.

Chapter 8

Conclusions & Outlook

8.1 Constraining EBL Using Messier 87

Upon a thorough analysis over the spectral data of Messier 87, we were able to establish a preference for a curved spectrum to describe the spectrum of the central AGN during flaring or high states. We see this as a statistical preference of $\sim 4\sigma$ for a Log Parabola over a power Law to fit the intrinsic spectrum of our source, specifically in the range of 300 GeV - 10 TeV, where the Universe renders itself optically thin to VHE γ -rays. While this type of curvature has never been observed before in Messier 87, it has been observed in other sources such as NGC1275 (Ansoldi et al., 2018). There are various possible explanations for such behavior including a high state arising from various particle populations, through internal absorption by local photon fields such as starlight within the galaxy or from accretion flow, or due to an intrinsically curved electron spectrum. We can effectively discount any sort of contribution from EBL absorption by the limited energy range we employed specifically with this goal in mind.

We were also able to place upper limits on the normalization of 3 relevant EBL models at $\alpha_{norm} \leq 8.7, 5.5$ & 2.0 for the Kneiske (Kneiske & Dole, 2010), Finke22 (Finke et al., 2010) and Dominguez-upper (Dominguez et al., 2011) models. These results are largely limited by the low redshift of our source at ~ 0.0042 and thus the lack of data available in the optically thick regions. While M87 is located in our Cosmic neighborhood, the hope in selecting this source for EBL studies was reliant on the large amount of VHE statistics available from the source during flares. We might expect an improvement in our results by applying a more comprehensive data set, focused on sources at higher redshifts and emitting at high energies. We have constructed an elaborate data set which is ideal for such research in our project searching for ALP-induced spectral upturns, also presented in this Thesis. Through these improvements we can expect better constraints to be placed through a similar research methodology.

8.2 ALP Searches in Virgo Using Messier 87

In the process of our ALP search in Messier 87, we constructed a complex model for ALP propagation through intergalactic space, traversing the Virgo cluster and Milkyway magnetic fields. We used a Gaussian turbulence model for the Virgo cluster field and the JF12 model (Jansson & Farrar, 2012) for the Milkyway field. We constrained the central magnetic field value for the Virgo cluster at $B_0 = 34.2 \mu\text{G}$ and determined the the fall-off factor $\eta = 0.42$. Using these parameters, we are able to construct simulated models for our expected photon survival probabilities from M87. We constructed all models using the *gammaALPs* open source framework (Meyer et al., 2021).

We explored a coarsely binned 5×5 grid along the ALP parameter space, spanning $m_{ALP} = 3.162 - 316.2$ neV & $g_{a\gamma\gamma} = 4.6 \times 10^{-12} - 10^{-10}$ GeV $^{-1}$. We constructed 1000 pseudo-randomized spectral models for each “pixel” in our parameter space and perform fits of these models against the observed spectrum of M87. We treated our fit results totaling $5 \times 5 \times 1000 = 25,000$ values in a statistical manner and interpret the 5th percentile value of each distribution to represent the ALPs case for the respective pixel. We compared this value against a no-ALPs case represented by a log parabola with a Dominguez EBL attenuation model using a Log Likelihood ratio test. Our results are statistically inconclusive with the strongest preference for the ALPs model being $< 2\sigma$. We also do not see any strong preference for the no-ALPs case, also rendering us unable to set exclusions with statistical confidence.

The inability of our fits to produce statistically significant results may be attributed to a lack of available statistics, or to the limitations of our current generation of γ -ray telescopes, particularly regarding their ability to clearly resolve individual photon energies. To be able to distinguish the fine wiggling of spectra against statistical fluctuations and noise, a high level of energy resolution would prove highly advantageous. We may be able to extend our results by combined analysis with other instruments, which we attempted to perform with data from the MAGIC telescope but were unable to due to external circumstances. We might be able to improve our results by combining analyses with sources such as NGC1275 or IC130 located in the Perseus Cluster using similar methodologies. A similar study has already been carried out utilizing observations of NGC1275 by the MAGIC Collaboration (Abe et al., 2024). There is still potential in the methodology we employ, provided we have enough statistics and technological capability.

Our choice of a Gaussian turbulence model over a cell-by-cell approach, still remains a relatively simple approach and might prove itself to be a limiting factor in the effectiveness of our ALP searches. Further studies conducted using a more complex magneto-hydrodynamic (MHD) model may offer more robust results, proving itself more accurate in modeling these photon-ALP oscillations. MHD simulations are highly effective with regard to modeling the complex interactions occurring between plasma flows and the magnetic fields in such Astrophysical environments and by extension the consequent photon-ALP oscillations in these environments. Studies exploring such MHD models (Vazza et al., 2017, 2021) offer us an opportunity to improve our predictive ability and indicate great research potential in the future. Despite the obvious ability of MHD simulations to model Astrophysical magnetic fields with superior precision, there is a case to be made for the ability of Gaussian turbulent models to make robust predictions in ALP searches even when compared directly to MHD based approaches. This is described in a 2023 study (Carenza, Sharma, Marsh, Brandenburg, & Ravensburg, 2023) which makes a direct comparison between the two.

While our analysis results proved inconclusive in establishing a preference for either an ALP or no-ALP scenario, the potential in this approach toward searching for photon-ALP oscillation wiggles is still a significant one. With improvements being made in our modeling methodology and data set, we might already obtain more robust results. We also expect to see potential improvements in our results with the arrival of next generation γ -ray telescopes. This may not be far off, expecting the arrival of telescopes such as CTAO in the near future. One publication (Abdalla et al., 2017) already explores the potential of CTAO for such precise studies in Cosmology and γ -ray propagation. The potential for improved results with this research approach is realistic and likely with a newer generation of detection instruments and techniques.

8.3 Upturn Searches For ALPs

Our efforts to search for signatures of ALPs via γ -ray transparency effects prompted us to search for upturns in the spectra of 13 candidate blazars. We organized and segmented the data sets where we observe a clear variability in the respective source spectrum in order to minimize biases. We determine the best intrinsic model for each data segment, accounting for possible variability for the same source during flares. We then applied our final comprehensive data set toward fine searches for upturns. We performed fits along a parameter space created between spectral index and break energy values for our expected upturn, recording the C-stat ($-2 \ln \mathcal{L}$) values. We use our results to carefully search for signs of upturning in our spectra.

In order to meaningfully motivate the case for any upturning to be ALP induced, we simulate pseudo-randomized ALP induced upturns using *gammaALPs* (Meyer et al., 2021). We constructed such pseudo-random models for a fixed ALP mass of $m_{ALP} = 10^{-3}$ neV and for varying coupling values $g_{a\gamma\gamma} = 1.0, 3.0$ and 5.0×10^{-11} GeV $^{-1}$. Additionally we also varied our analysis across 3 EBL models: Dominguez (Dominguez et al., 2011), Finke22 (Finke et al., 2022) and Saldana-Lopez (Saldana-Lopez et al., 2021). In each case, we simulated 100 pseudo-randomized realizations of the expected upturn and fit them against a Smooth Broken Power Law, obtaining the best fit results in each case. We interpolate this against the parameter space we created and populated with C-stat values while searching for upturns, thus obtaining a C-stat value for each ALP model. We consider the 5th percentile of the C-stat values from these ALP fits to effectively represent the respective set of parameters. We compare this against our no-ALPs case, taken to be the fit results at zero upturn and highest break energy parameters from our upturn searches. We follow the rules of a Likelihood analysis and add the C-stat values for all data sets modeled with the same parameters, obtaining our final preference values.

While we attempt to implement an ALP induced upturn model to explain any expected upturning in the spectra, there are other possible explanations offered for such spectral upturns. One study suggests that stochastic acceleration scenarios offer a plausible explanation for such upturns (Lefa, Aharonian, & Rieger, 2011). Another study offers a time-independent leptonic model as a possible explanation for this spectral feature (Lefa, Rieger, & Aharonian, 2011). We see in our strongest case, a preference for the no-ALPs case at $\sim 4\sigma$ for $m_{ALP} = 10^{-3}$ neV, $g_{a\gamma\gamma} = 5 \times 10^{-11}$ GeV $^{-1}$, for an IGMF value of 1 nG, using the Jansson model for the Milkyway B-field and the Dominguez model (Dominguez et al., 2011) for the Extra-galactic Background Light. The strongest case for ALP model preference is at $g_{a\gamma\gamma} = 3 \times 10^{-11}$ GeV $^{-1}$ for the Finke22 EBL model (Finke et al., 2022), giving us a preference of $\sim 2.5\sigma$.

During our analysis, we note that for multiple data segments, we observe that most statistics available are in the optically thick region for the source. The individual spectra for each segment have been shown in the Appendix for reference. This limits our ability to model the intrinsic spectra and thus the overall shape of the spectra. Consequently this limits our ability to search for resultant upturns induced by photon-ALP oscillations. This can be remedied by introducing data from other instruments which make observations in the GeV ranges below that of H.E.S.S., such as Fermi-LAT. Colleagues from our research group are currently working toward including data from Fermi-LAT into the data set, extending each spectrum and hopefully by extension the potential of the data set to conduct our ALP searches. The data set itself is a valuable resource for other ALP search methodologies. A subsequent project being undertaken by our research group focuses on searching for EBL contributions through the decay of “heavy” ALPs with masses above 1 eV, similar to work carried out by Korochkin, Neronov and Semikoz (Korochkin, Neronov, & Semikoz, 2020). Within our research group, new models accounting for ALP decay contributions are being developed, and are expected to be applied to

the constructed data set. In general, the high energy statistics and varying redshifts give the data set great potential for many types of axion and ALP searches.

Within the context of the type of research carried out during this Thesis, this data set could be highly effective for use in EBL related studies as well for the same reasons it is useful for ALP searches: varying redshifts and high energy statistics. Studies of similar nature are being carried out by various Research groups and Collaborations (Desai et al., 2019; Ajello et al., 2018; Gréaux, Biteau, & Rosillo, 2024). There are also similar studies being conducted within the H.E.S.S. Collaboration (Abdalla et al., 2017). The data set may also prove useful for studies regarding proton cascades such as undertaken previously by Essey (Essey & Kusenko, 2010, 2014). These studies explore the possibility of of Ultra high energy cosmic ray interactions with background photons, leading to cascades. The secondary γ -rays produced through this mechanism can be detected using our γ -ray telescopes. This cascade itself is predicted to prove dominant in the observed TeV emission from blazars such as those we use to construct our data set. It could also help improve our ability to detect and study distant sources beyond their primary γ -ray emission. Studies with such a data set can also prove useful in research concerning Cosmology, for example regarding the determination of the Hubble Constant and the resolution of Hubble tension (Biteau & Williams, 2015). In summary, the foundation we have been able to provide with this project and the related data set has much potential for future work, both in the field of Axion & ALP searches, and in other Astrophysics related fields. There are projects already ongoing within our research group which will extend the work to provide more comprehensive results.

Appendix A

Upturn Searches For ALPs

A.1 Spectra & Stat Surfaces

Shown ahead are the plots for all of our sources and their respective data segment illustrating the individual spectra as plotted against the chosen spectral model for each segment as reported in Table 7.3. Plotted along with these are the statistical surfaces generated with fits against the same spectral model type. In each case Fig (a) illustrates the C statistic values obtained by the forced fits performed corresponding to each pixel of the parameter space and Fig (b) shows the same space, but with each pixel mapping its respective difference to the lowest C statistic value from the overall.

Note: In some cases like that of PG 1553+113, we see large errors due to the fact that most of our available data is only in the optically thick region of the spectrum for that source. This renders the spectrum degenerate and leads to these errors. As discussed in the Conclusions & Outlook section, we intend to resolve this with future work undertaken by colleagues, extending the spectrum with data from instruments such as Fermi-LAT. Also note that in rare cases, an internal error with *gammapy* causes tick labels to remain in the plots where the error region cross the axes, despite being specified otherwise by our code.

A.1.1 1ES 0229+200

2005.01.01 - 2012.12.31

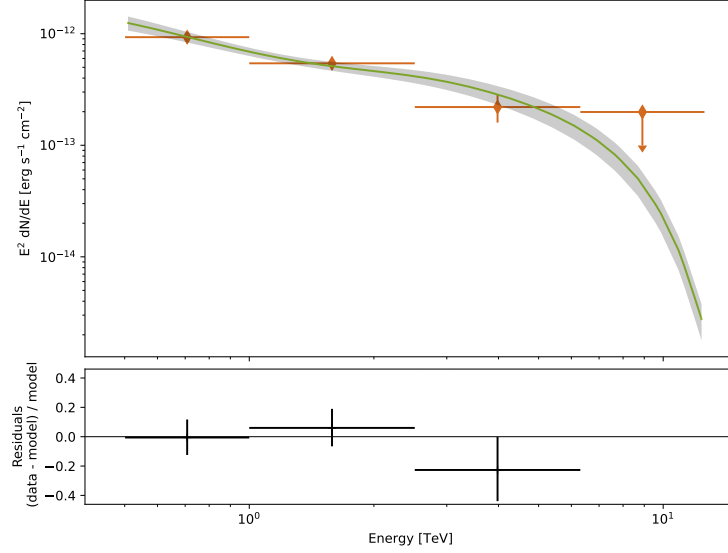


Figure A.1: Best fit spectrum as plotted against a Smooth Broken Power Law with the Dominguez EBL model.

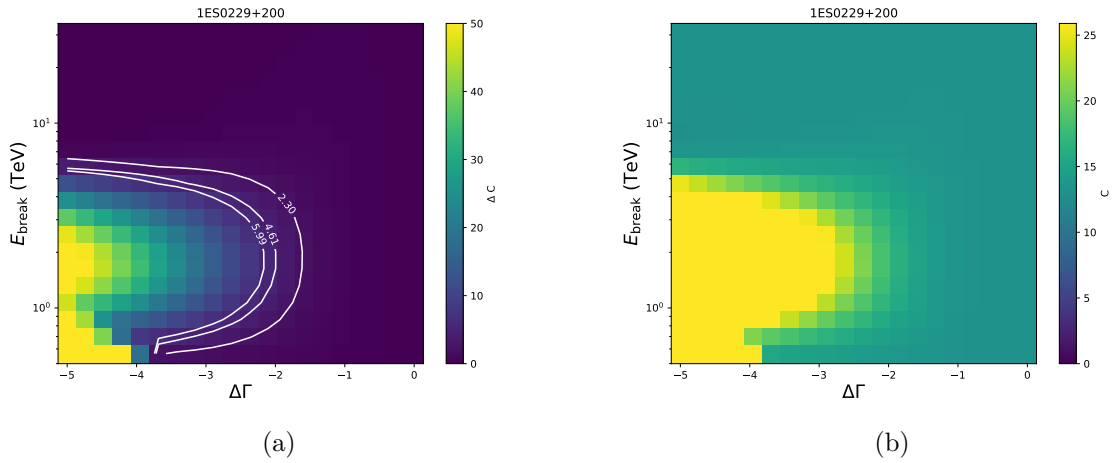


Figure A.2: Statistical surfaces created for the fit of the spectrum against a Smooth Broken Power Law with the Dominguez EBL model. The surfaces are built in a specific parameter space between E_{break} and $\Delta\Gamma$.

A.1.2 1ES 0347-121

2006.01.01 - 2009.12.31

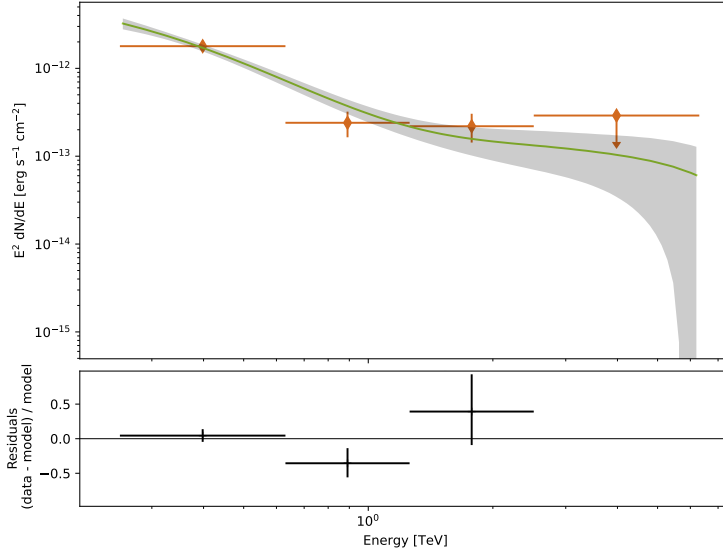


Figure A.3: Best fit spectrum as plotted against a Smooth Broken Power Law with the Dominguez EBL model.

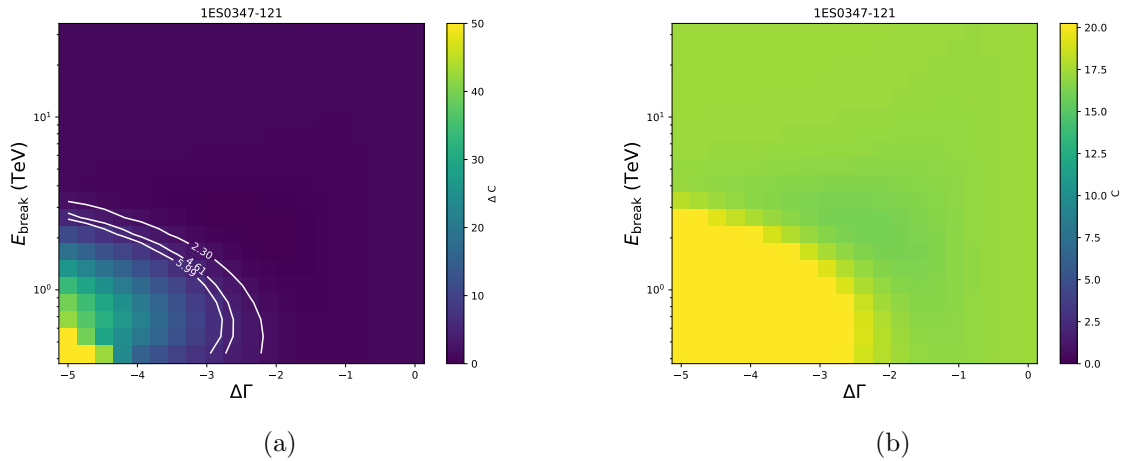


Figure A.4: Statistical surfaces created for the fit of the spectrum against a Smooth Broken Power Law with the Dominguez EBL model. The surfaces are built in a specific parameter space between E_{break} and $\Delta\Gamma$.

A.1.3 1ES 0414+009

2006.01.01 - 2010.12.31

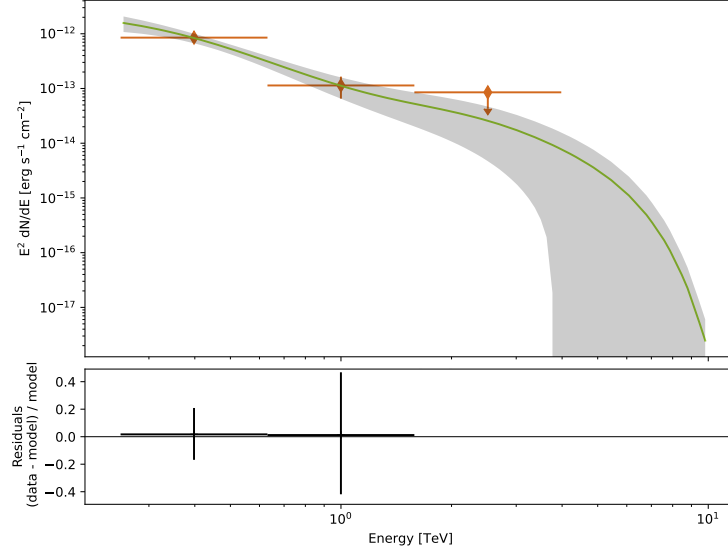


Figure A.5: Best fit spectrum as plotted against a Smooth Broken Power Law with the Dominguez EBL model.

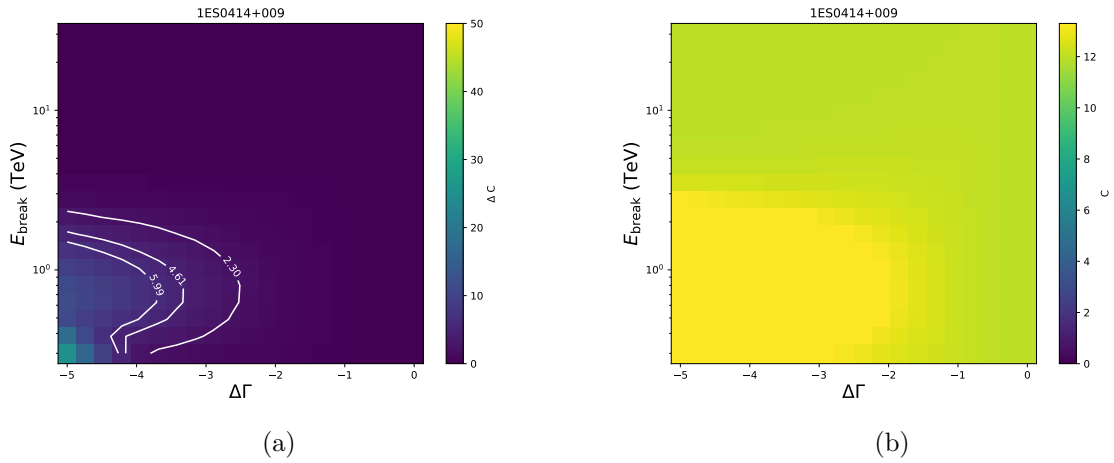


Figure A.6: Statistical surfaces created for the fit of the spectrum against a Smooth Broken Power Law with the Dominguez EBL model. The surfaces are built in a specific parameter space between E_{break} and $\Delta\Gamma$.

A.1.4 1ES 1101-232

2004.01.01 - 2008.12.31

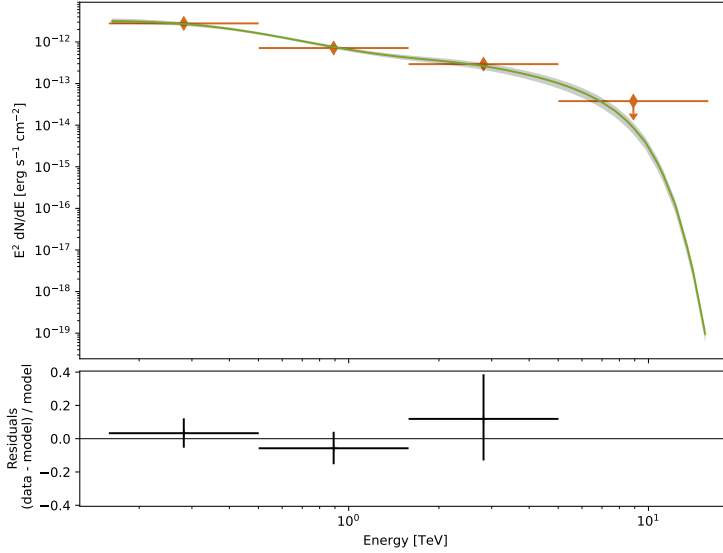


Figure A.7: Best fit spectrum as plotted against a Smooth Broken Power Law with the Dominguez EBL model.

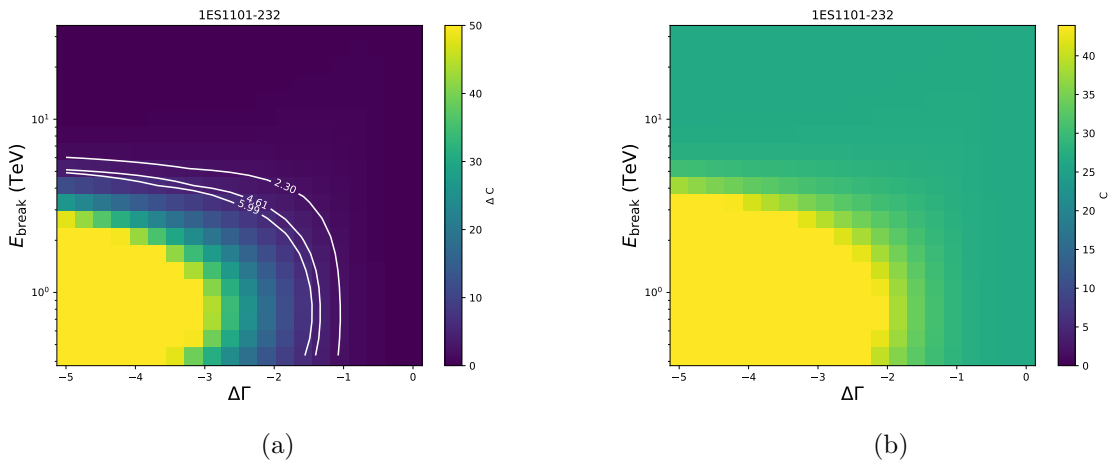


Figure A.8: Statistical surfaces created for the fit of the spectrum against a Smooth Broken Power Law with the Dominguez EBL model. The surfaces are built in a specific parameter space between E_{break} and $\Delta\Gamma$.

A.1.5 1ES 1312-423

2004.01.01 - 2010.12.31

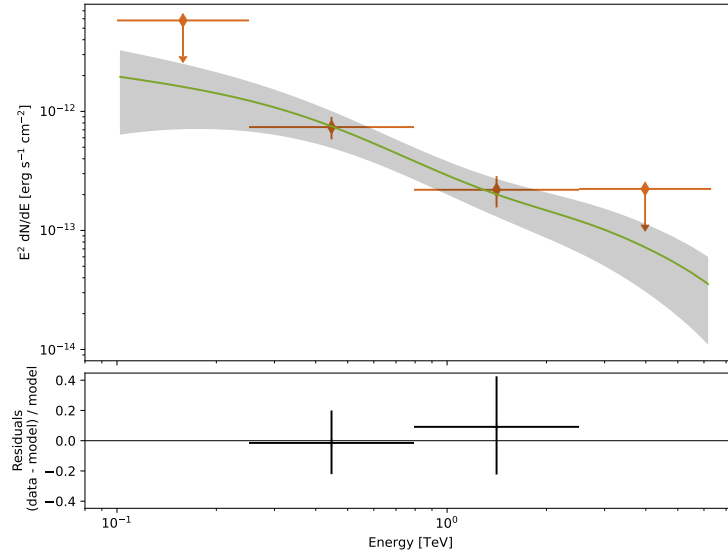


Figure A.9: Best fit spectrum as plotted against a Smooth Broken Power Law with the Dominguez EBL model.

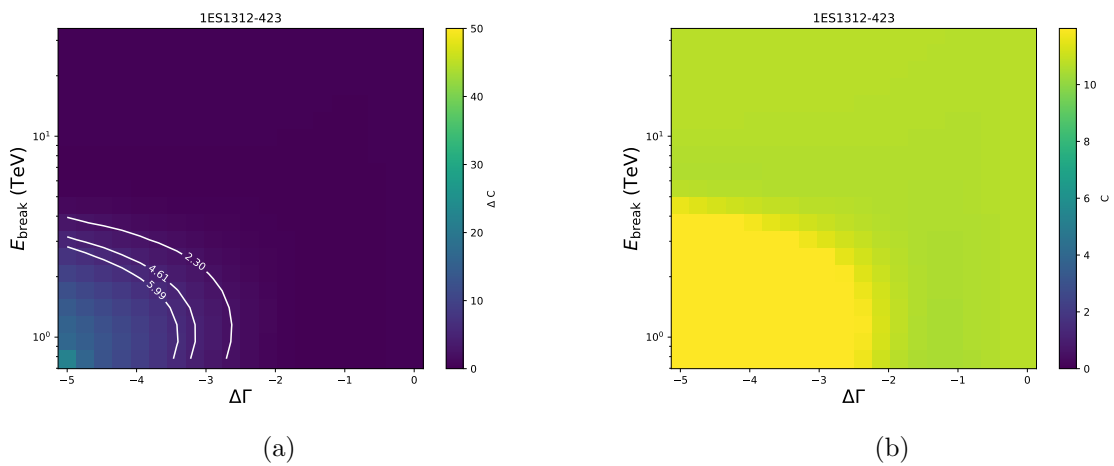


Figure A.10: Statistical surfaces created for the fit of the spectrum against a Smooth Broken Power Law with the Dominguez EBL model. The surfaces are built in a specific parameter space between E_{break} and $\Delta\Gamma$.

A.1.6 1RXS J101015.9

2007.01.01 - 2010.12.31

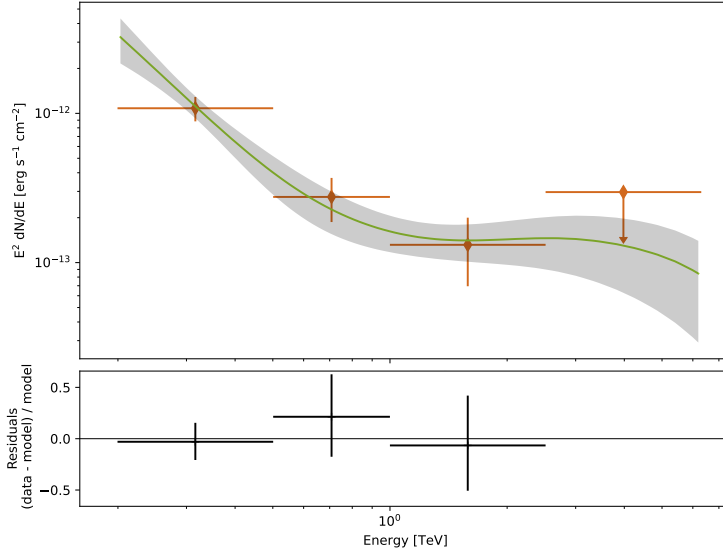


Figure A.11: Best fit spectrum as plotted against a Smooth Broken Power Law with the Dominguez EBL model.

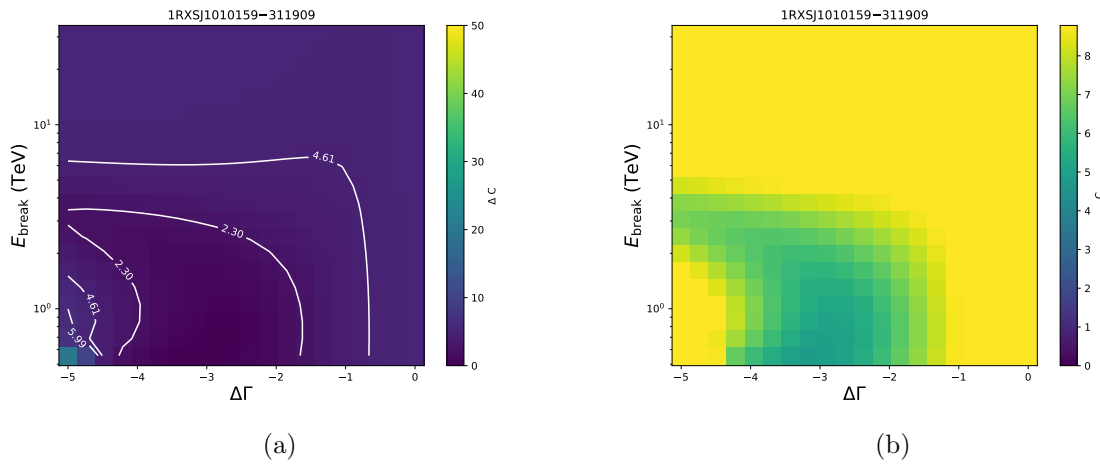


Figure A.12: Statistical surfaces created for the fit of the spectrum against a Smooth Broken Power Law with the Dominguez EBL model. The surfaces are built in a specific parameter space between E_{break} and $\Delta\Gamma$.

A.1.7 H2356-309

2004.01.01 - 2006.12.31

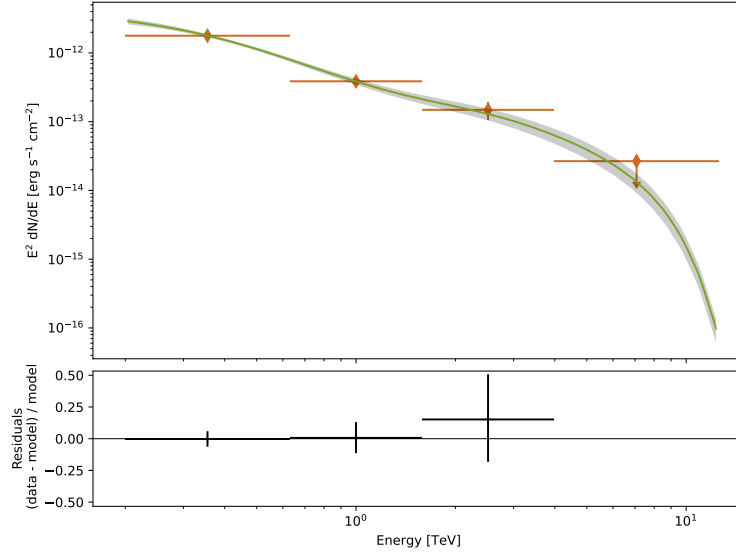


Figure A.13: Best fit spectrum as plotted against a Smooth Broken Power Law with the Dominguez EBL model.

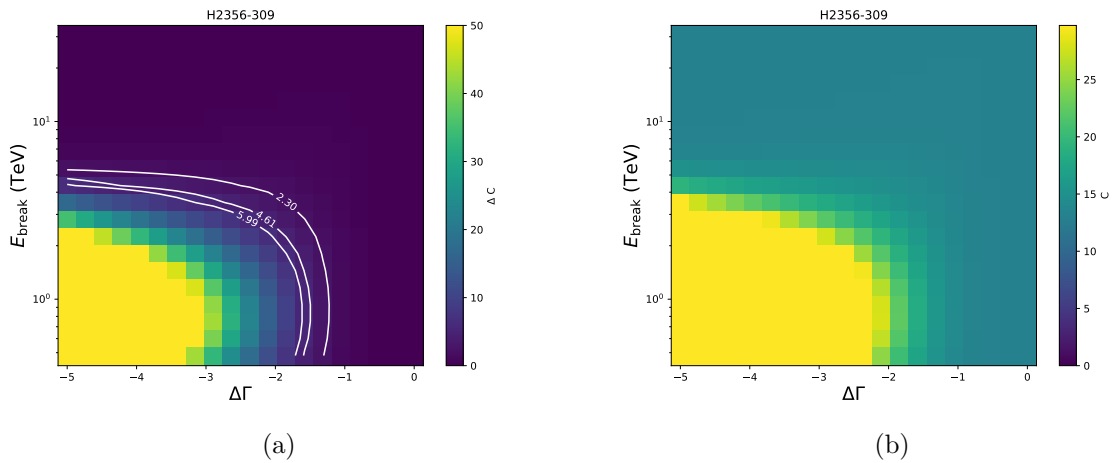


Figure A.14: Statistical surfaces created for the fit of the spectrum against a Smooth Broken Power Law with the Dominguez EBL model. The surfaces are built in a specific parameter space between E_{break} and $\Delta\Gamma$.

2007.01.01 - 2007.12.31

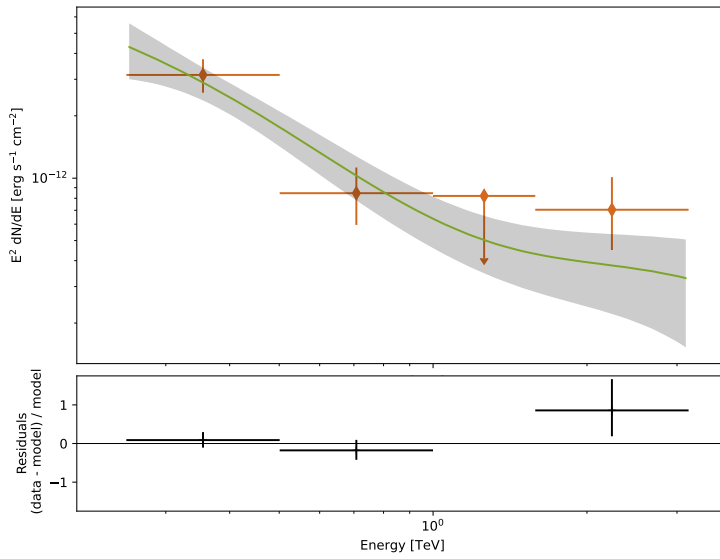


Figure A.15: Best fit spectrum as plotted against a Smooth Broken Power Law with the Dominguez EBL model.

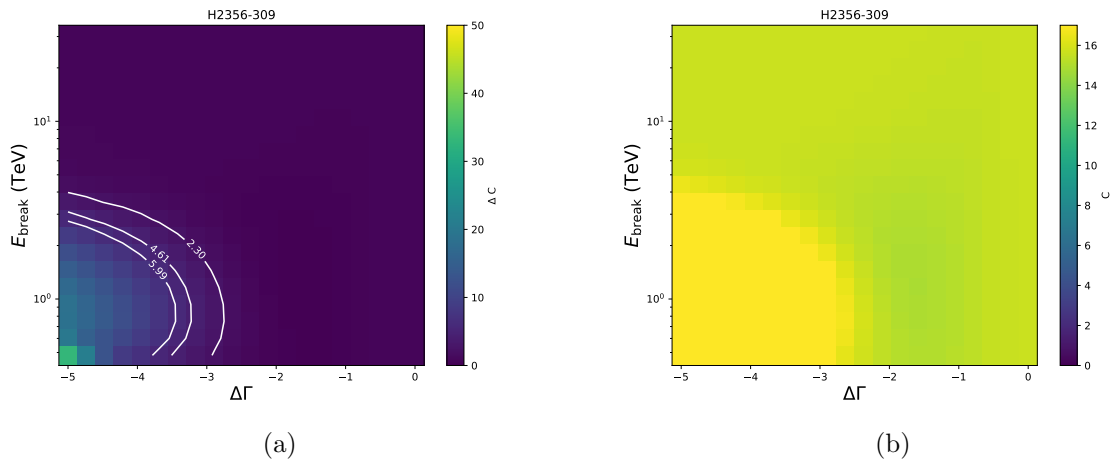


Figure A.16: Statistical surfaces created for the fit of the spectrum against a Smooth Broken Power Law with the Dominguez EBL model. The surfaces are built in a specific parameter space between E_{break} and $\Delta\Gamma$.

A.1.8 Markarian 421

2004.02.15 - 2004.04.18

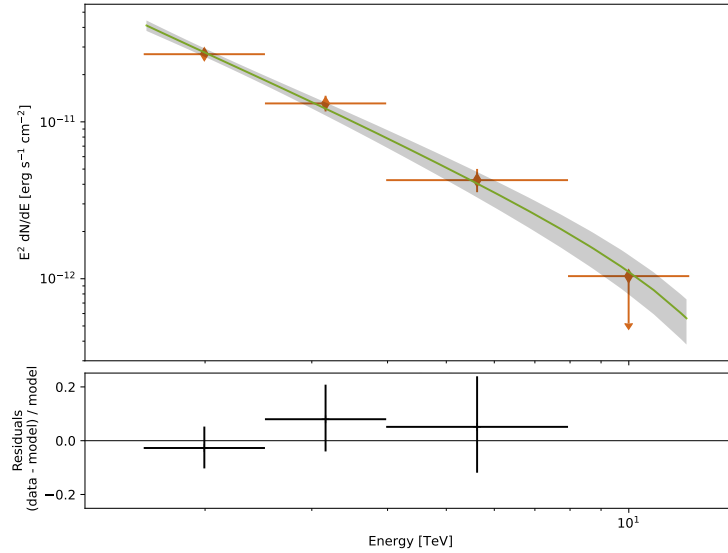


Figure A.17: Best fit spectrum as plotted against a Smooth Broken Power Law with the Dominguez EBL model.

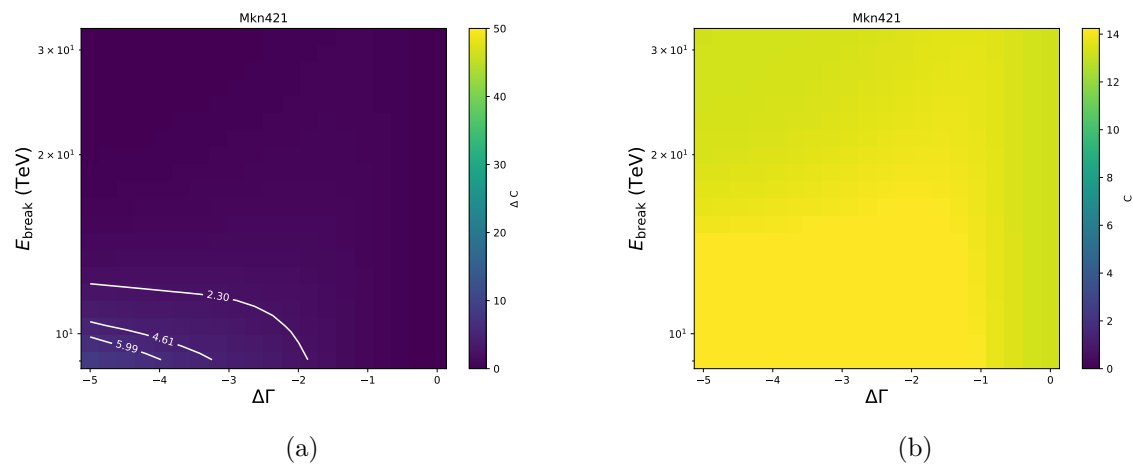


Figure A.18: Statistical surfaces created for the fit of the spectrum against a Smooth Broken Power Law with the Dominguez EBL model. The surfaces are built in a specific parameter space between E_{break} and $\Delta\Gamma$.

2004.04.19 - 2005.01.01

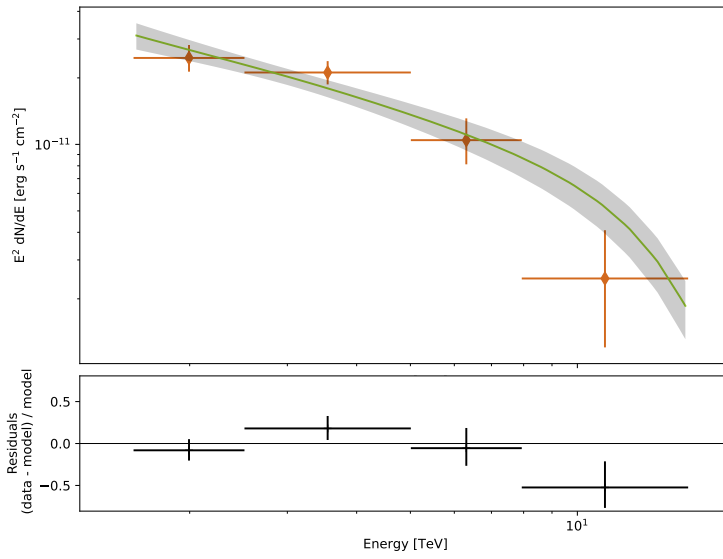


Figure A.19: Best fit spectrum as plotted against a Smooth Broken Power Law with the Dominguez EBL model.

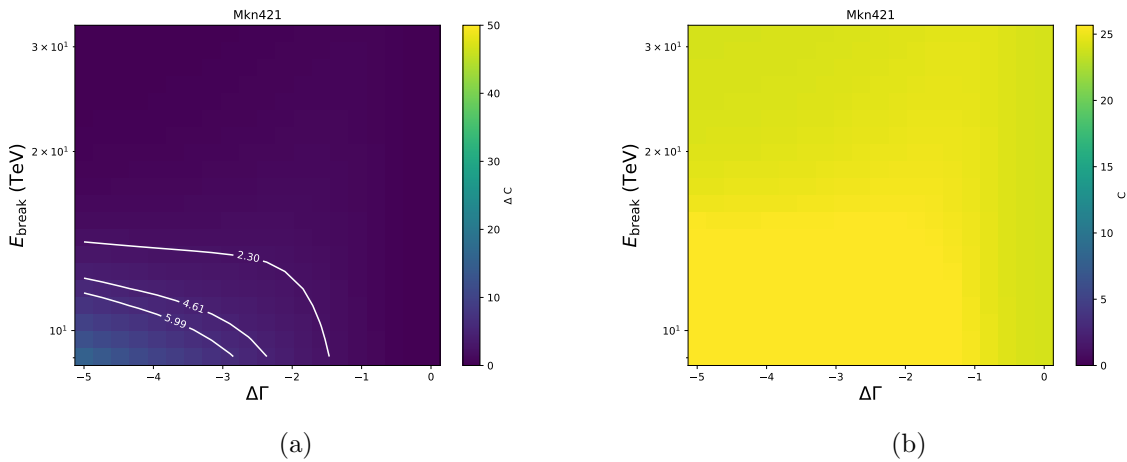


Figure A.20: Statistical surfaces created for the fit of the spectrum against a Smooth Broken Power Law with the Dominguez EBL model. The surfaces are built in a specific parameter space between E_{break} and $\Delta\Gamma$.

2010.01.01 - 2010.12.31

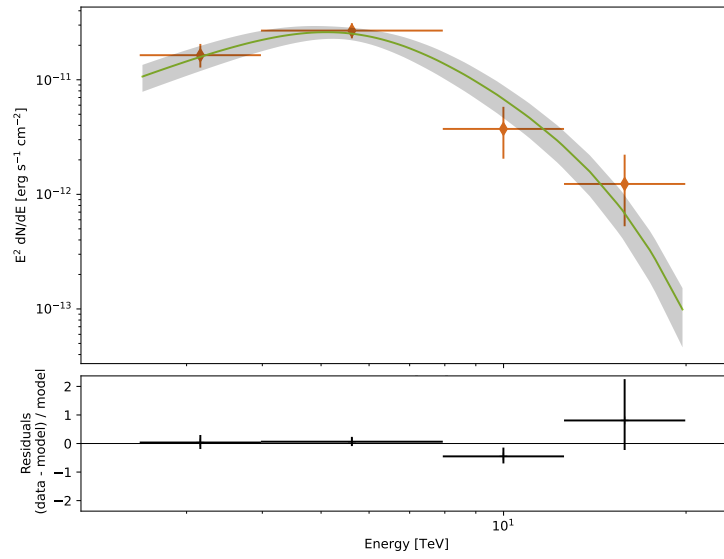


Figure A.21: Best fit spectrum as plotted against a Smooth Double Broken Power Law with the Dominguez EBL model.

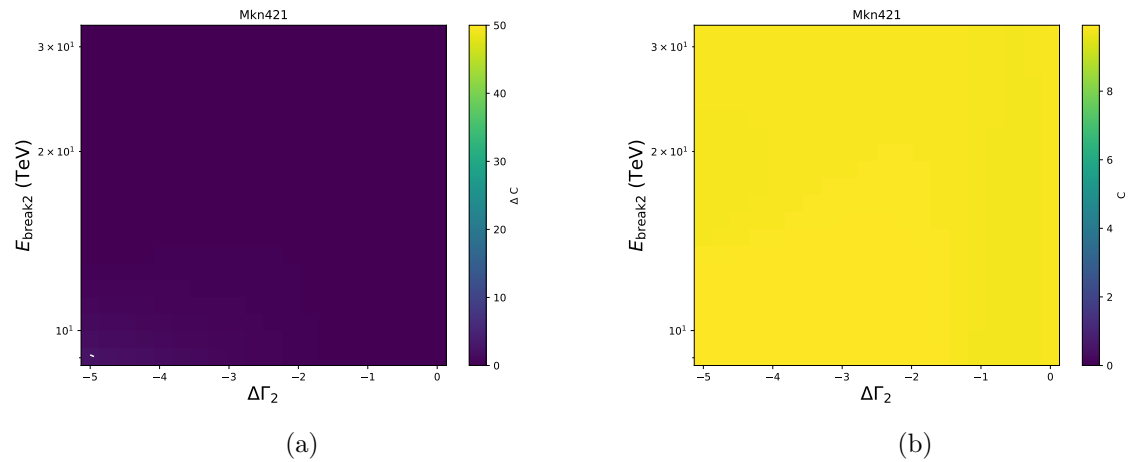


Figure A.22: Statistical surfaces created for the fit of the spectrum against a Smooth Double Broken Power Law with the Dominguez EBL model. The surfaces are built in a specific parameter space between E_{break} and $\Delta\Gamma$.

A.1.9 Markarian 501

2014.01.01 - 2014.12.31

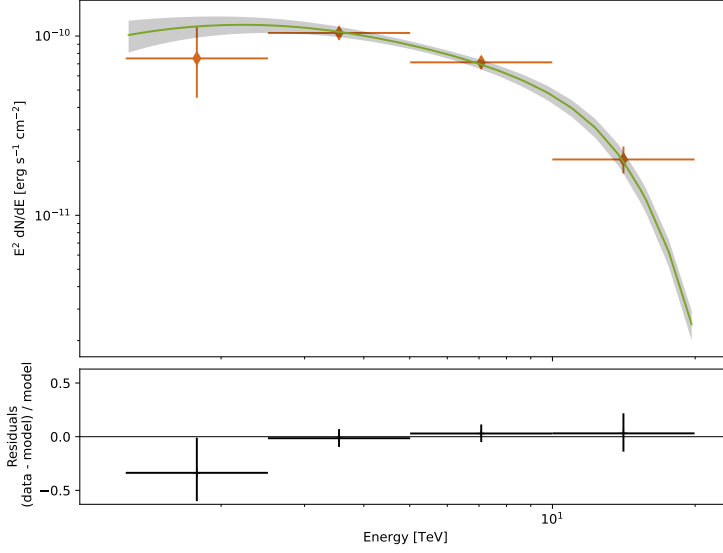


Figure A.23: Best fit spectrum as plotted against a Smooth Double Broken Power Law with the Dominguez EBL model.

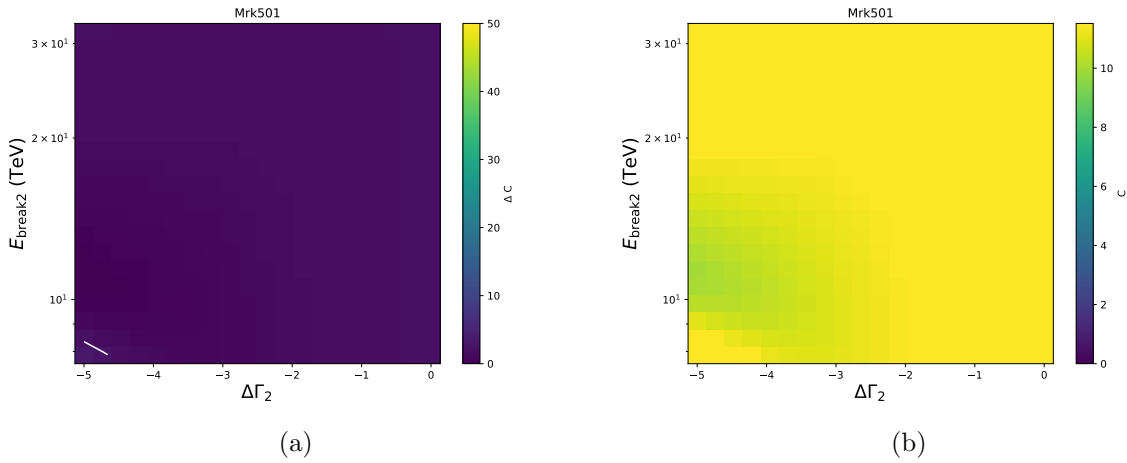


Figure A.24: Statistical surfaces created for the fit of the spectrum against a Smooth Double Broken Power Law with the Dominguez EBL model. The surfaces are built in a specific parameter space between E_{break} and $\Delta\Gamma$.

A.1.10 PG 1553+113

2012.01.01 - 2012.12.31

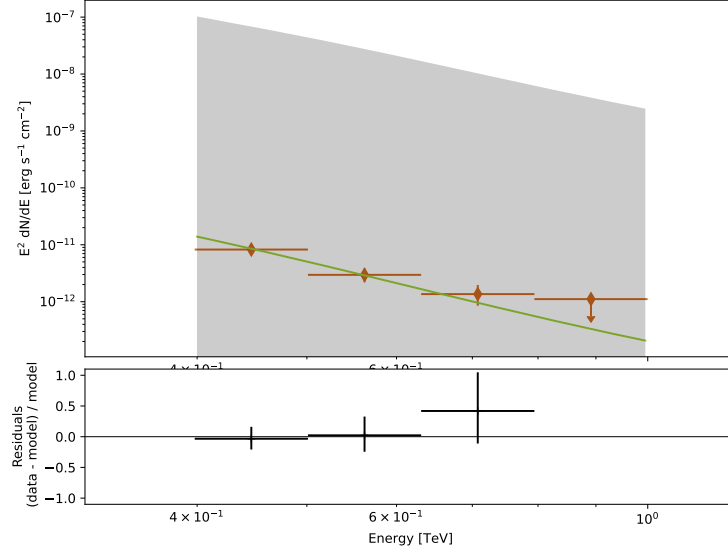


Figure A.25: Best fit spectrum as plotted against a Smooth Broken Power Law with the Dominguez EBL model.

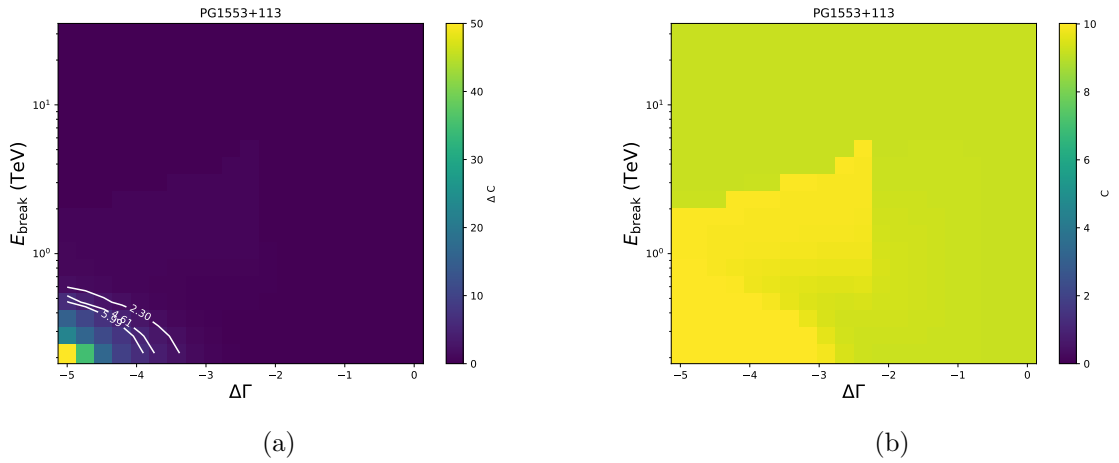


Figure A.26: Statistical surfaces created for the fit of the spectrum against a Smooth Broken Power Law with the Dominguez EBL model. The surfaces are built in a specific parameter space between E_{break} and $\Delta\Gamma$.

2019.01.01 - 2019.12.31

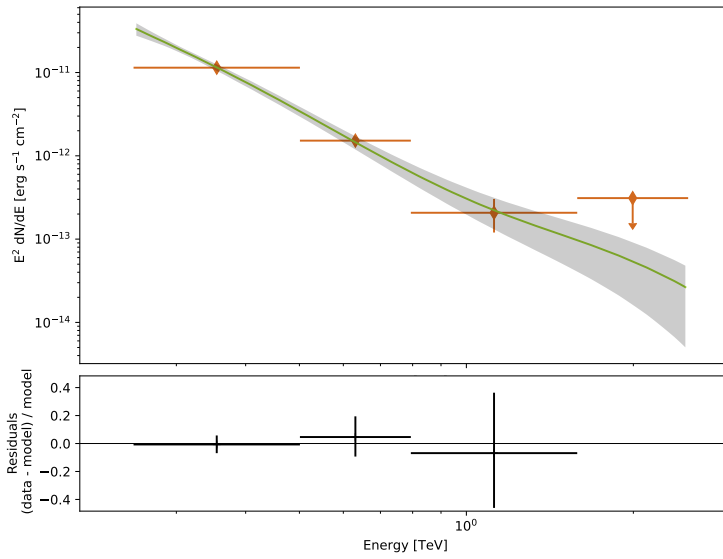


Figure A.27: Best fit spectrum as plotted against a Smooth Broken Power Law with the Dominguez EBL model.

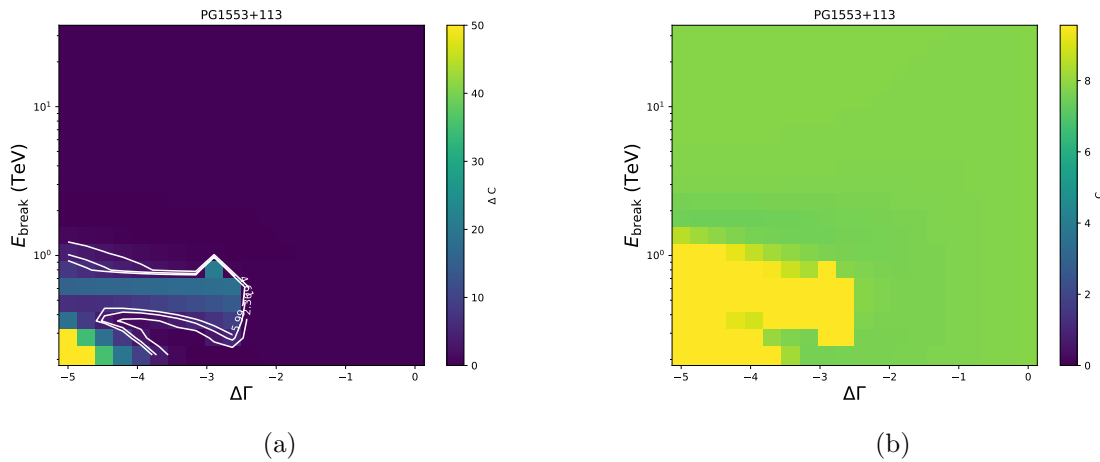


Figure A.28: Statistical surfaces created for the fit of the spectrum against a Smooth Broken Power Law with the Dominguez EBL model. The surfaces are built in a specific parameter space between E_{break} and $\Delta\Gamma$.

A.1.11 PKS 0447-439

2009.01.01 - 2010.12.31

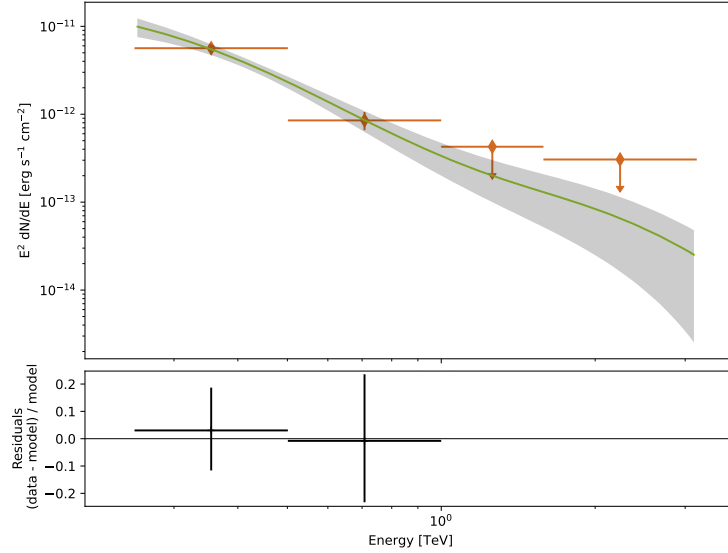


Figure A.29: Best fit spectrum as plotted against a Smooth Broken Power Law with the Dominguez EBL model.

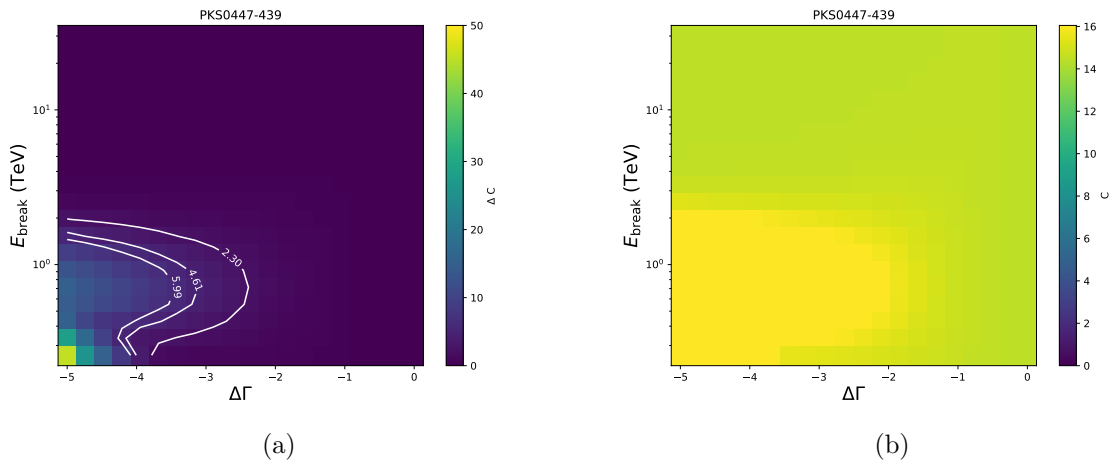


Figure A.30: Statistical surfaces created for the fit of the spectrum against a Smooth Broken Power Law with the Dominguez EBL model. The surfaces are built in a specific parameter space between E_{break} and $\Delta\Gamma$.

A.1.12 PKS 1510-089

2016.01.01 - 2016.12.31

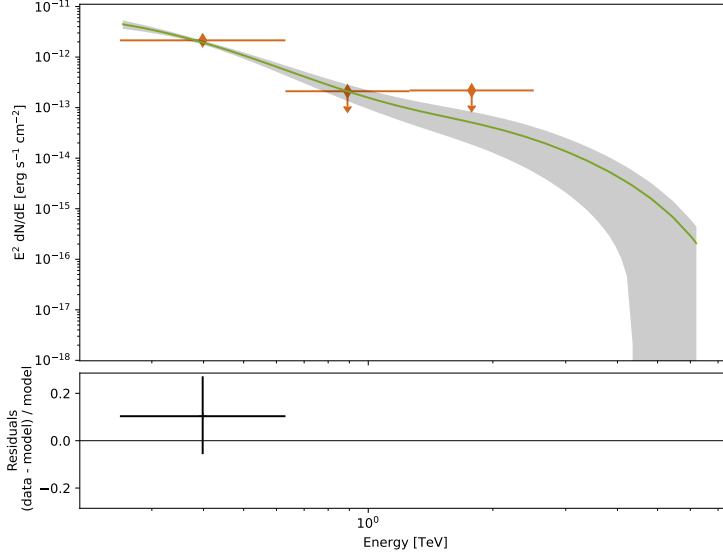


Figure A.31: Best fit spectrum as plotted against a Smooth Broken Power Law with the Dominguez EBL model.

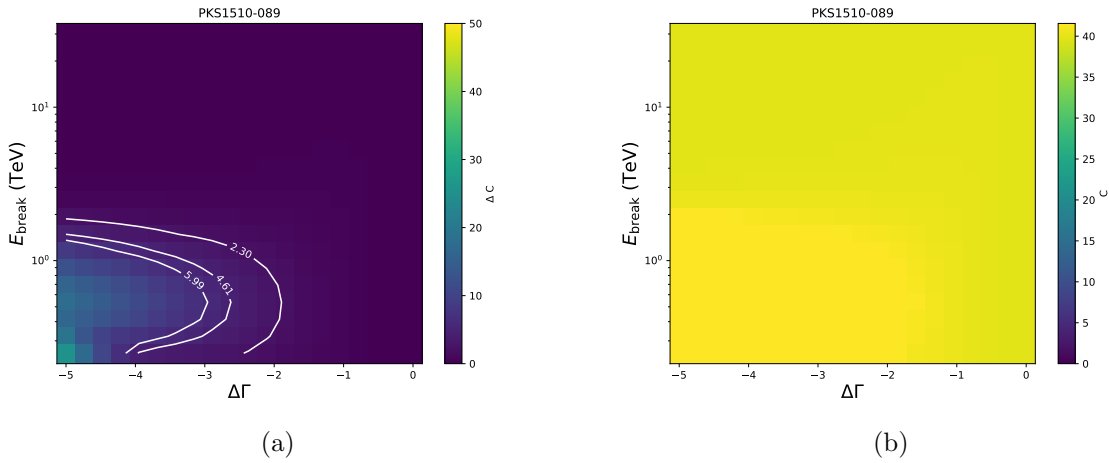


Figure A.32: Statistical surfaces created for the fit of the spectrum against a Smooth Broken Power Law with the Dominguez EBL model. The surfaces are built in a specific parameter space between E_{break} and $\Delta\Gamma$.

A.1.13 PKS 2155-304

2006.07.07 - 2006.07.29

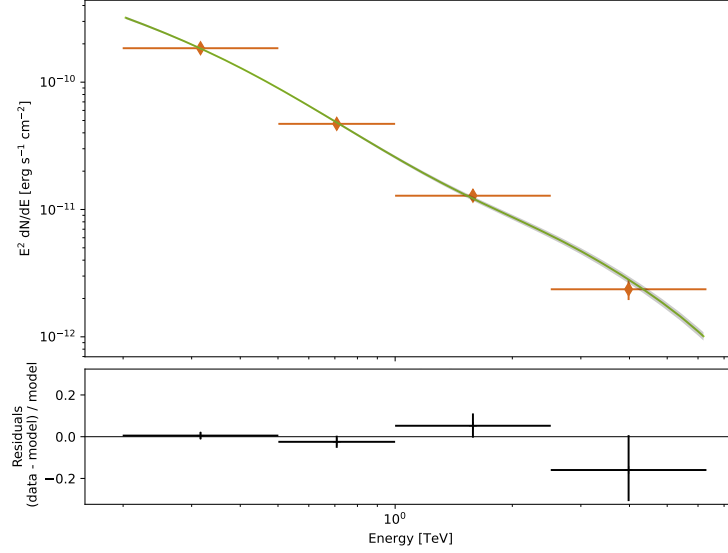


Figure A.33: Best fit spectrum as plotted against a Smooth Broken Power Law with the Dominguez EBL model.

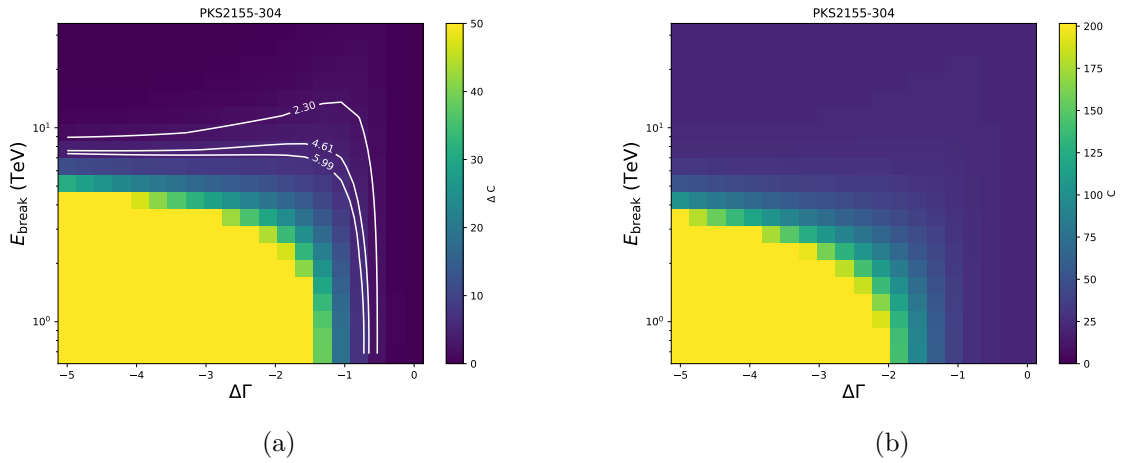


Figure A.34: Statistical surfaces created for the fit of the spectrum against a Smooth Broken Power Law with the Dominguez EBL model. The surfaces are built in a specific parameter space between E_{break} and $\Delta\Gamma$.

2006.07.29 - 2006.07.30

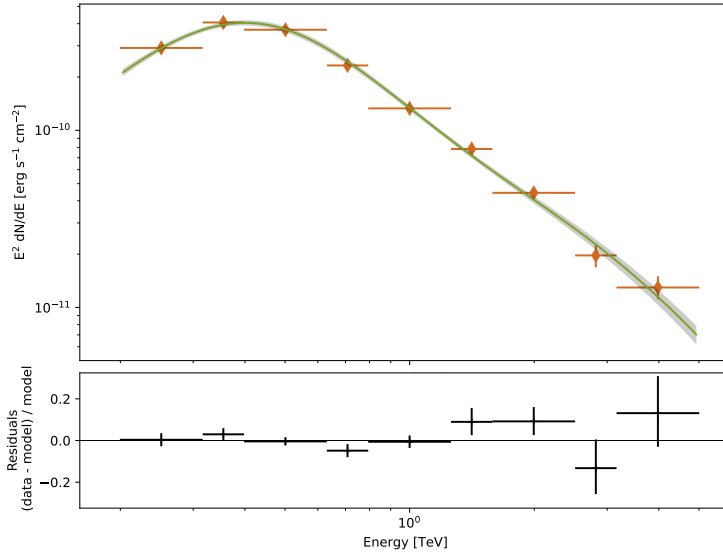


Figure A.35: Best fit spectrum as plotted against a Smooth Double Broken Power Law with the Dominguez EBL model.

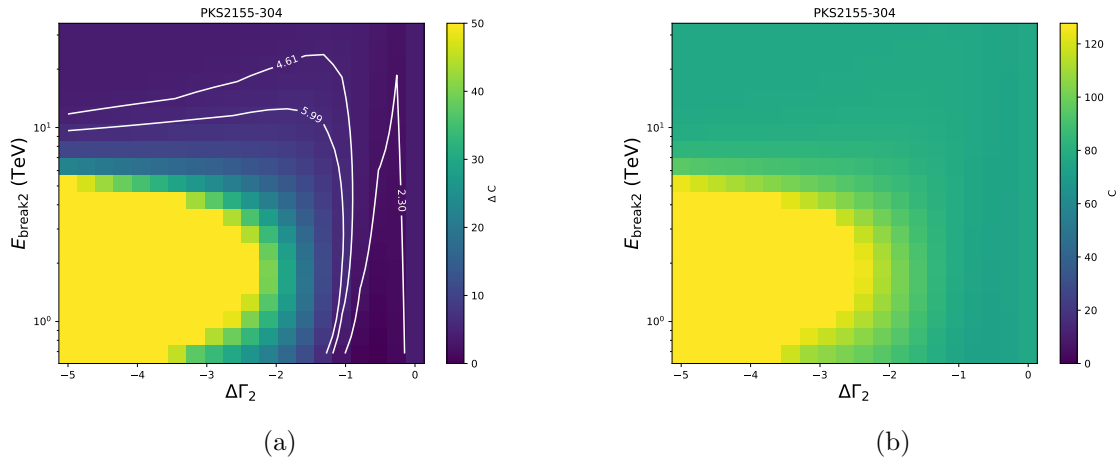


Figure A.36: Statistical surfaces created for the fit of the spectrum against a Smooth Double Broken Power Law with the Dominguez EBL model. The surfaces are built in a specific parameter space between E_{break} and $\Delta\Gamma$.

2006.07.30 - 2006.07.31

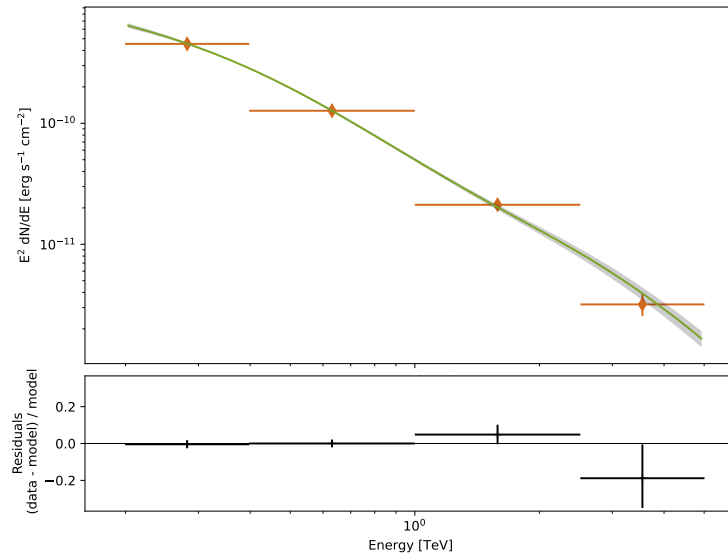


Figure A.37: Best fit spectrum as plotted against a Smooth Double Broken Power Law with the Dominguez EBL model.

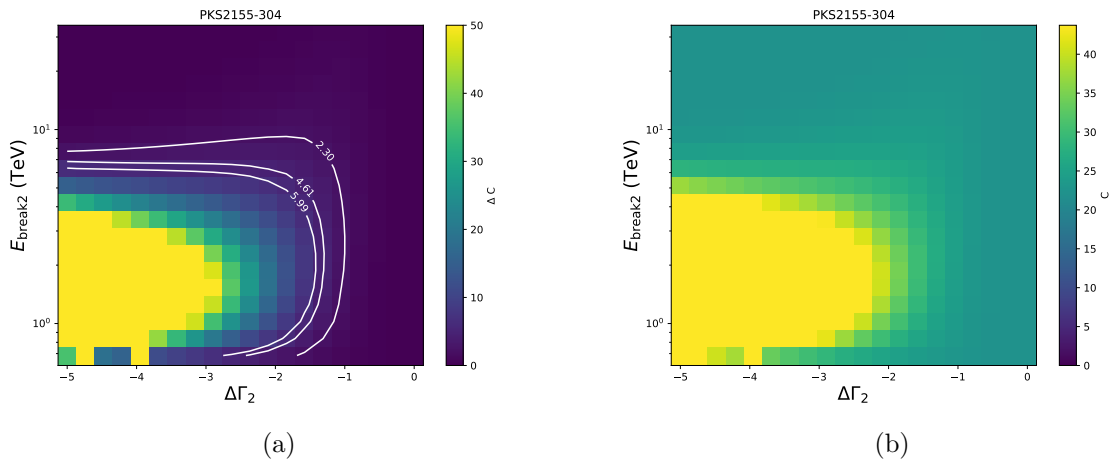


Figure A.38: Statistical surfaces created for the fit of the spectrum against a Smooth Double Broken Power Law with the Dominguez EBL model. The surfaces are built in a specific parameter space between E_{break} and $\Delta\Gamma$.

2006.07.31 - 2006.08.01

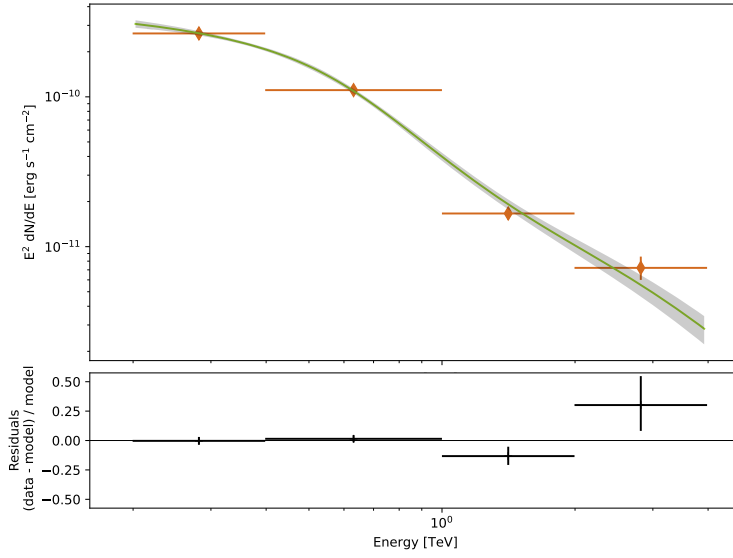


Figure A.39: Best fit spectrum as plotted against a Smooth Double Broken Power Law with the Dominguez EBL model.

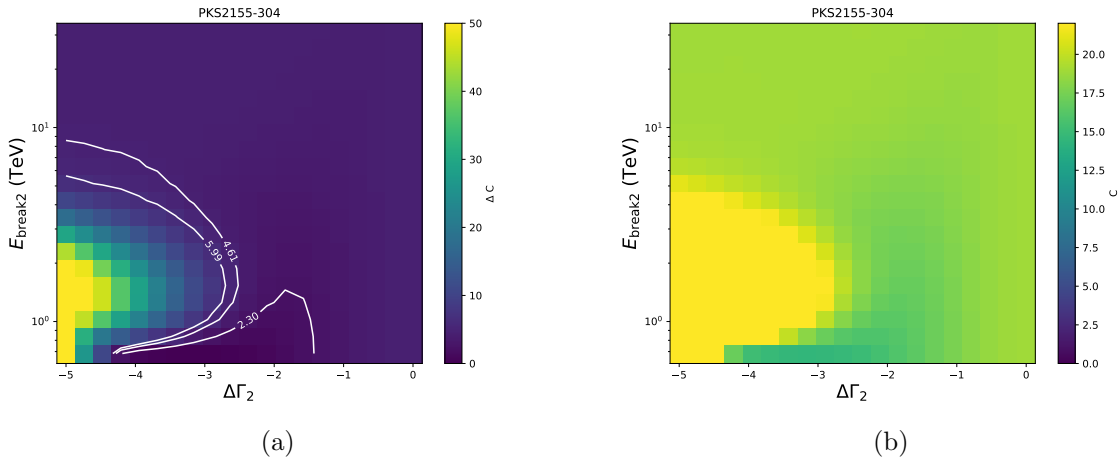


Figure A.40: Statistical surfaces created for the fit of the spectrum against a Smooth Double Broken Power Law with the Dominguez EBL model. The surfaces are built in a specific parameter space between E_{break} and $\Delta\Gamma$.

2006.08.01 - 2006.08.25

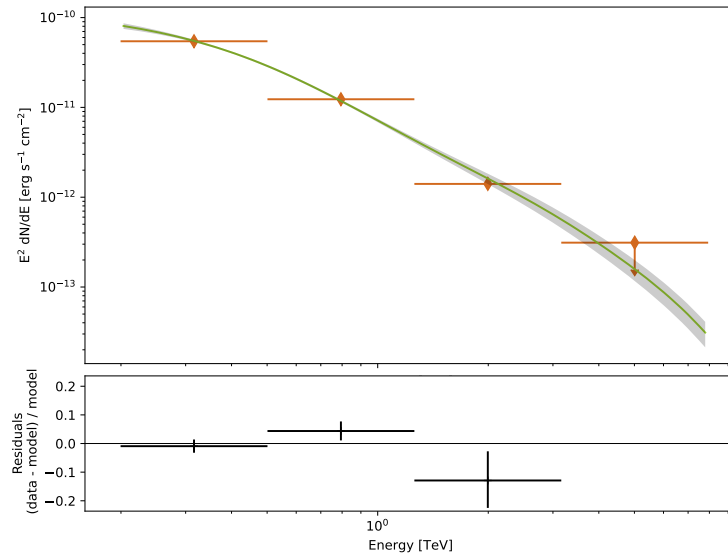


Figure A.41: Best fit spectrum as plotted against a Smooth Double Broken Power Law with the Dominguez EBL model.

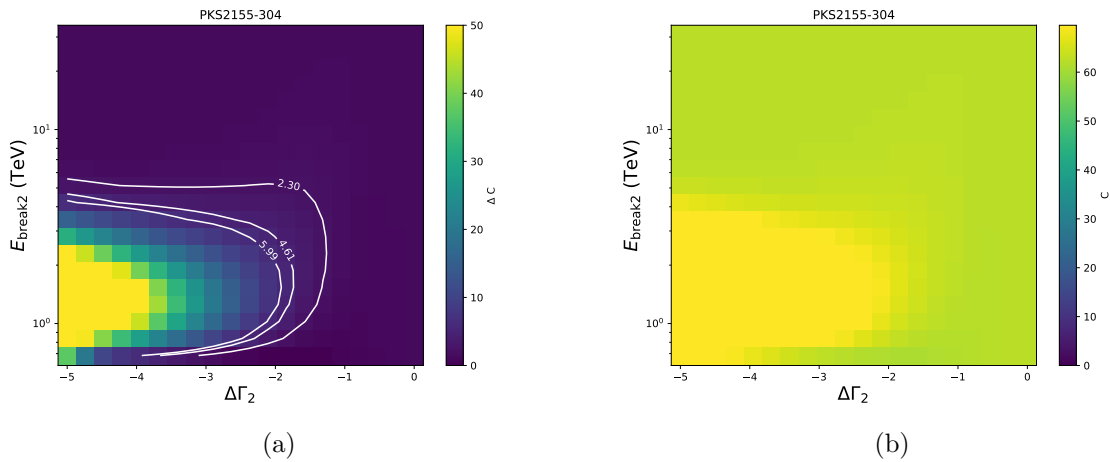


Figure A.42: Statistical surfaces created for the fit of the spectrum against a Smooth Double Broken Power Law with the Dominguez EBL model. The surfaces are built in a specific parameter space between E_{break} and $\Delta\Gamma$.

2006.08.25 - 2006.10.01

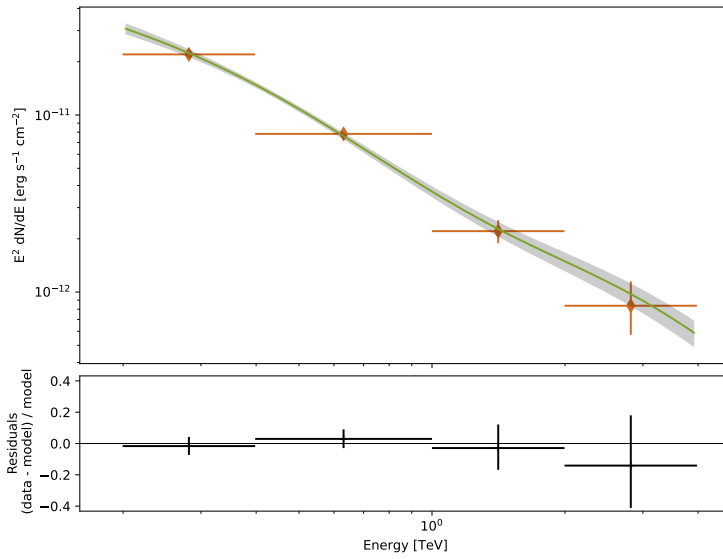


Figure A.43: Best fit spectrum as plotted against a Smooth Broken Power Law with the Dominguez EBL model.

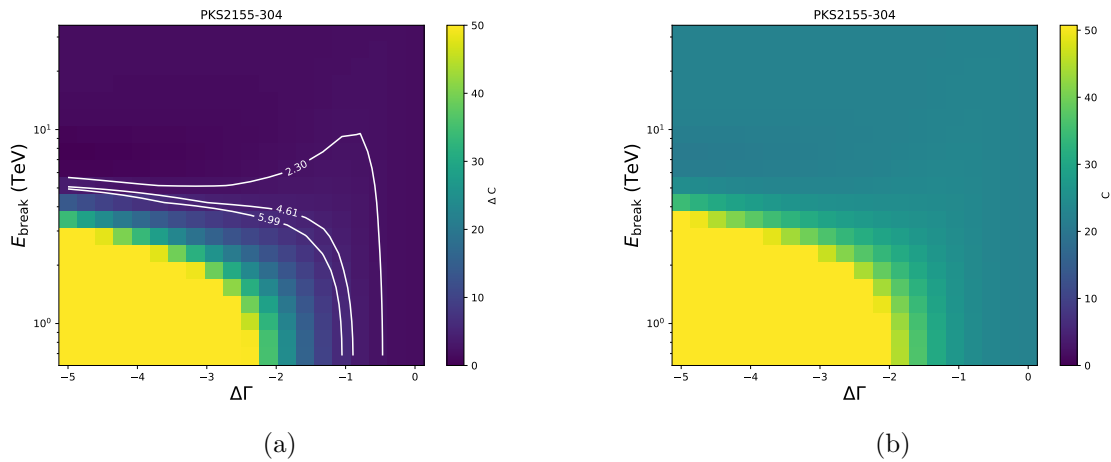


Figure A.44: Statistical surfaces created for the fit of the spectrum against a Smooth Broken Power Law with the Dominguez EBL model. The surfaces are built in a specific parameter space between E_{break} and $\Delta\Gamma$.

References

- Aalseth, C., Semeniouk, I., Creswick, R., Collar, J., Liolios, A., Avignone, F., ... others (1999). *Proposal to the spsc: A solar axion search using a decommissioned lhc test magnet* (Tech. Rep.).
- Abdalla, H., Abramowski, A., Aharonian, F., Benkhali, F. A., Akhperjanian, A., Andersson, T., ... others (2017). Measurement of the ebl spectral energy distribution using the vhe γ -ray spectra of hess blazars. *Astronomy & Astrophysics*, 606, A59.
- Abe, H., Abe, S., Abhir, J., Acciari, V., Agudo, I., Aniello, T., ... others (2024). Constraints on axion-like particles with the perseus galaxy cluster with magic. *Physics of the Dark Universe*, 44, 101425.
- Abel, C., Afach, S., Ayres, N. J., Baker, C. A., Ban, G., Bison, G., ... others (2020). Measurement of the permanent electric dipole moment of the neutron. *Physical Review Letters*, 124(8), 081803.
- Abeln, A., Altenmüller, K., Arguedas Cuendis, S., Armengaud, E., Attié, D., Aune, S., ... others (2021). Conceptual design of babyiaxo, the intermediate stage towards the international axion observatory. *Journal of High Energy Physics*, 2021(5), 1–80.
- Abramowski, A., Acero, F., Aharonian, F., Akhperjanian, A., Anton, G., Balzer, A., ... others (2012). The 2010 very high energy γ -ray flare and 10 years of multi-wavelength observations of m 87. *The Astrophysical Journal*, 746(2), 151.
- Adair, C., Altenmüller, K., Anastassopoulos, V., Arguedas Cuendis, S., Baier, J., Barth, K., ... others (2022). Search for dark matter axions with cast-capp. *Nature Communications*, 13(1), 6180.
- Adams, C., Temples, D., Noroozian, O., Sonnenschein, A., Foster, J., Berlin, A., ... others (2022). *submitter: Axion dark matter* (Tech. Rep.).
- Aharonian, F., Akhperjanian, A., Bazer-Bachi, A., Beilicke, M., Benbow, W., Berge, D., ... others (2006). Fast variability of tera electron volt γ rays from the radio galaxy m87. *Science*, 314(5804), 1424–1427.
- Aharonian, F., Benkhali, F. A., Aschersleben, J., Ashkar, H., Backes, M., Martins, V. B., ... others (2024). Curvature in the very-high energy gamma-ray spectrum of m 87. *Astronomy & Astrophysics*, 685, A96.
- Ajello, M., Helgason, K., Paliya, V., Finke, J., Dominguez, A., Desai, A., ... others (2018). A γ -ray determination of the universe’s star-formation history. *arXiv preprint arXiv:1812.01031*.
- Algaba, J.-C., Asada, K., & Nakamura, M. (2016). Resolving the rotation measure of the m87 jet on kiloparsec scales. *The Astrophysical Journal*, 823(2), 86.
- Alonso, R., Blas, D., & Wolf, P. (2019). Exploring the ultra-light to sub-mev dark matter window with atomic clocks and co-magnetometers. *Journal of High Energy Physics*, 2019(7), 1–46.

- Ansoldi, S., Antonelli, L., Arcaro, C., Baack, D., Babić, A., Banerjee, B., ... others (2018). Gamma-ray flaring activity of ngc1275 in 2016–2017 measured by magic. *Astronomy & astrophysics*, 617, A91.
- Armengaud, E., Attié, D., Basso, S., Brun, P., Bykovskiy, N., Carmona, J., ... others (2019). Physics potential of the international axion observatory (iaxo). *Journal of cosmology and astroparticle physics*, 2019(06), 047.
- Asztalos, S. J., Carosi, G., Hagmann, C., Kinion, D., Van Bibber, K., Hotz, M., ... others (2010). Squid-based microwave cavity search for dark-matter axions. *Physical review letters*, 104(4), 041301.
- Bähre, R., Döbrich, B., Dreyling-Eschweiler, J., Ghazaryan, S., Hodajerdi, R., Horns, D., ... others (2013). Any light particle search ii—technical design report. *Journal of Instrumentation*, 8(09), T09001.
- Balázs, C., Bloor, S., Gonzalo, T. E., Handley, W., Hoof, S., Kahlhoefer, F., ... others (2022). Cosmological constraints on decaying axion-like particles: a global analysis. *Journal of Cosmology and Astroparticle Physics*, 2022(12), 027.
- Batllori, J. M., Gu, Y., Horns, D., Maroudas, M., & Ulrichs, J. (2023). Wisp searches on a fiber interferometer under a strong magnetic field. *arXiv preprint arXiv:2305.12969*.
- Benkhali, F. A., Chakraborty, N., & Rieger, F. M. (2019). Complex gamma-ray behavior of the radio galaxy m 87. *Astronomy & Astrophysics*, 623, A2.
- Berge, D., Funk, S., & Hinton, J. (2007). Background modelling in very-high-energy γ -ray astronomy. *Astronomy & Astrophysics*, 466(3), 1219–1229.
- Biasuzzi, B., Hervet, O., Williams, D., & Biteau, J. (2019). Normalization of the extragalactic background light from high-energy γ -ray observations. *Astronomy & Astrophysics*, 627, A110.
- Bignami, G. F., Boella, G., Burger, J., Keirle, P., Mayer-Hasselwander, H., Paul, J., ... others (1974). The cos-b experiment for gamma-ray astronomy. *The Context and Status of Gamma-Ray Astronomy*, 307–322.
- Bigongiari, C. (2005). The magic telescope. *arXiv preprint astro-ph/0512184*.
- Biteau, J., & Williams, D. A. (2015). The extragalactic background light, the hubble constant, and anomalies: conclusions from 20 years of tev gamma-ray observations. *The Astrophysical Journal*, 812(1), 60.
- Blokhintsev, D. I., & Gal'perin, F. M. (1934). Neutrino hypothesis and the law of conservation of energy. *Pod Znamenem Marksizma*, 6, 147–157.
- Bothun, G. (1998). *Modern cosmological observations and problems*. CRC press.
- Brandt, J. C. (1969). Oso-iii: Preliminary scientific results. *Solar Physics*, 6, 171–174.
- Brubaker, B. (2018). First results from the haystac axion search (ph. d. thesis). Retrieved from.
- Caldwell, A., Dvali, G., Majorovits, B., Millar, A., Raffelt, G., Redondo, J., ... Group), M. W. (2017). Dielectric haloscopes: A new way to detect axion dark matter. *Physical review letters*, 118(9), 091801.
- Cao, Z. (2023). Lhaaso status and physics results. In *Epj web of conferences* (Vol. 280, p. 01003).
- Caputo, A., & Raffelt, G. (2024). Astrophysical axion bounds: The 2024 edition. *arXiv preprint arXiv:2401.13728*.
- Carenza, P., Sharma, R., Marsh, M. D., Brandenburg, A., & Ravensburg, E. (2023). Magnetohydrodynamics predicts heavy-tailed distributions of axion-photon conversion. *Physical Review D*, 108(10), 103029.

- Cecil, R., Barbosa, V. M., Lypova, I., & Meyer, M. (2023). Probing gamma-ray propagation at very-high energies with hess observations of m87.
- Cecil, R., & Meyer, M. (2023). Modeling the magnetic field of the virgo cluster for axion like particle search in gamma ray energies. In *Proceedings of 7th heidelberg international symposium on high-energy gamma-ray astronomy* (p. 182). doi: 10.22323/1.417.0182
- Chadha-Day, F., Ellis, J., & Marsh, D. J. (2022). Axion dark matter: What is it and why now? *Science advances*, 8(8), eabj3618.
- Christenson, J. H., Cronin, J. W., Fitch, V. L., & Turlay, R. (1964). Evidence for the 2π decay of the K^0 meson. *Physical Review Letters*, 13(4), 138.
- Collaboration, H., Aharonian, F., Benkhali, F. A., Arcaro, C., Aschersleben, J., Backes, M., ... others (2023). Constraining the cosmic-ray pressure in the inner virgo cluster using hess observations of m 87. *arXiv preprint arXiv:2305.09607*.
- Collaboration, L., Cao, Z., Aharonian, F., An, Q., Bai, L., Bai, Y., ... others (2023). A tera-electron volt afterglow from a narrow jet in an extremely bright gamma-ray burst. *Science (New York, NY)*, 380(6652), 1390–1396.
- Cowan Jr, C. L., Reines, F., Harrison, F., Kruse, H., & McGuire, A. (1956). Detection of the free neutrino: a confirmation. *Science*, 124(3212), 103–104.
- Curtis, H. D. (1918). Descriptions of 762 nebulae and clusters photographed with the crossley reflector. *Publications of Lick Observatory, vol. 13, pp. 9-42, 13, 9-42*.
- Desai, A., Helgason, K., Ajello, M., Paliya, V., Domínguez, A., Finke, J., & Hartmann, D. (2019). A gev–tev measurement of the extragalactic background light. *The Astrophysical Journal Letters*, 874(1), L7.
- Dine, M. (2001). The strong cp problem. In *Flavor physics for the millennium: Tasi 2000* (pp. 349–369). World Scientific.
- Dine, M., Fischler, W., & Srednicki, M. (1981). A simple solution to the strong cp problem with a harmless axion. *Physics letters B*, 104(3), 199–202.
- Dirac, P. A. M. (1927). The quantum theory of the emission and absorption of radiation. *Proceedings of the Royal Society of London. Series A, Containing Papers of a Mathematical and Physical Character*, 114(767), 243–265.
- Dirac, P. A. M. (1928, February). The quantum theory of the electron. *Proceedings of the Royal Society of London. Series A, Containing Papers of a Mathematical and Physical Character*, 117(778), 610–624. doi: 10.1098/rspa.1928.0023
- Dixit, A. V., Chakram, S., He, K., Agrawal, A., Naik, R. K., Schuster, D. I., & Chou, A. (2021). Searching for dark matter with a superconducting qubit. *Physical review letters*, 126(14), 141302.
- Dominguez, A., Primack, J. R., Rosario, D., Prada, F., Gilmore, R., Faber, S., ... others (2011). Extragalactic background light inferred from aegis galaxy-sed-type fractions. *Monthly Notices of the Royal Astronomical Society*, 410(4), 2556–2578.
- Donath, A., Terrier, R., Remy, Q., Sinha, A., Nigro, C., Pintore, F., ... Zanin, R. (2023). Gammapy: A python package for gamma-ray astronomy. *A&A*, 678, A157. Retrieved from <https://doi.org/10.1051/0004-6361/202346488> doi: 10.1051/0004-6361/202346488
- Dwek, E., & Krennrich, F. (2013). The extragalactic background light and the gamma-ray opacity of the universe. *Astroparticle Physics*, 43, 112–133.
- Einstein, A. (1905, 9 27). Ist die trägheit eines körpers von seinem energieinhalt abhängig? *Annalen der Physik*, 18, 639–641. (English title: "Does the Inertia of a Body Depend Upon Its Energy Content?")

- Ellis, J., Gaillard, M. K., & Nanopoulos, D. V. (2016). A historical profile of the higgs boson. *The standard theory of particle physics*, 255–274.
- Essey, W., & Kusenko, A. (2010). A new interpretation of the gamma-ray observations of distant active galactic nuclei. *Astroparticle Physics*, 33(2), 81–85.
- Essey, W., & Kusenko, A. (2014). Understanding the spectrum of a distant blazar pks 1424+ 240 and its implications. *Astroparticle Physics*, 57, 30–32.
- Fath, E. A. (1909). The spectra of some spiral nebulae and globular star clusters. *Publications of the Astronomical Society of the Pacific*, 21(126), 138–143.
- Feenberg, E., & Primakoff, H. (1948). Interaction of cosmic-ray primaries with sunlight and starlight. *Physical Review*, 73(5), 449.
- Fermi, E. (1934a). Tentativo di una teoria dei raggi β . *Il Nuovo Cimento (1924-1942)*, 11(1), 1–19.
- Fermi, E. (1934b). Versuch einer theorie der β -strahlen. i. *Zeitschrift für Physik*, 88(3), 161–177.
- Feynman, R. P. (2006). *Qed: The strange theory of light and matter* (Vol. 90). Princeton University Press.
- Feynman, R. P. (2018). Space-time approach to quantum electrodynamics. In *Quantum electrodynamics* (pp. 178–198). CRC Press.
- Fichtel, C., Kniffen, D., & Hartman, R. (1973). *Celestial diffuse gamma radiation above 30 mev observed by sas-2* (Tech. Rep.).
- Finke, J. D., Ajello, M., Domínguez, A., Desai, A., Hartmann, D. H., Paliya, V. S., & Saldana-Lopez, A. (2022). Modeling the extragalactic background light and the cosmic star formation history. *The Astrophysical Journal*, 941(1), 33.
- Finke, J. D., Razzaque, S., & Dermer, C. D. (2010). Modeling the extragalactic background light from stars and dust. *The Astrophysical Journal*, 712(1), 238.
- Franceschini, A., Rodighiero, G., & Vaccari, M. (2008). Extragalactic optical-infrared background radiation, its time evolution and the cosmic photon-photon opacity. *Astronomy & Astrophysics*, 487(3), 837–852.
- Gebhardt, K., Adams, J., Richstone, D., Lauer, T. R., Faber, S., Gültekin, K., ... Tremaine, S. (2011). The black hole mass in m87 from gemini/nifs adaptive optics observations. *The Astrophysical Journal*, 729(2), 119.
- Gehrels, N., Chipman, E., & Kniffen, D. (1994). The compton gamma ray observatory. *The Astrophysical Journal Supplement Series*, vol. 92, no. 2, p. 351-362, 92, 351–362.
- Gell-Mann, M. (2018). Symmetries of baryons and mesons. In *The eightfold way* (pp. 216–233). CRC Press.
- Giannotti, M., Irastorza, I. G., Redondo, J., Ringwald, A., & Saikawa, K. (2017). Stellar recipes for axion hunters. *Journal of Cosmology and Astroparticle Physics*, 2017(10), 010.
- Gordon, W. (1926). Der comptoneffekt nach der schrödingerschen theorie. *Zeitschrift für Physik*, 40, 117–133. doi: 10.1007/BF01390840
- Gréaux, L., Biteau, J., & Rosillo, M. N. (2024). The cosmological optical convergence: Extragalactic background light from tev gamma rays. *The Astrophysical Journal Letters*, 975(1), L18.
- Guerrera, A. W. M., & Rigolin, S. (2023). Alp production in weak mesonic decays. *Fortschritte der Physik*, 71(2-3), 2200192.
- Guidetti, D. (2011). Magnetic fields around radio galaxies from faraday rotation measure analysis.

- Higgs, P. W. (1964). Broken symmetries and the masses of gauge bosons. *Physical review letters*, 13(16), 508.
- Hofmann, W., & Zanin, R. (2024). The cherenkov telescope array. In *Handbook of x-ray and gamma-ray astrophysics* (pp. 2787–2833). Springer.
- Holder, J., Atkins, R., Badran, H., Blaylock, G., Bradbury, S., Buckley, J., ... others (2006). The first veritas telescope. *Astroparticle Physics*, 25(6), 391–401.
- Jansson, R., & Farrar, G. R. (2012). A new model of the galactic magnetic field. *The Astrophysical Journal*, 757(1), 14.
- Kashibadze, O. G., Karachentsev, I. D., & Karachentseva, V. E. (2020). Structure and kinematics of the virgo cluster of galaxies. *Astronomy & Astrophysics*, 635, A135.
- Kildea, J., Atkins, R., Badran, H., Blaylock, G., Bond, I., Bradbury, S., ... others (2007). The whipple observatory 10 m gamma-ray telescope, 1997–2006. *Astroparticle Physics*, 28(2), 182–195.
- Kim, J. E. (1979). Weak-interaction singlet and strong cp invariance. *Physical Review Letters*, 43(2), 103.
- Klein, O. (1926). Quantentheorie und fünfdimensionale relativitätstheorie. *Zeitschrift für Physik*, 37, 895–906. doi: 10.1007/BF01397481
- Kneiske, T. M., & Dole, H. (2010). A lower-limit flux for the extragalactic background light. *Astronomy & Astrophysics*, 515, A19.
- Korochkin, A., Neronov, A., & Semikoz, D. (2020). Search for decaying ev-mass axion-like particles using gamma-ray signal from blazars. *Journal of Cosmology and Astroparticle Physics*, 2020(03), 064.
- Lea, S. M., Mushotzky, R., & Holt, S. S. (1982). *Einstein observatory solid state spectrometer observations of m87 and the virgo cluster* (Tech. Rep.).
- Lee, T.-D., & Yang, C.-N. (1956). Question of parity conservation in weak interactions. *Physical Review*, 104(1), 254.
- Lefa, E., Aharonian, F. A., & Rieger, F. M. (2011). “leading blob” model in a stochastic acceleration scenario: The case of the 2009 flare of mkn 501. *The Astrophysical Journal Letters*, 743(1), L19.
- Lefa, E., Rieger, F. M., & Aharonian, F. (2011). Formation of very hard gamma-ray spectra of blazars in leptonic models. *The Astrophysical Journal*, 740(2), 64.
- Marsh, D. J. (2017). Axions and alps: a very short introduction. *arXiv preprint arXiv:1712.03018*.
- Marsh, M. D., Russell, H. R., Fabian, A. C., McNamara, B. R., Nulsen, P., & Reynolds, C. S. (2017). A new bound on axion-like particles. *Journal of Cosmology and Astroparticle Physics*, 2017(12), 036.
- Mei, S., Blakeslee, J. P., Côté, P., Tonry, J. L., West, M. J., Ferrarese, L., ... Merritt, D. (2007). The acs virgo cluster survey. xiii. sbf distance catalog and the three-dimensional structure of the virgo cluster. *The Astrophysical Journal*, 655(1), 144.
- Meyer, M. (2024). *ebtable: Python package to read in tabulated photon densities and gamma-ray opacities*. <https://github.com/me-manu/ebtable>. GitHub.
- Meyer, M., Davies, J., & Kuhlmann, J. (2021). gammaalps: An open-source python package for computing photon-axion-like-particle oscillations in astrophysical environments. *arXiv preprint arXiv:2108.02061*.
- Meyer, M., Montanino, D., & Conrad, J. (2014). On detecting oscillations of gamma rays into axion-like particles in turbulent and coherent magnetic fields. *Journal of Cosmology and Astroparticle Physics*, 2014(09), 003.

- Moretti, R., Corti, H. A., Labranca, D., Ahrens, F., Avallone, G., Babusci, D., ... others (2024). Design and simulation of a transmon qubit chip for axion detection. *IEEE Transactions on Applied Superconductivity*.
- Morrison, P. (1958). Unknown Title. *Nuovo Cimento*. (Considered to mark the birth of gamma ray astronomy)
- Murgia, M., Govoni, F., Feretti, L., Giovannini, G., Dallacasa, D., Fanti, R., ... Dolag, K. (2004). Magnetic fields and faraday rotation in clusters of galaxies. *Astronomy & Astrophysics*, 424(2), 429–446.
- Ne’eman, Y. (1961). Derivation of strong interactions from a gauge invariance. *Nuclear physics*, 26(2), 222–229.
- Newton, I. (1687). *Philosophiæ naturalis principia mathematica*. Londini: Jussu Societatis Regiæ ac Typis Josephi Streater. Prostat apud plures Bibliopolas. (First edition. Printed for the Royal Society by Joseph Streater, and sold by multiple booksellers.)
- Nigro, C., Deil, C., Zanin, R., Hassan, T., King, J., Ruiz, J. E., ... others (2019). Towards open and reproducible multi-instrument analysis in gamma-ray astronomy. *Astronomy & Astrophysics*, 625, A10.
- Noether, E. (1918). Invariante variationsprobleme, nachrichten von der gesellschaft der wissenschaften zu göttingen, mathematisch-physikalische klasse 1918 (1918) 235–257. URL <http://eudml.org/doc/59024>.
- Nulsen, P., & Böhringer, H. (1995). A rosat determination of the mass of the central virgo cluster. *Monthly notices of the royal astronomical society*, 274(4), 1093–1106.
- Overduin, J. M., & Wesson, P. S. (2004). Dark matter and background light. *Physics Reports*, 402(5-6), 267–406.
- Owen, F. N., Eilek, J. A., & Keel, W. C. (1990). Detection of large faraday rotation in the inner 2 kiloparsecs of m87. *Astrophysical Journal, Part 1 (ISSN 0004-637X)*, vol. 362, Oct. 20, 1990, p. 449-454., 362, 449–454.
- Peccei, R. D., & Quinn, H. R. (1977a). Constraints imposed by cp conservation in the presence of pseudoparticles. *Physical Review D*, 16(6), 1791.
- Peccei, R. D., & Quinn, H. R. (1977b). Cp conservation in the presence of pseudoparticles. *Physical Review Letters*, 38(25), 1440.
- Pontecorvo, B. (1957). Mesonium and antimesonium. *Zh. Eksp. Teor. Fiz.*, 33, 549. ([Sov. Phys. JETP 6, 429 (1958)])
- Primakoff, H. (1951). Photo-production of neutral mesons in nuclear electric fields and the mean life of the neutral meson. *Physical Review*, 81(5), 899.
- Pshirkov, M., & Popov, S. (2009). Conversion of dark matter axions to photons in magnetospheres of neutron stars. *Journal of Experimental and Theoretical Physics*, 108, 384–388.
- Pühlhofer, G., Leuschner, F., & Salzmann, H. (2024). Hess: The high energy stereoscopic system. In *Handbook of x-ray and gamma-ray astrophysics* (pp. 2745–2785). Springer.
- Raffelt, G., & Stodolsky, L. (1988). Mixing of the photon with low-mass particles. *Physical Review D*, 37(5), 1237.
- Ringwald, A. (2014). Searching for axions and alps from string theory. In *Journal of physics: Conference series* (Vol. 485, p. 012013).
- Russell, H., Fabian, A., McNamara, B., & Broderick, A. (2015). Inside the bondi radius of m87. *Monthly Notices of the Royal Astronomical Society*, 451(1), 588–600.
- Saldana-Lopez, A., Domínguez, A., Pérez-González, P. G., Finke, J., Ajello, M., Primack, J. R., ... Desai, A. (2021). An observational determination of the evolving

- extragalactic background light from the multiwavelength hst/candels survey in the fermi and cta era. *Monthly Notices of the Royal Astronomical Society*, 507(4), 5144–5160.
- Seyfert, C. K. (1943). Nuclear emission in spiral nebulae. In *A source book in astronomy and astrophysics, 1900–1975* (pp. 738–743). Harvard University Press.
- Shifman, M. A., Vainshtein, A., & Zakharov, V. I. (1980). Can confinement ensure natural cp invariance of strong interactions? *Nuclear Physics B*, 166(3), 493–506.
- Sikivie, P. (1983). Experimental tests of the” invisible” axion. *Physical Review Letters*, 51(16), 1415.
- Thompson, D. J., & Wilson-Hodge, C. A. (2022). Fermi gamma-ray space telescope. In *Handbook of x-ray and gamma-ray astrophysics* (pp. 1–31). Springer.
- Tully, R. B., Courtois, H. M., & Sorce, J. G. (2016). Cosmicflows-3. *The Astronomical Journal*, 152(2), 50.
- Urban, O., Werner, N., Simionescu, A., Allen, S., & Böhringer, H. (2011). X-ray spectroscopy of the virgo cluster out to the virial radius. *Monthly Notices of the Royal Astronomical Society*, 414(3), 2101–2111.
- Vacca, V., Murgia, M., Govoni, F., Feretti, L., Giovannini, G., Perley, R., & Taylor, G. (2012). The intracluster magnetic field power spectrum in a2199. *Astronomy & Astrophysics*, 540, A38.
- Vazza, F., Brueggen, M., Gheller, C., Hackstein, S., Wittor, D., & Hinz, P. M. (2017). Simulations of extragalactic magnetic fields and of their observables. *Classical and Quantum Gravity*, 34(23), 234001.
- Vazza, F., Locatelli, N., Rajpurohit, K., Banfi, S., Domínguez-Fernández, P., Wittor, D., ... others (2021). Magnetogenesis and the cosmic web: A joint challenge for radio observations and numerical simulations. *Galaxies*, 9(4), 109.
- Virtanen, P., Gommers, R., Oliphant, T. E., Haberland, M., Reddy, T., Cournapeau, D., ... SciPy 1.0 Contributors (2020). SciPy 1.0: Fundamental Algorithms for Scientific Computing in Python. *Nature Methods*, 17, 261–272. doi: 10.1038/s41592-019-0686-2
- Weinberg, S. (1978). A new light boson? *Physical Review Letters*, 40(4), 223.
- Wilczek, F. (1978). Problem of strong p and t invariance in the presence of instantons. *Physical Review Letters*, 40(5), 279.
- Wu, C.-S., Ambler, E., Hayward, R. W., Hoppes, D. D., & Hudson, R. P. (1957). Experimental test of parity conservation in beta decay. *Physical review*, 105(4), 1413.
- Yukawa, H. (1955). On the interaction of elementary particles. i. *Progress of Theoretical Physics Supplement*, 1, 1–10.
- Zemcov, M., Immel, P., Nguyen, C., Cooray, A., Lisse, C. M., & Poppe, A. R. (2017). Measurement of the cosmic optical background using the long range reconnaissance imager on new horizons. *Nature Communications*, 8(1), 15003.
- Zhang, X., Houston, N., & Li, T. (2023). Nuclear decay anomalies as a signature of axion dark matter. *Physical Review D*, 108(7), L071101.
- Zhitnitskij, A. (1980). On possible suppression of the axion-hadron interactions. *Yadernaya Fizika*, 31(2), 497–504.